VNIVERSITAT DE VALÈNCIA

Facultad de Física

Departamento de Física Aplicada

SOLUTION PROCESSABLE PbS QD-SOLID PHOTODETECTORS FOR TELECOMMUNICATION APPLICATIONS

Ph.D. Thesis

Programa de Doctorado en Física

Author:
Alberto Maulu

Co-supervisors:
Prof. Juan P. Martínez Pastor

Dr. Pedro J. Rodríguez Cantó

Valencia, September 2018

Dedicated to Cécile and Angelo.

Acknowledgments

These years as a PhD student have represented a period of continuous learning in both the scientific and the personal side. Many are indeed the persons that during this time believed in me and gave me their priceless support, and now that this experience comes to its conclusion I would like to express my gratitude to all of them.

I would like to commence by expressing my sincere and profound gratitude to Professor Juan Martínez Pastor and to Dr. Pedro Rodríguez Cantó for their infinite patience, support and guidance. Their dedication and love for science have been for me a source of inspiration throughout all the PhD.

I would like to extend my thanks to all the members of the Applied Physics Department and the members of the Institute of Material Science of the University of Valencia (ICMUV) for their warm welcome and for always being ready to help me in case of need.

I thank to all my people at the UMDO group and Intenanomat S.L., I feel deeply grateful for the possibility I had to do this fantastic experience. I also would like to acknowledge the Generalitat Valenciana for the Santiago Grisolía grant that gave me the opportunity to follow my studies at the University of Valencia.

A special thanks to my estimate friends Mauro Brotons, Juan Navarro, Daniel Andrés and Mattia Signoretto, I feel extremely privileged for having shared the PhD years with all of you.

I am immensely grateful to all my friends who accompanied me outside the academic context, specially Slava Melnikov, Valerio Corinaldesi, Marco Castellaccio, Fabio Muretti, Enrico Schintu and Guido Ielasi, your friendship is a priceless gift.

To my big family, thank you to be always there, to share with me all your enthusiasm and passions. I know that even if I will be far for long, I will never feel alone.

To my father, that always gave me his unconditional support in every activity I made, that offered me his wise guidance and his inestimable friendship, to him goes my endless gratitude, you are the man I hope to become.

Cécile, my fiancé, she is the one that shared with me the most of the emotional difficulties that accompany the making of a PhD thesis. Thank you for all your patience and your endless affection, in it I find the serenity and the strength to face every challenge.

Many thanks to all of you.

Abstract

La detección óptica y la conversión de luz en electricidad (conversión fotovoltaica), en la que los dispositivos optoelectrónicos encuentran su campo de aplicación más importante, han sido importantes campo de aplicación durante décadas de los semiconductores monocristalinos como materiales fotoactivos (absorción de luz y fotogeneración de portadores). Su éxito se debe a los excelentes resultados alcanzados, aunque viene acompañado de inconvenientes, como el elevado coste de producción, la complejidad de fabricación y su incompatibilidad con substratos flexibles. Durante la última década, el advenimiento de los materiales optoelectrónicos procesados en disolución, como los puntos cuánticos (QDs) coloidales, ha abierto nuevas posibilidades para aplicaciones optoelectrónicas. Este nuevo enfoque aplicado al desarrollo de detectores ópticos reside en el alto grado de control que ofrece la ingeniería de materiales a la nanoescala. Además, la procesabilidad de dichos nanomateriales ha permitido su integración en muchos tipos de substratos comerciales de bajo coste, en algunos casos logrando fotodispositivos con figuras de mérito comparables a las de los fotodetectores convencionales. Por ejemplo, en el grupo del Prof. Edward H. Sargent (Universidad de Toronto, Canadá) han medido detectividades de hasta 10^{13} jones en la segunda ventana de telecomunicaciones (1.3 μm) en fotodetectores basados en QDs de Pbs, un orden de magnitud mayor que la detectividad lograda en fotodetectores basados en películas delgadas de InGaAs crecidas epitaxialmente.

En esta tesis hemos pretendido y conseguido desarrollar fotodetectores basados en QDs de PbS estables en aire y procesados en disolución, con una alta sensibilidad en longitudes de onda del infrarrojo próximo (hasta unos 1600 nm), esto es, útiles para la detección óptica en la tercera ventana de telecomunicaciones. Para conseguir este objetivo principal, primero se ha dedicado el esfuerzo necesario para optimizar la síntesis química de los QDs de PbS con el tamaño adecuado para obtener su borde de absorción en las longitudes de onda señaladas, como base para la producción de películas delgadas con un enfoque ascendente (*bottom-up*). En segundo lugar, hemos conseguido “nanotintas” estables en aire con estos QDs de PbS, adecuadamente formuladas para su compatibilidad (propiedades reológicas adecuadas) con un método eficiente de deposición en área extensa, que permita la formación de una película delgada de QDs

de PbS libre de defectos estructurales (ligados al apilamiento vertical de los QDs, que no son más que nanocristales aproximadamente esféricos de unos 6-7 nm de diámetro). La técnica de deposición elegida ha sido "doctor blading", donde una cuchilla extiende la nanotinta sobre un substrato dado, en nuestro caso vidrio/ITO (ITO: Indium Tin Oxide) o Si/SiO_2, para la fabricación de fotodiodos y fotoconductores, respectivamente.

También hemos estudiado la influencia de la química superficial de los QDs de PbS en las propiedades de las películas delgadas producidas con éstos y los dispositivos fabricados con estas capas. De hecho, el paso clave en la formación de películas conductoras con QDs de PbS es el procedimiento de intercambio de ligandos en estado sólido, en el que se reemplazan las moléculas largas (Oleilamina) utilizadas para la síntesis de los QDs de PbS con otras más cortas, con el fin de reducir la distancia entre los QDs, lo que aumentaría la movilidad de los portadores en el sólido de QDs resultante debido a un fuerte acoplamiento electrónico. Específicamente, hemos utilizado el ácido 3-Mercapto-Propiónico (MPA) y el Ioduro de Tetra-butil-amonio (TBAI), lo que ciertamente influye en la superficie de los QDs de PbS y en el rendimiento de los fotodetectores basados en PbS. Encontramos que, en ambos casos, el mecanismo responsable de la fotoconductividad está relacionado con la sensibilización de sólido de QDs por trampas, origen de la alta responsividad observada y la lenta respuesta temporal de los dispositivos fotoconductores. Se ha identificado la importante influencia de los niveles de trampas sobre la dinámica de los portadores y la eficiencia final del dispositivo, además de evidenciar el compromiso entre la velocidad del dispositivo y la alta responsividad de los dispositivos fotoconductores. El intercambio de ligandos en el sólido de QDs con MPA, mientras pasiva eficazmente su superficie, produce un rendimiento superior del dispositivo (mayor foto-sensibilidad y detectividad), lo cual se debe a una menor corriente oscura y menor nivel de ruido en comparación con el caso de los sólidos de QDs tratados con TBAI. Además, el intercambio de ligandos con MPA confiere una excelente estabilidad en aire a los sólidos de QDs, reduciendo la oxidación del PbS, como se deduce de medidas de XPS. Sobre la base de estos hallazgos, finalmente hemos desarrollado un fotodetector estable en aire y altamente sensible (10^{11} Jones), basado en un fotodiodo de arquitectura Schottky con una eficiencia cuántica interna superior al 30% a 1500 nm y con una respuesta temporal de unos 135 μs.

Abstract

Optical sensing and conversion of light into electricity (photovoltaics), on which optoelectronic devices find their more important application field, have been for decades important fields of application for single-crystal semiconductors as photoactive (light absorption and carrier photogeneration) materials. Their success relay on the excellent performances achieved in these devices, which indeed are accompanied by several drawbacks, as high production cost, manufacture complexity and incompatibility with flexible substrates. During the last decade the advent of solution-processed optoelectronic materials, such as colloidal quantum dots (QDs), has opened new prospective for optoelectronic applications. This new approach applied to develop optical detectors lies in the high degree of control offered by nanoscale materials engineering. Moreover, solution-processability of these nanomaterials has enabled their low-cost integration over many commercial substrates, in some cases achieving photodevices with figures of merit comparable to those of conventional photodetectors. For instance, the group of Prof. Edward H. Sargent (Toronto University, Canada) reported detectivities of about 10^{13} jones in the second telecom window (1.3 μm) for PbS QD-based photodetectors. This is one order of magnitude higher than the detectivity achieved for photodetectors based on epitaxially grown InGaAs thin films.

In this thesis we have tried and succeeded in developing photodetectors based on PbS QDs stable in air and processed in solution, with a high sensitivity in near-infrared wavelengths (up to about 1600 nm), that is, useful for optical detection in the third telecommunications window. To achieve this main objective, we have undertaken the necessary efforts to optimize the chemical synthesis of the PbS QDs with the appropriate size to obtain their absorption edge at the indicated wavelengths, these QDs were the basis to produce thin films within a bottom-up approach. Secondly, we have achieved "nanoinks" with these PbS QDs that are stable in air and suitably formulated for their compatibility (adequate rheological properties) with an efficient method of deposition for large areas that allows the formation of a thin film of PbS QDs free of structural defects (associated to the 3D stacking of the QDs, which are approximately spherical nanocrystals of about 6-7 nm in diameter). The chosen large-area deposition technique has been "doctor

blading", where a blade extends the ink on a given substrate, in our case glass/ITO (ITO: Indium Tin Oxide) or Si/SiO_2, for the fabrication of photodiodes and photoconductors, respectively.

We have also studied the influence of the QD surface chemistry on the properties of their produced thin films and fabricated photodevices. In fact, the key step in the formation of conductive PbS QD films is the solid-state ligand exchange procedure by replacing long isolating molecules (Oleylamine) used for the QD synthesis with shorter ones, in order to reduce the interparticle distance, which would increase the carrier mobility in the resulting strongly-coupled QD-solid. Specifically, we have used 3-mercaptopropionic acid (MPA) and tetrabutylammonium iodide (TBAI), which certainly influences the surface of the PbS QDs and the performances of PbS-based photodetectors. We did find that, in both cases, the mechanism responsible of photoconductivity is related to trap sensitization of the QD-solid, which is responsible of the observed high responsivity and low time response of photoconductor devices. The important influence of trap states over the carrier dynamics and the final device performances have been identified, and evidenced the trade-off between device speed and photon detection responsivity of the device. The ligand exchange of the QD-solid film with MPA, while efficiently passivating the PbS QDs, yields a superior device performance (photo-sensitivity and detectivity), which is due to a smaller dark current and lower noise level as compared to the case of PbS QD-solids treated with TBAI. Furthermore, MPA ligand exchange confers excellent long-term air-stability to the QD-solids reducing the oxidation of PbS QDs, as deduced from XPS measurements. Based on these findings, we have finally developed an air-stable highly sensitive (10^{12} Jones) photodetector based on a simple Schottky photodiode architecture with internal quantum efficiency higher than 30% at 1500 nm and time response of about 135 μs.

Table of Content

List of Figures

List of Tables

Chapter 1 Introducción: objetivos y metodologías

La detección óptica y el almacenamiento y reproducción de imágenes son la base de la transducción de nuestro mundo visual en señales digitales que pueden almacenarse, transportarse y procesarse. La detección de la luz ha sido tradicionalmente facilitada por fotodetectores monocristalinos de área pequeña, que se caracterizan por su alto coste, complejidad y rigidez.

En el presente trabajo, demostramos un nuevo enfoque para la fotodetección basado en puntos cuánticos coloidales (CQDs) procesados en disolución. Esta forma de procesado de nanomateriales permite la producción de fotodetectores flexibles de gran área y bajo coste.

En este capítulo, se presentan varios dispositivos optoelectrónicos relativos a la fotodetección. A continuación, se describen las propiedades fundamentales de un fotodetector de uso en telecomunicaciones. Se revisará brevemente el estado del arte de los fotodetectores basados en puntos cuánticos coloidales, y se discuten sus ventajas y desventajas, que es la motivación principal del presente trabajo de tesis. Finalmente, este capítulo concluye con los objetivos y la organización de esta tesis.

1.1 Optoelectrónica para telecomunicaciones

El concepto de dispositivos optoelectrónicos se introdujo por primera vez durante la segunda mitad de la década de los ‘80, pero solo con el nuevo milenio se ha convertido en uno de los campos de investigación más prósperos del mundo, impulsado principalmente por el rápido desarrollo de la tecnología de comunicación digital. De hecho, con el tráfico de Internet en continuo aumento y las necesidades de miniaturización de componentes electrónicos digitales, la tecnología basada en cobre ya no podría satisfacer los nuevos requisitos de las aplicaciones de telecomunicaciones. Bajo esta circunstancia, la optoelectrónica será un protagonista en las aplicaciones de comunicaciones modernas debido a la transmisión de alta velocidad y la alta eficiencia que promete.

Hoy en día, las transmisiones de datos a larga distancia se llevan a cabo principalmente en la ventana espectral entre 1300 y 1550 nm, que corresponde a la pérdida óptica mínima para las fibras ópticas de sílice. Por lo tanto, puesto que los dispositivos optoelectrónicos que operan en este rango de longitud de onda se pueden conectar a servidores externos sin necesidad de convertidores de longitud de onda, hemos de encontrar nuevas soluciones para fuentes de luz,[1],[2] moduladores ópticos[3] y componentes pasivos[4],[5].

Entre los dispositivos optoelectrónicos, el fotodetector se encuentra al final de la trayectoria óptica (receptor) con la función de convertir la luz en señal eléctrica. La calidad de la conversión de señal afecta críticamente al rendimiento global de todo el sistema.

Tradicionalmente, la fotodetección ha sido posible mediante dispositivos basados en semiconductores monocristalinos, que han demostrado ampliamente sus prestaciones, con una alta movilidad de portadores, absorción de luz eficiente, así estabilidad térmica y óptica. Sin embargo, la tecnología basada en semiconductores monocristalinos también tiene importantes desventajas, como los altos costes de producción, el procesamiento a alta temperatura, el limitado rango espectral de funcionamiento y las estrictas condiciones relativas al desajuste reticular para la integración en los circuitos CMOS. Además, los semiconductores monocristalinos están excluidos de la aplicación en dispositivos electrónicos flexibles debido a la incompatibilidad de los parámetros de procesado y crecimiento. Además, la aplicación de

obleas de silicio en superficies extensas se ve impedida debido a la incompatibilidad del proceso Czochralski y de procesos de deposición en continuo (“roll-to-roll”) para sustratos flexibles.

Puntos cuánticos sintetizados en disolución

En la búsqueda de soluciones a estas limitaciones, la optoelectrónica basada en puntos cuánticos (QDs) coloidale, gracias a sus propiedades ópticas y electrónicas dependientes del tamaño, representa una de las soluciones más interesantes hacia aplicaciones tecnológicas sin precedentes.

Las potencialidades de la optoelectrónica basada en QDs coloidales comienzan con la propia síntesis de éstos, que se realiza de forma simple por vías de química húmeda, como el método de inyección en caliente, donde los precursores se dispersan en diferentes matraces y luego se inyectan uno en el otro a una temperatura precisa. Mediante la elección cuidadosa de las concentraciones de los precursores, sus temperaturas, tiempo de reacción, así como la selección del disolvente y los ligandos orgánicos, es posible producir QDs con el tamaño y la forma deseada. La Figure 3 muestra la absorción de QDs de PbS donde, variando el diámetro del nanocristal de 10 a 3 nm, el pico de absorción puede ajustarse de 1800 a 800 nm, respectivamente.[6]

Debido a que sus propiedades dependen enormemente del tamaño de la nanopartículas, el PbS se ha estudiado para una amplia gama de aplicaciones de detección óptica como imágenes SWIR para visión nocturna,[7] conversión de energía fotovoltaica [8] e integrado en dispositivos de telecomunicación como guías de onda [9] y fotodetectores.[10] En el trabajo aquí presentado, hemos propuesto los QDs de PbS como material activo para aplicaciones de fotodetección, explotando la posibilidad de abordar longitudes de onda de telecomunicaciones (infarrojo cercano, 1300-1600 nm).

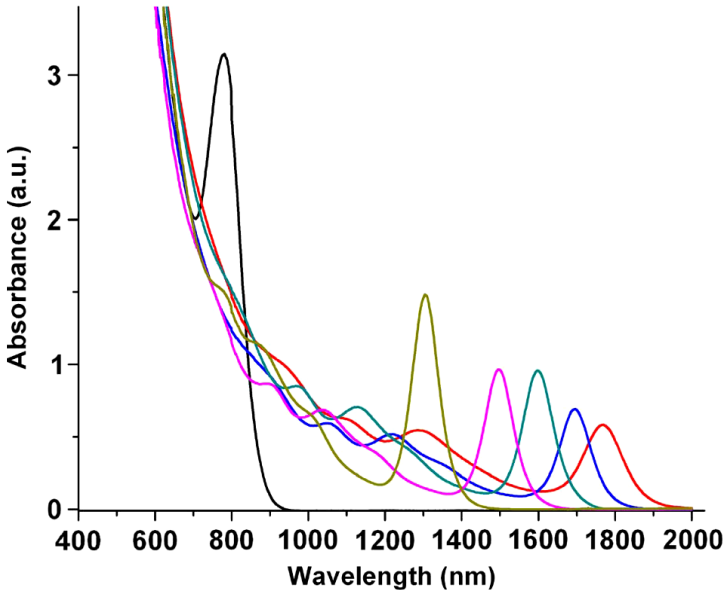

Figura 1: Espectros de absorción de QDs de PbS con tamaños que varían de 10 nm (rojo) a 3 nm (negro) de diámetro.[6]

Después de la síntesis y del procedimiento post-sintético que consiste en la purificación, el aislamiento y la re-dispersión de los QDs en disolventes orgánicos seleccionados, es posible producir una dispersión coloidal estable de nanocristales de PbS. Después de la optimización de sus propiedades reológicas, la solución está lista para ser procesada para producir películas delgadas de QDs y, desde aquí, dispositivos optoelectrónicos.

Como consecuencia, se han explorado métodos de procesado en disolución para deposición de películas delgadas como drop casting,[11] recubrimiento por centrifugación[12] y recubrimiento por inmersión,[13] entre otras técnicas, para fabricar dispositivos optoelectrónicos basados en puntos cuánticos. Estas técnicas de bajo coste muestran diferentes ventajas y desventajas, aunque permiten la fabricación de películas delgadas de QDs sobre sustratos rígidos[10] y flexibles[14] sin problemas de desajuste reticular, siempre y cuando los nanocristales tenga misma forma y tamaño (baja dispersión de éste).

En la Figure 4 se muestra un ejemplo de la procesabilidad de la disolución de QDs sobre un sustrato flexible.[14] En este caso particular, se trata de un dispositivo fotoconductor para la detección de gas NO_2, donde los QDs de PbS se ha depositado por centrifugación (“spin coating”) sobre un sustrato de papel con

un patrón de electrodos de Au interdigitados previamente estampado. Esta es una prueba de concepto que muestra la potencialidad de los QDs aplicados a dispositivos de fotodetección portátiles.

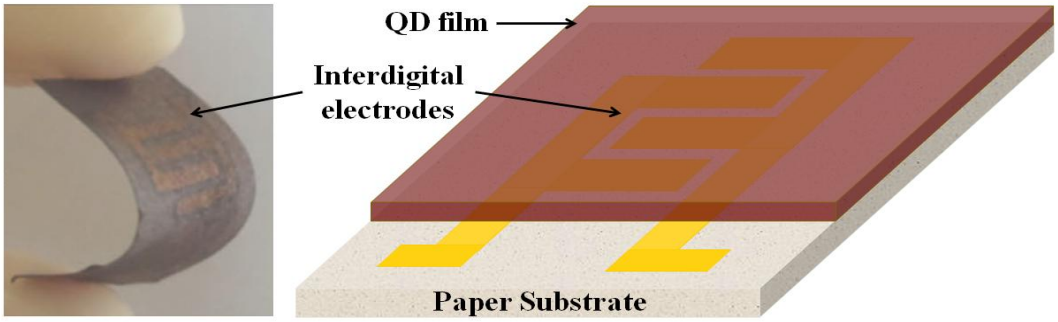

Figure 2: Ejemplo de dispositivo flexible para detección de gas NO_2 basado en CQDs.

Recientemente se ha dado un interés creciente en la capacidad de producir un autoensamblado en el proceso de formación de capas de QDs o, lo que es lo mismo, la producción de estructuras sólidas ordenadas (que hemos denominado "QD-solid"), también llamadas "supercristales".[15] En estas estructuras ordenadas de QDs podremos obtener un transporte de carga mejorado[16], así como un cierto cambio en su propiedades ópticas,[17], lo que podría considerarse como un nuevo tipo de semiconductor, cuyo comportamiento depende tanto de la naturaleza individual de las nanopartículas como de las interacciones entre ellas (acoplamiento electrónico).[18] En este punto, el confinamiento de los portadores dentro de los puntos cuánticos, además de dar las propiedades únicas asociadas a los QDs, representa un desafío para la extracción y el transporte eficientes de los portadores de carga requeridos en aplicaciones de telecomunicaciones de alta velocidad. En este contexto, el estudio fundamental del transporte de carga, desde estados cuánticos confinados o localizados a estados deslocalizados e hibridados presentes en los supercristales, es de importancia primordial. La identificación y caracterización de los factores críticos que subyacen a la movilidad de los portadores de carga en estos supercristales es hoy en día de gran importancia para desarrollar estrategias de optimizacion de la tecnología basada en el autoensamblado de los QDs.[19]-[20] El mecanismo para el transporte de portadores de carga en películas delgadas de QDs se puede modelar generalmente como un túnel activado térmicamente de nanocristal a nanocristal también, muy similar al conocido como "hopping",[21] y, por lo tanto, es fuertemente dependiente de la distancia entre partículas, la cual se rige por la longitud de los ligandos.[22] Por cierto, hay una multiplicidad de

factores que influyen en la dinámica de los portadores, como la presencia de niveles de energía profundos o trampas,[23] defectos cristalinos,[24] productos de oxidación[25] y polidispersividad de los nanocristales,[26] entre otros. Además, la interrelación de estos factores representa un obstáculo importante para la descripción de un mecanismo general para el transporte de portadores de carga en películas delgadas de puntos cuánticos. De hecho, los estudios en esta materia se llevan a cabo frecuentemente siguiendo enfoques demasiado específicos.

1.2 Objetivos y Metodologías

Los QDs de PbS permiten nuevas funcionalidades para aplicaciones de detección ópticas en las ventanas espectrales de telecomunicación, ofreciendo un nuevo grado de libertad para la ingeniería de las propiedades ópticas de materiales y la compatibilidad de sustratos para la producción de dispositivos rentables, de gran área y de alto rendimiento. El trabajo de investigación presentado en esta tesis se detiene en todas las etapas hacia la producción de fotodetectores basado en películas delgadas de QDs procesados en disolución, desde la optimización de los procesos (síntesis química y deposición de películas delgadas) hasta la fabricación y caracterización de estos dispositivos optoelectrónicos.

La mayoría de los esfuerzos se han dedicado a alcanzar los siguientes objetivos:

Síntesis de QDs de PbS

La morfología de los QDs, desde donde surgen sus propiedades ópticas, está directamente relacionada con las condiciones de síntesis. Por ejemplo, su tamaño y dispersión de tamaños se ven afectados drásticamente por la naturaleza del precursor y los parámetros de reacción.[27] Por estas razones hemos estudiado las condiciones de la síntesis y las características de las sustancias involucradas con el fin de ajustar las propiedades ópticas de los QDs de PbS en una solución coloidal estable (en el tiempo y bajo condiciones ambientales).

Metodologías: Los QDs de PbS se han sintetizado por el método de inyección en caliente que se analiza y describe en detalle en el Capítulo 3 de esta tesis. Los QDs de PbS en suspensiones coloidales se han estudiado por espectroscopia de absorción y fotoluminiscencia. Se han preparado, además, rejillas para microscopia electrónica, sobre las que se ha goteado tales suspensiones, para el estudio morfológico y estructural de los QDs de PbS mediante microscopia electrónica de transmisión de baja (TEM) y alta resolución (HRTEM), así como espectroscopia de rayos-X por energía dispersiva (EDX). Estas técnicas de caracterización morfológica y estructura están disponibles en el Servicio Central de Soporte a la Investigación Experimental (SCSIE) de nuestra universidad.

Formulación de una tinta de puntos cuánticos

Después de la síntesis, la disolución de los QDs de PbS obtenida debe optimizarse en sus propiedades físicas, químicas y reológicas para adaptarla al método de deposición seleccionado, como base para la producción de capas delgadas de alta calidad. Se presentarán y discutirán los resultados de este proceso de optimización.

Metodologías: Las nanotintas se han preparado mediante de la dispersión de QDs de PbS en octano, habiendo medido la tensión superficial de la dispersión por el método de la formación de gotas, así como el ángulo de contacto con las superficies a usar en el presente trabajo (vidrio/ITO/PEDOT y Si/SiO_2). Para estas medidas ha sido utilizado un método simple, implementado en nuestro laboratorio, basado en una lupa conectada a una CCD para almacenar la fotografía de la gota depositada sobre las superficies seleccionadas.

Métodos de procesado en disolución para la realización de solidos de QDs de PbS

Los métodos de procesado en disolución tienen la ventaja de ser simples y de bajo coste, a baja temperatura y rápidos, en comparación a las técnicas convencionales que se llevan a cabo en vacío. Estudiaremos la influencia de los métodos de deposición sobre la morfología de los sólidos de QDs con la prospectiva de su aplicación en fotodetección. De esta manera, dedicaremos una especial atención a las técnicas de deposición o impresión en continuo, concretamente a la técnica denominada “doctor blading”, que será la usada finalmente en este trabajo.

Metodologías: La técnica de deposición usada y optimizada para la producción de capas de QDs de PbS es conocida como “doctor blading” (cuchilla que extiende la nanotinta sobre el substrato). En el Capítulo 4 se describirá en detalle esta técnica enmarcándola/comparándola con otras técnicas de procesado en disolución. Las capas depositadas antes y después de procesos de intercambio de ligandos se han examinado por microscopia de transmisión de electrones (TEM) y microscopia electrónica de barrido (SEM) para corroborar el ordenamiento de los QDs en capas antes y después del intercambio de ligando. Se han utilizado también técnicas de difracción de rayos X estándar, para complementar el estudio de los QDs en disolución, así como a ángulos bajos para obtener información directa del ordenamiento reticular de los

QDs; también estos equipos forman parte del SCSIE, al igual que los equipos de microscopia electrónica. El intercambio de ligandos además se ha corroborado mediante espectroscopia FT-IR, mientras que la estabilidad y el efecto del ambiente sobre las capas (antes y después del intercambio de ligandos) se ha estudiado mediante XPS (técnica de la que es responsable el Dr. Juan F. Sánchez Royo, perteneciente a nuestro grupo).

Propiedades de solidos de QDs para aplicaciones optoelectrónicas

En fotodetectores basados en sólidos de QDs de PbS, la química de la superficie aplicada a estas película de nanocristales tiene profundos efectos sobre su comportamiento en fotodetección. De hecho, los estados superficiales de trampas influyen en la dinámica de los portadores de carga con resultados que pueden ser perjudiciales o beneficiosos para el rendimiento del dispositivo, dependiendo de la arquitectura del dispositivo seleccionado. En este documento, nos centramos en la química de la superficie de nanocristales de PbS y la estrategia para controlarla a fin de optimizar el funcionamiento y la eficiencia de los fotodetectores basados en sólidos de puntos cuánticos.

Metodologías: Los electrodos de los dispositivos fotoconductores se han fabricado sobre substratos de Si/SiO_2 mediante litografía óptica con máscaras para de electrodos de diferentes dimensiones y tipologías. Los electrodos de oro han sido depositados por evaporación térmica y "lift-off" (eliminación de la resina y del oro depositado sobre ésta) en nuestra sala gris, mientras que los dispositivos transistores de efecto campo (FET) se han adquirido de la casa OSSILA. Los fotoconductores se han caracterizado a través de curvas I(V) en oscuridad y bajo iluminación. En este caso también se ha usado luz monocromática mediante un sistema formado por una lámpara halógena de hasta 20 W (fijada a través de una fuente de corriente) y acoplada por fibra óptica a un monocromador cuya salida se focaliza sobre el área activa del dispositivo. La señal de éste se ha medido mediante un multímetro o bien con un amplificador sintonizado modulando la luz incidente. Estas técnicas se han montado a lo largo de esta tesis en nuestro laboratorio y se han descrito en el Capítulo 2, junto con la definición de los diferentes parámetros que caracterizan y definen el funcionamiento de los fotodetectores.

Optimización de los dispositivos optoelectrónicos para detección de luz

Los fotodetectores se pueden clasificar en función de su arquitectura y aprovechamiento de sus propiedades electro-ópticas (fotoconductividad, efecto fotovoltaico), que serán las que expliquen sus parámetros de eficiencia (fotoconversión, sensibilidad, respuesta temporal, etc.). En general, un adecuado equilibrio entre la velocidad de detección y la sensibilidad sería el mejor compromiso, dependiendo de los requisitos de la aplicación. El análisis de los mecanismos físicos subyacentes a los fotodiodos y a los fotoconductores servirá para explorar y valorar la potencialidad de estos dispositivos. En este trabajo, se prestará especial atención al ajuste de las propiedades del material fotoactivo a la nanoescala, a su caracterización y a la optimización de las figuras de mérito del dispositivo. La respuesta temporal se ha medido iluminando el dispositivo con un láser pulsado Nd:YAG de 1064 nm y un osciloscopio de 100 MHz.

Metodologías: Los fotodiodos de unión Schottky se consiguen depositando plata metálica por evaporación térmica (en nuestra sala gris) sobre capas de QDs de PbS previamente depositadas sobre substratos de Vidrio/ITO/PEDOT (ITO and PEDOT son electrodos transparentes, siendo el segundo un polímero conductor que permite obtener una mejor interfase con la capa de QDs y permite el transporte de huecos hacia el ITO). Los contactos de plata se han limitado a un área de 1 mm^2 mediante una máscara rígida metálica. Los fotodiodos de unión Schottky se han caracterizado de igual forma que los dispositivos fotoconductores, si bien iluminado por la parte del substrato de vidrio y midiendo de forma directa la fotocorriente generada en el fotodiodo con el amplificador sintonizado (ver Capítulo 2). Además, también se han medido las características C(V) a varias frecuencias usando un equipo LCR. La respuesta temporal se ha medido iluminando el dispositivo con luz monocromática incidente a 1550 nm modulada a 780 Hz y un osciloscopio de 100 MHz.

1.3 Publicaciones derivadas de esta tesis

La mayoría del trabajo desarrollado en esta tesis se ha publicado en los siguientes artículos (o como material suplementaria anexa a las publicaciones 1-2):

1. Maulu, J. Navarro-Arenas, P. J. Rodríguez-Cantó, J. F. Sánchez-Royo, R. Abargues, I. Suárez, J. P. Martínez-Pastor, ***Charge transport in trap-sensitized infrared PbS quantum dot-based photoconductors: pros and cons***, Nanomaterials, vol. 8, no. 9, 677 (18 pp.) (2018).
2. A. Maulu, P.J. Rodríguez-Cantó, J. Navarro-Arenas, R. Abargues, J. F. Sánchez-Royo, Raúl García-Calzada, and Juan P. Martínez Pastor, ***Strongly-coupled PbS QD-solids by Doctor-Blading for IR Photodetection***, RSC Advances **6**, 80201–80212 (2016). DOI: 10.1039/C6RA14782H. Impact factor 2016: 3.108
3. A. Maulu, P. J. Rodríguez-Cantó, and J. P. Martínez Pastor, ***Efficient photodetectors at telecom wavelengths based on thin films of lead sulfide quantum dots***, in the book "Physics, Chemistry and Application of Nanostructures (Proceedings of International Conference Nanomeeting – 2015)", World Scientific Pub. Co., ISBN 978-981-4696-51-7, pp. 556-559 (2015).

También se han presentado resultados parciales de la tesis en varias conferencias nacionales e internacionales:

- A. Maulu, P. J. Rodríguez-Cantó and J. P. Martínez-Pastor, ***Colloidal QD-solid photodetectors produced by doctor blading based on two configurations: nano-gap (MIM) vs Schottky/heterostructure,*** 8th International Conference on Quantum Dots, 11-16 May 2014, Pisa (Italy), Oral.
- A. Maulu, P.J. Rodríguez-Cantó, I. Suarez, R. Abargues, J.P. Martinez-Pastor, ***"Fabrication of solution-processed QD-solids by doctor blading technique and their application for photodetection"***, 4th International Colloids Conference, 15-18 June 2014, Madrid (Spain), Poster.
- A. Maulu, P. J. Rodríguez-Cantó, J. P. Martínez Pastor, ***Efficient photodetectors at telecom wavelengths based on thin films of lead sulfide quantum dots,*** Nanomeeting 2015, 26-29 May 2015, Minsk (Belarus), Oral.
- A. Maulu, P. J. Rodríguez Cantó, J. Navarro Arenas, R. Abargues and J. Martínez Pastor, ***Photodetectors at 1.3-1.7 μm Based on Thin Films of PbS Quantum Dots,*** **IX Reunión Española de Optoelectrónica** (IX Spanish Meeting of Optoelectronics), OPTOEL2015, Salamanca (Spain), 13-15 July 2015. Poster.

- J. P. Martínez Pastor, ***Efficient photodetectors at telecom wavelengths based on thin films of lead sulfide quantum dots,*** NANOSD Security and Defence 2015, 22-25 Septiembre Madrid. Ponencia oral.
- Alberto Maulu, ***Solution-Processed QD-solid by Doctor-Blading Based on PbS QD Nanoinks for the Fabrication of Photodetectors at Telecom Wavelengths***, Conferencia Española de Nanofotónica CEN 2016, 20-22 Junio, Valencia. Ponencia oral.

Los trabajos anteriores y la experiencia adquirida durante esta tesis también se han aplicado en la participación del doctorando en el siguiente trabajo de investigación:

- I. Suarez, E. Hassanabadi, A. Maulu, N. Carlino, C. A. Maestri, M. Latifi, P. Bettotti, I. Mora-Sero and J. P. Martinez-Pastor, ***Integrated Optical Amplifier-Photodetector on a Wearable Nanocellulose Substrate***, Advanced Optical Materials **6**, 1800201 (8 pp) (2018). DOI: **10.1002/adom.201800201**

1.4 Estructura de la tesis

El trabajo de investigación presentado en esta tesis tiene la siguiente organización:

El **Capítulo 2** presenta la física subyacente a la fotodetección en fotodiodos y dispositivos fotoconductores. Se introducen los factores implicados en fotoconductores basados en sólidos de puntos cuánticos de PbS. Se analizará a continuación su influencia en las características y el rendimiento de la fotodetección del dispositivo. Se prestará especial atención a las propiedades de capas delgadas de QDs de PbS y sus prerrogativas de aplicación. A continuación, el capítulo presenta las figuras de mérito más importantes para describir y evaluar la eficiencia de los fotodetectores. Finalmente, se presentará la configuración experimental utilizada para la caracterización optoelectrónica del dispositivo.

El Capitulo 3 comienza con una introducción a los efectos de confinamiento cuántico en la materia a la nanoescala (los puntos cuánticos), explorando el papel de los estados de superficie en los nanocristales. El método de inyección en caliente se analizará como base para realizar una investigación detallada del mecanismo de reacción subyacente a la formación de los nanocristales. Para ello, se describirán las rutas sintéticas para la producción de nanocristales de PbS. A partir de aquí, presentaremos sus propiedades y los procesos sintéticos que hemos abordado y optimizado para aplicaciones de fotodetección en el infrarrojo próximo (producción de QDs de PbS con tamaño adecuado y homogéneo). El capítulo finaliza con los resultados más relevantes de la caracterización de los QDs sintetizados en este trabajo.

El Capítulo 4 describe el uso de técnicas de procesado en de disolución para la producción de capas delgadas a partir de la tinta de QDs de PbS. Abordaremos la fabricación de películas autoensambladas sin defectos, con una gran capacidad de control del grosor de las películas y su homogeneidad sobre superficies grandes, concretamente usando el método “doctor blading” e ilustraremos su gran potencialidad. Es la primera vez que se usa esta técnica para generar supercristales de QDs y dispositivos optoelectrónicos con estas capas. Se describirá la formulación de las nanotintas de QDs de PbS y su optimización, de acuerdo con los parámetros de deposición por la técnica reseñada. A continuación, presentaremos los tratamientos de pasivación de los nanocristales depositados en capa delgada. El objetivo

de estos procesos es la substitución de los ligandos usados en la síntesis de los QDs por otros más cortos al fin de mejorar el acoplamiento electrónico entre los nanocristales y, por ende, la movilidad de los portadores de carga. El capítulo termina con la caracterización estructural y elemental de los nuevos sólidos derivados de los puntos cuánticos de PbS, prestando especial atención a la pasivación de su superficie y a la estabilidad frente a la exposición ambiental (efecto de oxidación, principalmente).

El Capítulo 5 analiza la influencia de la química superficial de los QDs sobre las propiedades de los sólidos de QDs. Más específicamente, veremos el efecto de los tratamientos realizados en estado sólido sobre las propiedades eléctricas de las capas de QDs, los cuales modifican la superficie del QD mediante el intercambio de ligandos con dos diferentes agentes pasivantes: ácido 3-mercaptopropiónico (MPA) y Yoduro de Tetrabutilamonio (TBAI). A continuación, describiremos la fabricación de dispositivos fotoconductores basados en sólidos de QDs de PbS y discutiremos sus propiedades eléctricas y electroópticas. Particularmente, estudiaremos la fotoconductividad en el dispositivo, cuyo origen, a baja potencia, viene determinada por la sensibilización debida a estados trampa, cuyos efectos sobre el transporte de carga y la fotodetección serán ampliamente analizados, mientras que a alta potencia viene limitada por la movilidad de los portadores. Finalmente, el análisis realizado para los dos tratamientos de intercambio de ligado permitirá definir la mejor ruta de procesamiento y establecer las limitaciones los fotodetectores fabricados.

El Capítulo 6 se dedica a la fabricación y a la caracterización de fotodiodos de unión Schottky basados en sólidos de QDs de PbS operando en la tercera ventana de longitudes de onda de telecomunicaciones. En el capítulo se detallarán la arquitectura de este dispotivio Schottky y los procesos de optimización llevados a cabo para alcanzar la máxima sensibilidad, una baja corriente de ruido y una respuesta de tiempo relativamente rápida. El rendimiento del dispositivo durante la exposición al aire a largo plazo se ha probado y evitado parcialmente mediante su encapsulación con polímero transparente, mostrando una gran estabilidad y reproducibilidad.

Finalmente, en las Conclusiones y Perspectivas Futuras se hace un resumen de los logros más relevantes de la presente tesis doctoral y la discusión de las perspectivas futuras en el campo de investigación de ésta: dispositivos optoelectrónicos basados en sólidos de QDs.

Chapter 1 Introduction: objectives and methods

Optical sensing and imaging underpin the transduction of our visual world into digital signals that can be stored, conveyed, and processed. Light detection has been traditionally facilitated by small-area, single-crystalline photodetectors, characterized by high cost, complexity and rigidity.

In the present work, we demonstrate a novel approach to photodetection based on solution-processed colloidal quantum dots. This material platform enables the production of large-area, low cost, flexible photodetectors.

In this chapter, several optoelectronic applications of are presented, with emphasis on photodetection. The fundamental properties of a photodetector relevant to telecommunication are then described. The state-of-the-art of photodetection applications are briefly reviewed, and advantages and disadvantages are discussed. The motivation for the present work is then set by the opportunities that arise from the proposed approach based on colloidal nanocrystals. Finally, this chapter concludes with the objectives and the organization of this thesis.

1.1 Optoelectronics for telecommunication applications

The concept of optoelectronic devices was first introduced during the second half of the 1980s but only with the new millennium it has grown to become one of the most prosperous research fields worldwide, mostly pushed by rapid development of the communications technology. In fact, with the internet traffic in continuous increase and the needs for miniaturization of digital electronic components, the copper-based technology could no longer satisfy the new requirements of telecommunications applications. Under this circumstance, optoelectronics will be a protagonist in modern communications applications due to the high-speed transmission and high efficiency it promises.

Nowadays, the long-distance data transmissions are mostly carried out in the spectral window between 1300 and 1550 nm, corresponding to the minimum optical loss for silica optical fibres. Therefore, as optoelectronic devices operating in this wavelength range can be connected to external servers without needs of wavelength conversion, new solution for light sources,[1],[2] optical modulators[3] and other passive components[4],[5] are intensively pursued.

Among the optoelectronic devices, the photodetector (PD) is located at the end of the optical path (receiver) with the function of convert light into electricity. The signal conversion quality then critically affects the overall performance of the entire system.

Traditionally, photodetection was facilitated by single-crystalline semiconductor-based devices, which have widely proved their performances with high carrier mobility, efficient light absorption, photo and thermal stability. However, monocrystalline-based technology has also important drawbacks, as high production costs, high-temperature processing, limited spectral range and complex lattice mismatch considerations for the integration into CMOS circuits. Moreover, single-crystalline semiconductors are precluded from application in flexible electronics due to the incompatibility of their growth conditions with the process setting required. Furthermore, the upscaling from silicon-wafer-area to larger-area applications is impeded due to the incompatibility of the Czochralski process and the roll-to-roll process on flexible substrates.

Solution-synthesized colloidal quantum dot

In the quest to find a solution to these limitations, QD-based optoelectronics, thanks to the QDs unique size-tuneable electronic and optical properties, represent one of the most interesting solutions towards unprecedented technological applications.

The potentiality of QD-optoelectronics appeared after the definition of QD synthesis by simple wet chemistry routes, as the hot injection method, where the precursors are dispersed in different flasks and then injected one into the other at a precise temperature. By the careful choice of the precursor concentrations, temperatures, reaction time, solvent and ligand selection, it is possible to produce QDs with the desired size and shape. Figure 3 reports the absorption of PbS CQDs where, by varying the dot diameter from 10 to 3 nm the absorption peak can be tuned from 1800 to 800 nm.[6]

Due to its unique size tuneable properties, PbS has been studied for a wide range of optical sensing applications as SWIR imaging for night vision,[7] photovoltaic energy conversion[8] and integrated in telecommunication devices as waveguides[9] and photodetectors.[10] In the work here presented, we have proposed PbS QDs as active material for photodetection applications, exploiting the possibility to address telecom wavelengths (near infrared, 1300-1600 nm).

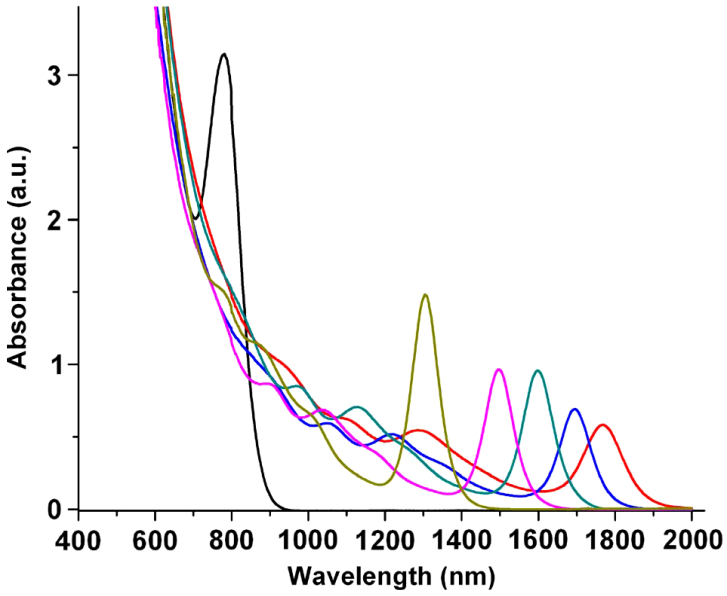

Figure 3: Absorption spectra of PbS colloidal quantum dots with sizes ranging from 10 nm (red) to 3 nm (black) in diameter.[6]

After the QDs synthesis and a post-synthetic procedure consisting in purification, isolation and redispersion in selected organic solvents, it is possible to produce a stable colloidal dispersion of the QDs. Then, after the optimization of its rheological properties, the solution is ready to be processed to produce QD thin films and, from here, optoelectronic devices.

As consequence, film deposition methods as drop casting,[11] spin coating[12] and dip coating,[13] among other techniques, have been contextually explored to fabricate QD-optoelectronic devices. Even demonstrating different advantages and disadvantages, these techniques enable the low-cost integration of QD thin films over rigid[10] and flexible[14] substrates with no lattice mismatch concerns.

In Figure 4, is reported an example of the solution processability of QDs on flexible substrate.[14] In this particular case is reported a photoconductor device for NO_2 gas sensing where PbS CQDs are spun onto a paper substrates previously patterned with interdigital Au electrodes. This is a proof of concept that shows the clear potentiality of CQDs in wearable sensing applications.

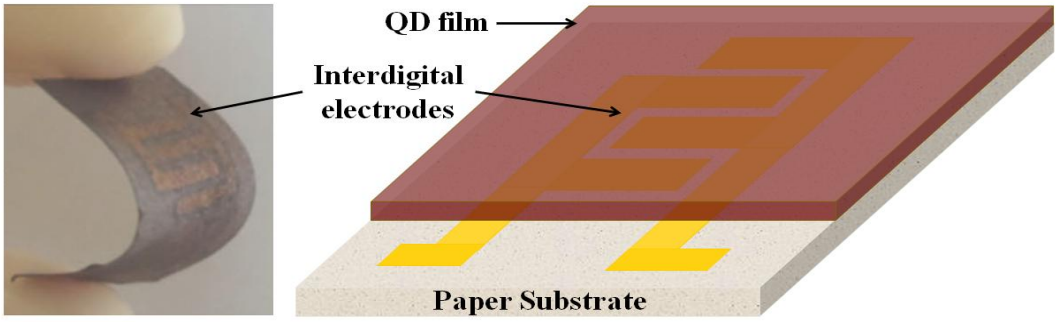

Figure 4: Example of flexible device for sensing application based on colloidal quantum dots.

Recently, important attention has been attracted by the capability of CQDs, to produce a nanocrystal self-assembling into ordered solid structures, also called “superlattices” or “QD-solids”.[15] These nanostructures, with characteristic charge transport[16] and optical properties,[17] can be considered as a novel type of semiconductor, whose behaviour depend on both, the individual nanoparticle nature and the interparticle interactions.[18] At this point, the confinement of carriers inside the QDs, besides giving the unique properties to the nanomaterials, represents a challenge to the efficient extraction and transport of charge carriers required by high speed telecommunication applications. In this context, the fundamental

study of the charge transport, from localized quantum-confined states to delocalized and hybridized states present in QD-solids, is of primary importance. The identification and characterization of the critical factors underlying the mobility of charge carriers is nowadays highly demanded to develop strategies for performance improvement of QD-solid-based technology.[19]-[20]

Indeed, the mechanism for charge carriers transport in the QD-solids can be generally modelled as thermally activated tunnelling from NC-to-NC, also known as hopping,[21] and is therefore strongly dependent on the interparticle distance, which is governed by the length of capping ligands.[22] By the way, there is a multiplicity of factors that influence the carrier dynamics, as trapping states,[23] nanocrystal defects,[24] oxidation products[25] and nanocrystals polydispersity,[26] among others. Moreover, the intercorrelation of these factors, represent an important obstacle towards the description a general mechanism of charge carrier transport in QD-solids. In fact, studies in this matter are more frequently carried out following a study case approach.

1.2 Objectives and Methods

Solution processable PbS CQDs enable new functionalities for photodetection applications at telecom spectral windows, offering a new degree of freedom for the engineering of material optical properties and substrate compatibility for the production of cost-effective, large-area and high-performance devices. The research work, presented in this thesis, face all the stages toward the production of solution-processed QD-solid photodetectors, form the optimization of the processes (chemical synthesis and thin films deposition) to the fabrication and characterization of these optoelectronic devices.

Most of the efforts have been expressed on the following subjects:

Synthesis of PbS QDs

The morphology of QDs from which arise their optical properties are directly related to the synthesis conditions. For instance, their size and size dispersion are affected dramatically by the precursor nature and reaction parameters.[27] We explore how to control the reaction conditions and the nature of the involved substances to tune the optical properties of PbS QDs in a stable (again time and ambient conditions) colloidal solution.

Methods: The PbS QDs have been synthesized by the hot injection method which is analysed and described in detail in Chapter 3 of this thesis. The PbS QDs in colloidal suspensions have been studied by absorption and photoluminescence spectroscopy. In addition, grids for electron microscopy, on which such suspensions have been dripped, have been prepared for the morphological and structural study of the PbS QDs by means of low transmission (TEM) and high resolution (HRTEM) electron microscopy, as well as energy dispersive X-ray spectroscopy (EDX). These techniques of morphological and structural characterization are available in the Central Service of Support for Experimental Research (SCSIE) of our university.

CQD Nanoink formulation

After the synthesis, the obtained dispersion of CQDs, needs to be optimized in its physical, chemical and rheological properties to better suit the of the selected deposition method, to produce high quality QD-solids. The results of this optimization process are presented and discussed.

Methods: The nanoinks have been prepared by dispersing PbS QDs in octane, having measured the surface tension of the dispersion by the method of droplet formation, as well as the contact angle with the surfaces to be used in the present work. (glass/ITO/PEDOT and Si/SiO_2). For these measurements a has been used simple method, implemented in our laboratory, based on a magnifying glass connected to a CCD where the photograph of the drop deposited on the selected surfaces was stored.

Solution processing methods for the formation of PbS-QD-solids

Solution processing methods have the advantage of being low cost, simple and fast compared to conventional vacuum-based techniques. We deeply explore the influence of the deposition methods over the QD-solids morphology in prospective of their photodetection application. In this view, we reserve special attention to the roll-to-roll compatible techniques, concretely the doctor blading technique.

Methods: The deposition technique used and optimized for the production of layers of PbS QDs is known as "doctor blading" (blade that extends the nanoink on the substrate). In Chapter 4 this technique will be described in detail and compared with other solution processing techniques. Layers deposited before and after ligand exchange processes have been examined by electron transmission microscopy (TEM) and scanning electron microscopy (SEM) to study the QD assembly in layers before and after the ligand exchange. Standard X-ray diffraction techniques have also been used, to analyse the QDs in solution, as well as at low angles to obtain direct information of the QDs packaging; these instrumentation facilities are also part of the SCSIE, as are the electronic microscopy equipment. The QD-solid ligand exchange treatment has also been verified by FTIR spectroscopy, while the stability and effect of the environment on the QD films (before and after the exchange of ligands) has been studied by means of XPS (technique whose responsible, the Dr. Juan F. Sánchez Royo, is member of our group).

QD-solid properties for optoelectronic application

In photodetectors based on PbS QD-solids, the surface chemistry applied to this film of nanocrystals has deep effects on the photodetection behaviour. Indeed, surface trapping states influence the charge carrier kinetics with detrimental or beneficial outcomes for the device performance, depending on the selected device architecture. Herein, we focus on the PbS nanocrystal surface chemistry and the strategy to control it to optimize the QD-solid-based photodetector performances.

Methods: The electrodes of the photoconductive devices have been manufactured on Si / SiO_2 substrates using optical lithography with masks for electrodes of different dimensions and types. The gold electrodes have been deposited in our gray room by thermal evaporation and "lift-off" process, consisting on the deposition of sacrificial layer which is developed and removed to form inverse patterns, then a gold layer is evaporated onto the surface and finally the sacrificial layer is removed. Field effect transistor devices (FET) have been purchased from the company OSSILA. The photoconductors have been characterized through I(V) curves under darkness and illumination conditions. In this case, monochromatic light has also been used by means of a system formed by a halogen lamp of up to 20 W (controlled by a current source) and coupled by optical fibre to a monochromator whose output is focused on the active area of the device. The signal of this one has been measured by means of a multimetre or with a tuned amplifier modulating the incident light. These techniques have been assembled throughout this thesis in our laboratory and, together with the definition of the different parameters that characterize and define the functioning of photodetectors, have been described in Chapter 2.

Photodetector engineering for optoelectronic performance optimization

Different photodetector devices can be distinguished by the electro-optical properties (photoconductivity, photovoltaic effect) and performance parameters (responsivity, detectivity, time&frequency response, etc.) arising from their specific architecture. Generally, a tread-off between detection speed and sensitivity would be the best compromise depending on the application requirements. The analysis of the physical mechanisms underlying photodiodes and photoconductors will serve to explore and valorise the potentiality of these devices. Herein, special attention will be given to the tuning of the

photoactive material properties at the nanoscale and the characterization and optimization of the device figures of merit.

Methods: Schottky photodiodes are achieved by depositing metallic silver by thermal evaporation (in our gray room) on layers of PbS QDs previously deposited on Glass/ITO/PEDOT substrates (ITO and PEDOT are transparent electrodes, the second being a conductive polymer that allows to obtain a better interface with the layer of QDs and allows the transport of holes towards the ITO). The silver contacts have been limited to an area of 1 mm^2 by a rigid metal mask. Schottky photodiodes have been characterized with the same techniques used for photoconductive devices, even if in this case the devices were illuminated through the glass substrate and directly measuring the photocurrent generated in the photodiode with the tuned amplifier (see Chapter 2). In addition, the C(V) characteristics have been measured at various frequencies using an LCR equipment. The temporal response has been measured by illuminating the device with incident monochromatic light at 1550 nm modulated at 780 Hz and a 100 MHz oscilloscope.

1.3 Publications derived from this thesis

Most of the work in this thesis have been published in the following papers (and supporting information annexed to publications 1-2):

4. Maulu, J. Navarro-Arenas, P. J. Rodríguez-Cantó, J. F. Sánchez-Royo, R. Abargues, I. Suárez, J. P. Martínez-Pastor, ***Charge transport in trap-sensitized infrared PbS quantum dot-based photoconductors: pros and cons***, Nanomaterials, vol. 8, no. 9, 677 (18 pp.) (2018).
5. A. Maulu, P.J. Rodríguez-Cantó, J. Navarro-Arenas, R. Abargues, J. F. Sánchez-Royo, Raúl García-Calzada, and Juan P. Martínez Pastor, ***Strongly-coupled PbS QD-solids by Doctor-Blading for IR Photodetection***, RSC Advances **6**, 80201–80212 (2016). DOI: 10.1039/C6RA14782H. Impact factor 2016: 3.108
6. A. Maulu, P. J. Rodríguez-Cantó, and J. P. Martínez Pastor, ***Efficient photodetectors at telecom wavelengths based on thin films of lead sulfide quantum dots***, in the book "Physics, Chemistry and Application of Nanostructures (Proceedings of International Conference Nanomeeting – 2015)", World Scientific Pub. Co., ISBN 978-981-4696-51-7, pp. 556-559 (2015).

Partial results were also presented in several national and international conferences:

- A. Maulu, P. J. Rodríguez-Cantó and J. P. Martínez-Pastor, ***Colloidal QD-solid photodetectors produced by doctor blading based on two configurations: nano-gap (MIM) vs Schottky/heterostructure,*** 8th International Conference on Quantum Dots, 11-16 May 2014, Pisa (Italy), Oral.
- A. Maulu, P.J. Rodríguez-Cantó, I. Suarez, R. Abargues, J.P. Martinez-Pastor, ***"Fabrication of solution-processed QD-solids by doctor blading technique and their application for photodetection"***, 4th International Colloids Conference, 15-18 June 2014, Madrid (Spain), Poster.
- A. Maulu, P. J. Rodríguez-Cantó, J. P. Martínez Pastor, ***Efficient photodetectors at telecom wavelengths based on thin films of lead sulfide quantum dots,*** Nanomeeting 2015, 26-29 May 2015, Minsk (Belarus), Oral.
- A. Maulu, P. J. Rodríguez Cantó, J. Navarro Arenas, R. Abargues and J. Martínez Pastor, ***Photodetectors at 1.3-1.7 μm Based on Thin Films of PbS Quantum Dots*****, IX Reunión Española de Optoelectrónica** (IX Spanish Meeting of Optoelectronics), OPTOEL2015, Salamanca (Spain), 13-15 July 2015. Poster.

- J. P. Martínez Pastor, ***Efficient photodetectors at telecom wavelengths based on thin films of lead sulfide quantum dots,*** NANOSD Security and Defence 2015, 22-25 Septiembre Madrid. Ponencia oral.
- Alberto Maulu, ***Solution-Processed QD-solid by Doctor Blading Based on PbS QD Nanoinks for the Fabrication of Photodetectors at Telecom Wavelengths***, Conferencia Española de Nanofotónica CEN 2016, 20-22 Junio, Valencia. Ponencia oral.

The previous works and experience gained during this thesis have been also applied in the participated to this research work:

- I. Suarez, E. Hassanabadi, A. Maulu, N. Carlino, C. A. Maestri, M. Latifi, P. Bettotti, I. Mora-Sero and J. P. Martinez-Pastor, ***Integrated Optical Amplifier-Photodetector on a Wearable Nanocellulose Substrate***, Advanced Optical Materials **6**, 1800201 (8 pp) (2018). DOI: **10.1002/adom.201800201**

1.4 Thesis Structure

The research work presented in this thesis is organized as follows:

Chapter 2 introduce the physics underlying the photodetection in photodiodes and photoconductors devices. The factors involved in the photoconductivity in QD-solid-based photoconductors are introduced. Their influence on the device photodetection characteristics and performances is then discussed. Special attention will be devoted to the PbS QD-solids properties and its application prerogatives. Following, the chapter introduce the most important figures of merit set to describe and evaluate photodetection performances. In conclusion, the experimental setup utilized for the device optoelectronic characterization will be presented.

Chapter 3 begins with an introduction to the quantum confinement effects in matter at nanoscales, exploring the role of nanocrystal surface states. Herein, the hot injection method is closely discussed with a detailed investigation of the reaction mechanism underlying the nanocrystals formation. The wet synthetic routes for the production of PbS nanocrystals are then outlined. From here, we present the PbS CQD properties and synthetic processes we have approached and optimized to target IR photodetection applications. The experimental steps followed for the production of monodispersed PbS CQDs to address the third telecommunication window are then reported. The chapter finishes with the characterization of the PbS CQDs synthesized in this work.

Chapter 4 describe the use of solution processing techniques for the production of PbS QD-solid films from the PbS nanoink. We addressed here the fabrication of flawless self-assembled QD films, with high tunability over the films thickness, and homogeneity over large surfaces. Hence, we illustrate the potentiality of doctor blading as QD-solid roll-to-roll compatible deposition method. The first solution-processed QD-solid produced by doctor blading is here reported. The formulation of the ad-hoc PbS QD-nanoink, optimized accordingly to the deposition parameters is described. We then present the post-processing QD-solid passivating treatments, as ligand exchange processes aimed to improve the electronic coupling among QDs. The chapter is then closed by the structural and elemental characterization of the

produced QD-solids with specific attention to the QD surface passivation and stability against ambient exposure (oxidation effect, mainly).

Chapter 5 discuss the influence of the QD surface chemistry over the QD-solid properties and it follows with the processing route we explored to contextually modify the nanocrystal surface. More specifically, we approached solid state treatments to tune the electrical properties of QD-solids, modifying the QD surface by ligand exchange treatment with two different passivating agents: 3-mercaptopropionic acid (MPA) and tetrabutylammonium iodide (TBAI). Following this path, we investigate how the modifications induced on the QD surface influence the dynamics of charge carriers inside the QD-solid. Photoconductor devices based on PbS QD-solids after such ligand exchange procedures are here presented and their electrical, optical and electro-optical properties discussed. The role of oxides species and the subsequent trap sensitization affecting charge transport and photodetection is herein analysed. The chapter finally define the best processing route to improve photo-sensitivity and detectivity.

Chapter 6 is devoted to the fabrication and characterization of PbS QD-solid-based Schottky photodiode operating in the third window of telecom wavelengths. The chapter details the Schottky architecture and the optimization processes carried out for the ultimate achievement of high sensitivity, low noise current, and relatively fast time response. The device performances during long-term air exposure has been deeply tested, showing high stability and reproducibility.

Conclusions and Outlooks: a summary of the achievements of present work and the discussion of the prospects in the research field are given in this final section of the present thesis.

Chapter 2 Photodetectors Working Principles and Figures of Merit

With this thesis work we approach photodetection at telecom wavelengths with QD-solid-based optoelectronic devices. In particular, photodetector devices can be classified in two categories: photoconductors and photodiodes.

To understand the properties required from the photoactive material with respect to desired the device performance, the physical mechanism underlying the photodetection is here discussed. Further attention is dedicated to the influence of the device architecture on the photodetection mechanism.

The chapter then continues with the description of the figures of merit formulated to evaluate and compare the photodetectors performances.

The chapter is closed with the description of the experimental setups we adopted to QD-solid-based photodiodes and photoconductors optoelectronic performances.

2.1 Theory of photodiode and photoconductor devices

In semiconductor-based photodetectors, upon illumination, the conductivity of the material changes due to the variation of carrier mobility or carrier density, or both.[28] Indeed, this increment of conductivity, namely photoconductivity, is mostly attributed to the photogeneration of electron-hole pairs resulting in a carrier density increase.[28],[29]

In photodetectors, the semiconductor constitutes the photoactive component of the device and its band-gap energy define the light wavelength range of photodetection. When the semiconductor adsorbs a photon of energy greater than or equal to its band-gap, an electron will be promoted from the valence band to the conduction band with the consequent generation of a hole in the valence band, as illustrated in Figure 5.

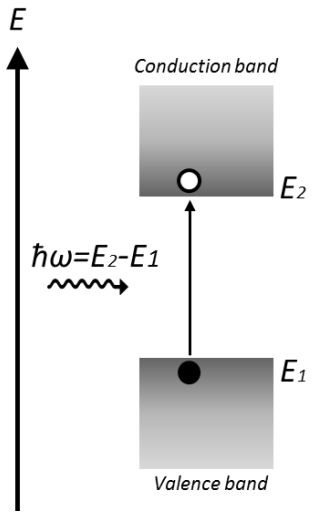

Figure 5: Scheme of photon absorption and electron-hole generation in semiconductors

In an ideal case, photogenerated electron – hole pairs can be collected at the electrodes in contact with the semiconductor under the influence of an internal or external electric field, giving rise to a photocurrent. Now, based on the nature of this electric field that determines the collection of charge carriers, we can draw the differences between photodiode and photodetector devices.

A Photoconductor consist on a semiconducting material deposited between two ohmic electrodes, in which the voltage bias applied to the metal contacts create the electric field that allows the collection of the

charge carriers. A photodiode, instead, is in the most common cases constituted by a p-n, p–i–n or a Schottky junction where an intrinsic electric field at the junction has the function of separate and sweep out the charge carriers towards the electrodes.

2.1.1 Photocurrent in Photodetectors

A closer look to the physical mechanisms inherent the photodetection of photoconductor and photodiode is now necessary to define each device characteristics.

The photoconductor architecture typically consists in a semiconductor material and two metal ohmic contacts to form a two-port electrical device (Figure 6). When the semiconductor is illuminated, the photogenerated charge carriers drift across the material towards the contacts generating a primary photocurrent.

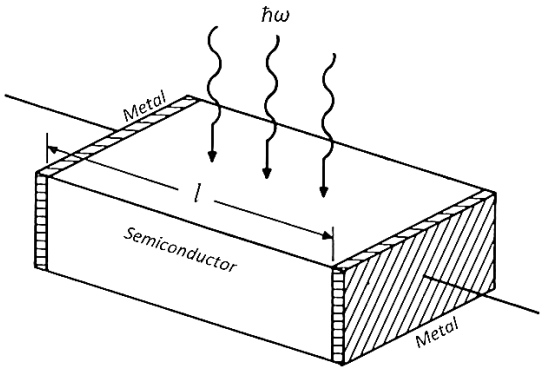

Figure 6: Schematic representation of a photoconductor device.

Photoconductivity in these semiconductor devices principally originates from this primary photocurrent, but also has the contribution of a secondary photocurrent due to the injection of charge carriers from the metal electrodes. The primary photocurrent governs the *EQE* while the secondary governs the photoconductive gain *G* which is defined as the ratio of circulated carriers per absorbed photon, it can be described has it follows:[30]

$$G = \frac{\tau_{lt}}{\tau_{tt}} = \frac{\tau_{lt} V \mu}{l^2} \qquad 1$$

Where τ_{lt}, τ_{tt} and μ are the minority carrier lifetime, transit time and mobility of charge carrier, l is the distance between the electrodes and V is the voltage bias used to create an electric field $F = V/l$. As evidenced by eq. 1 for a given semiconductor material the distance between the electrodes is a crucial parameter to optimize in order to increase the gain that contribute to the photocurrent.

Photodiodes, instead, are constituted by a junction between two different semiconductors (heterojunctions), or a semiconductor with opposite doping levels (homojunction), or a semiconductor and a rectifying metal contact (Schottky junction, as depicted in Figure 7).

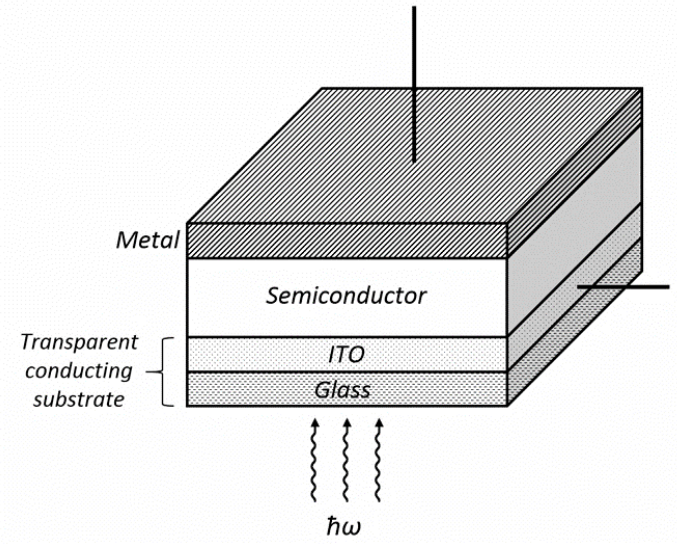

Figure 7: Schematic representation of a Schottky photodiode device.

In each case, the working principle is based on the separation of the photogenerated electron-hole pairs by the action of the built-in electric field. The charges will be then transported to the respective electrodes for the extraction. In photodiodes the photoconductive gain contribution to the photocurrent is absent as no external voltage is contemplated, so their quantum efficiency is limited to one carrier extracted per absorbed photon. Anyway, since in photodiodes the temporal response is mainly (for very thin

semiconductor films) determined by the transit time of carriers through the depletion layer, they are often faster than photoconductors.

2.2 Dynamics of Charge Carriers in Photodetectors

2.2.1 Photoconductors

As previously discussed, the photodetector gain is directly influenced by the carrier lifetime, transit time and mobility. In the real case of a PbS QD-solid semiconductor the travel of electrons and holes is influenced by states energetically located within the QD bandgap. We can discriminate intragap states in two main categories: sensitizing centres and trapping centers.[31]

Trapping centres lie close to the middle of the semiconductor band gap and determines the Shockley-Hall-Read generation-recombination mechanism, where electrons (holes) can be emitted and captured from the conduction (valence) band. This mechanism shortens the effective carrier lifetime, producing a decrease in the overall photoconductive gain of the device.[32],[6]

Sensitizing centres instead, are identified with states located energetically close to the conduction or valence bands and exhibit dissimilar capture coefficient for one carrier respect to the other. Based on this behaviour, sensitizing centres can prolong the effective carrier lifetime selectively, capturing one type of carrier while letting the other relatively free to move to the photoconductor electrode.[33] Under this condition, in the photoconductor with such a net imbalanced charge that, under the external electric field, will determine the photocurrent from the electrode to the semiconductor. This secondary photocurrent, due to the injection of charge carriers from the metal, can finally results in a photoconductive gain (G) when an external electric field is applied.[30],[34] Under high illumination intensity, when the density of excited carriers is equal or higher than the density of sensitizing centres, is possible to observe the saturation of the trapping centres.[35] Under this condition the photocurrent gain would decrease with linear dependence of the illumination power. However, while increasing the photocurrent gain, the action of sensitizing centres over the carrier lifetime limits the temporal response of the device.[36] This effect can be quantified considering that the lifetime of a trapped carrier increases with the energy depth, the concentration and the capture cross-section area of the traps. A deep study in this matter has been reported by Rose et al in the book “Concepts in Photoconductivity and Allied Problems”. Nevertheless, the nature of this trapping

centres is not yet fully understood,[37], but is commonly related to unbalanced binding between passivating molecules and the QD surface atoms or off stoichiometry arrangement of atoms at the QD surface.[30] The control over these parameters related to the sensitizing centres can give a certain control over the equilibrium between photoconductive gain and response time in photoconductors based on QD-solids.

We can conclude that QD-based photoconductors due to their configuration are more suitable for the achievement of high gain better than high-speed response and a larger frequency band-width can would be achieved with a more suitable architecture as, for instance, Schottky photodiodes.

2.2.2 Photodiodes

In photodiodes the charge carriers after photoexcitation need to cross the regions that constitute the multilayer architecture of the device (Figure 7) to be collected, therefore the device thickness is a critical parameter for the carriers to traverse these layers with a transit time shorter than their lifetime. In particular Schottky photodiodes, fabricated by the selection of a suitable metal/semiconductor interface, generate a built-in field that may be used to extract the photogenerated holes and electrons.[38] With a metal electrode with work function lower than the work function of a p-type semiconductor the device will manifest a characteristic Schottky barrier and the resulting rectifying properties.

To reduce the dark current Schottky devices can also incorporate both electron and hole blocking layers to suppress charge injection from the conducting electrodes. Schottky photodiodes can thus rely on a low noise current operating at zero applied bias or also with a small external reverse bias, which would improve both the EQE and the 3-dB bandwidth.[39] To achieve the maximum performances of the photodiode, some device structural parameter need to be optimized. First, it is necessary to define an active layer thickness that guarantee the maximum depletion of the semiconductor volume. Simultaneously, the metal/semiconductor interface must generate a potential barrier that prevents carrier injection from device electrodes. In this way the noise level can be reduced and the limit of the device dynamic range increased, hence optimizing the photo-conversion efficiency while limiting dark current signals.[40]

2.3 Photodetectors Figure of Merit

In this section we present the figures of merit commonly used to evaluate and quantitatively compare the performances of photodetector devices regardless of their architecture.[41],[42]

2.3.1 Responsivity

The responsivity is the parameter that quantify the electrical signal output given by the device per optical power input. This figure of merit represents the ratio of photocurrent to incident light power irradiating the active layer of the detector, it is given by the expression:

$$R = \frac{I(\lambda)}{P(\lambda)} = \frac{\eta e \lambda}{hc} \approx \frac{\eta \lambda}{1.24\ (nm \times W/A)} \qquad 2$$

$I(\lambda)$ is the photocurrent measured in amperes and $P(\lambda)$ is the incident optical power measured in watts (both as a function of the wavelength λ measured in nm), e is the electron charge, h the Planck's constant c the speed of light, η the quantum efficiency.

We can also consider the case where photoconductive gain contribute to the responsivity as:

$$R(\lambda) = \frac{\eta e \lambda}{hc} \frac{1}{\sqrt{(1+\tau^2\omega^2)}} G \qquad 3$$

Where, τ^2 is the time constant, ω^2 is the electrical modulation frequency, and G is the photoconductive gain.

2.3.2 Quantum Efficiency

The **external quantum efficiency (EQE)** measures the efficiency that the incident number of photons on the photodetector results in the generation of electron-hole pairs and the proportion of them collected to

produce photocurrent (i.e., the percentage of incident photons that contribute to photocurrent). The expression for the EQE of a photodetector in photovoltaic mode is given by:

$$EQE(\lambda) = \frac{R(\lambda)}{\lambda}\frac{hc}{e} = \frac{1240\,R(\lambda)}{\lambda}\ (\lambda\ in\ nm) \qquad 4$$

The **internal quantum efficiency (IQE)** is related to EQE, but dividing by *1-R*, where *R* is the reflectance at the light input surface of the photodetector.

2.3.3 Noise Equivalent Power

The noise equivalent power (NEP) is a measure of the power sensitivity of a photodetector.

Considering that the minimum detectable optical signal power, is associated to the responsivity of the photodetector, and that the produced electrical signal, must be higher than the noise current level, the signal to noise ratio (SNR) may be defined as:

$$SNR = \frac{RP}{i_n} \qquad 5$$

where *R* is the responsivity, *P* the input power and i_n is the noise signal.

Consequently, NEP may be defined as the level of incident light power that generates a photocurrent equal to the noise current (i.e., power that yields SNR = 1):

$$NEP = \frac{i_n}{R} \qquad 6$$

2.3.4 Specific Detectivity

The general definition for the specific detectivity (D^*) is equal to the reciprocal of the NEP normalized per square root of the photodetector area (A) and frequency bandwidth (related to the integration time in detection):

$$D^* = \frac{\sqrt{AB}}{NEP} = \frac{\sqrt{ABR}}{i_n} \qquad 7$$

D^* is expressed in Jones (cm $Hz^{1/2}$ W^{-1}) and may be also interpreted as the *SNR* produced by a detector area of 1 cm^2 under 1 W of optical power stimulation and 1 Hz of electrical bandwidth.

2.3.5 Noise in Photodetectors

Noise, defined as spontaneous fluctuations of current or voltage (depending on the photodetection mode), it is present in all semiconductor devices. The device type, its manufacturing process and operating condition are related to the nature of these signal fluctuations. Different noise sources can be identified for each device, and taken all together constitute the so-called inherent noise current of the device.

Thus, the inherent noise in semiconductor devices can be considered as an important parameter for performance and quality evaluations. The most important sources of noise in photodetectors can be identified as: thermal noise, shot noise, generation-recombination noise and 1/*f* noise.

Thermal Noise

Thermal noise, also known as Johnson noise, is due to random motion of charge carriers caused by thermal excitation. This random motion of carriers creates a fluctuating voltage on the terminals of each

resistive element of the device. The consequent internal noise current can be described by the Nyquist Equation:[28]

$$\overline{i_{th}^2} = \frac{4\,kT\,B}{R} \qquad 8$$

Where *k* is the Boltzmann constant, *T* is the absolute temperature, *B* is the electrical bandwidth and *R* the resistance of the detector. The thermal noise is approximately white, it means that its power density $dP_n/dB = kT$ is nearly independent from frequency.

The spectral density function of the equivalent voltage thermal noise is given by:

$$S_{th} = 4\,kT\,R \qquad 9$$

Since this spectral density is usually constant up to 1 THz and proportional to temperature and resistance of the elements, it can be used to evaluate the quality of contacts and connections of the device and its most suitable (or limit) operating temperature without introducing appreciable noise.

Shot Noise

As a quantum noise effect, the shot noise can be associated to the discreteness of photons and electrons. It arises from the occurrence of photon absorption events in a photodetector, but also due to the injection of charge carriers of high thermal energy through the device potential barriers (for instance, a metal-semiconductor junction).[43] These random processes are at the origin of the shot noise current that is given by the relation:

$$\overline{i_{sh}^2} = 2ei_DB \qquad 10$$

where *e* is the electron charge, i_D is the dark current flowing in the device and *B* is the electrical bandwidth, as in previous definitions.

Also, the shot noise is a white noise as its spectral density function is temperature independent and proportional to the dark current:

$$S_{shi} = 2ei_D \qquad 11$$

This relation can be used to evaluate parasitic leaking resistances of photodiodes as Zener diodes and Schottky diodes.[44]

Generation Recombination Noise

Generation-recombination noise results from statistical fluctuation in the rate of generation and recombination of carriers generated either by optical excitation or thermal generation. This signal fluctuation due to variations of the carrier lifetime causes a random population and depopulation of trap states. This phenomenon also introduces a random barrier modulation across the charge transport path resulting in an additional noise as observed in multi-crystalline photoconductors.[6] The current noise expression for *G-R* noise is:

$$i_{gr} = 2eG\sqrt{B(N_{ph} + N_{th})} \qquad 12$$

where G is the photoconductive gain, N_{ph} and N_{th} are the number of optically and thermally generated carriers, respectively. Unlike thermal and shot noise that are white noises, *G-R* noise spectrum is expected to follow the temporal/frequency spectrum limited by the carrier lifetime (τ) associated to the traps that cause the generation-recombination noise:

$$\frac{S_{gr}(\omega)}{N^2} = \frac{(\overline{\Delta N})^2}{N^2} \cdot \frac{4\tau}{1+(\omega\cdot\tau)^2} \qquad 13$$

where ω is the working frequency, N the average number of free carriers and ΔN the variance of charge carrier number.

1/*f* noise

1/f noise, characterized by the power spectral density function, which is inversely proportional to the frequency of the signal, is always present in semiconductor devices. It is generally attributed to several independent fluctuations with an exponential distribution of characteristic times. In single crystal devices, 1/f noise is usually lower than other noise currents except for very low frequency (100–1 kHz). Contrarily, in devices based on nanocrystals it represent the dominant noise source over a very wide range of frequencies.[45] It is commonly associated to the presence of structural defects,[24] and traps states[23] that influence the charge carriers dynamics.

In the specific case of colloidal quantum dot infrared photodetectors, the 1/f noise originates from to carrier's mobility fluctuations in the hopping regime, representing a limitation factor for the detectivity performances of the detector.[46]

2.4 Experimental Setups

In the following we describe the experimental setups used in the present work for the optoelectronic characterization of produced photodetectors. As excitation source we use a halogen lamp (20 W) coupled into a DeltaNu DNS-300 monochromator (grating of 600 g/mm blazed at 1200 nm) through an optical fibre. The halogen lamp is alimented by a programmable power supply to enable measurements with tuneable illumination intensity. The optical power, impinging on the active area of the detector, is obtained by dividing the active area of the device by the collimated beam area and multiplied for the total power measured by a Newport's DET-L-GE-T-C calibrated Ge photodetector. Then, the light is mechanically chopped at the frequency of interest and focused on the photodiode backside through the glass substrate or to the photoconductor surface using a 10x objective. The device photovoltage/photocurrent is directly measured in photodiodes using a Stanford Research Systems SR810 DSP lock-in amplifier, as depicted in Figure 8. In the case of the photoconductor detectors the setup is slightly different (Figure 9), where a programmable voltage source Keithley 230 is used to apply a voltage bias to the device, connected in parallel with a load resistor of 1 MΩ and with a capacitor of 0.1 μF in series with the lock-in amplifier (cutting the entrance of DC signal in the amplifier), as shown in Figure 9b.

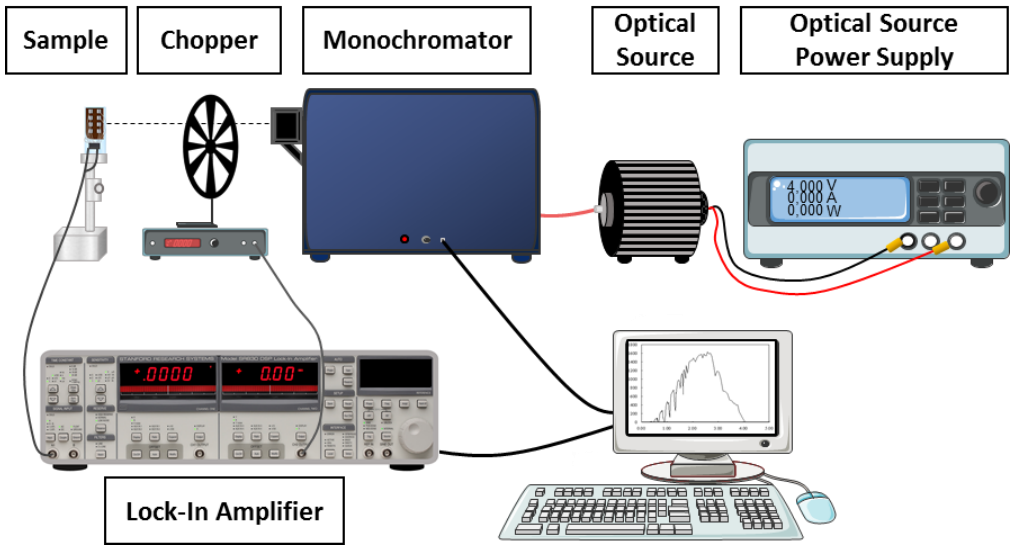

Figure 8: Experimental setup for responsivity measurement of photodiodes.

The setups for the characterization of photodiodes (Figure 8) and photoconductors (Figure 9) are slightly different. In fact, for the characterization of photoconductors, to the setup in Figure 8 is added a programmable voltage source Keithley 230, to apply bias voltages to the device, in parallel with a load resistor of 1 GΩ and with a capacitor of 0.1 μF in series with the lock-in amplifier Figure 9b. This circuit had the function of suppress the DC current signal in lock-in amplifier measurements.

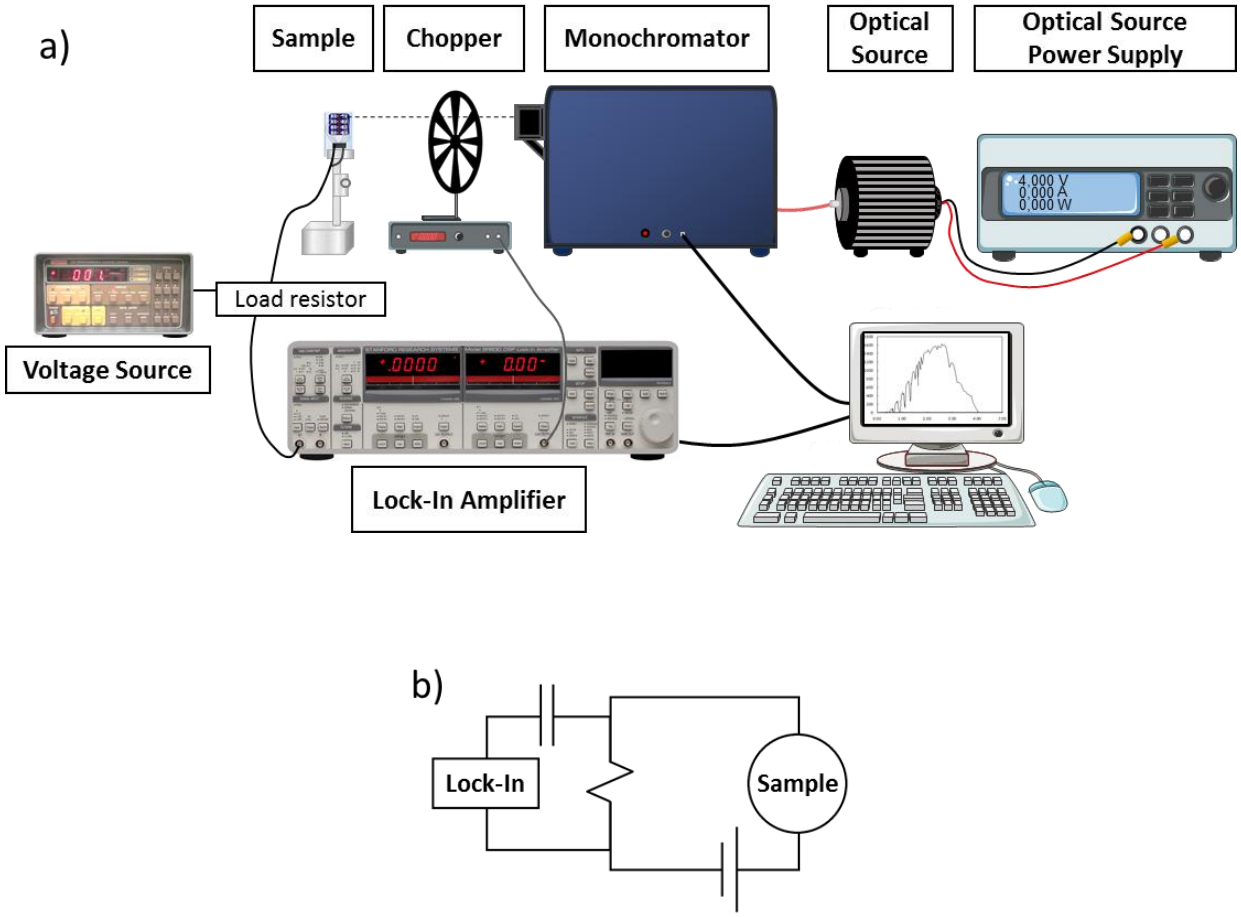

Figure 9: a) Experimental setup for responsivity measurement of photoconductors; b) Detail of the circuit containing the load resistor.

In Figure 10 is depicted the experimental setups used to study the current-voltage behaviour of the photodetectors by using a Keithley 2400 source measurement unit. We used this setup with different excitation source: monochromatic light of λ = 820/820 nm and λ = 1550 nm, solar simulator (AM1.5 conditions) or white light from a tungsten halogen lamp.

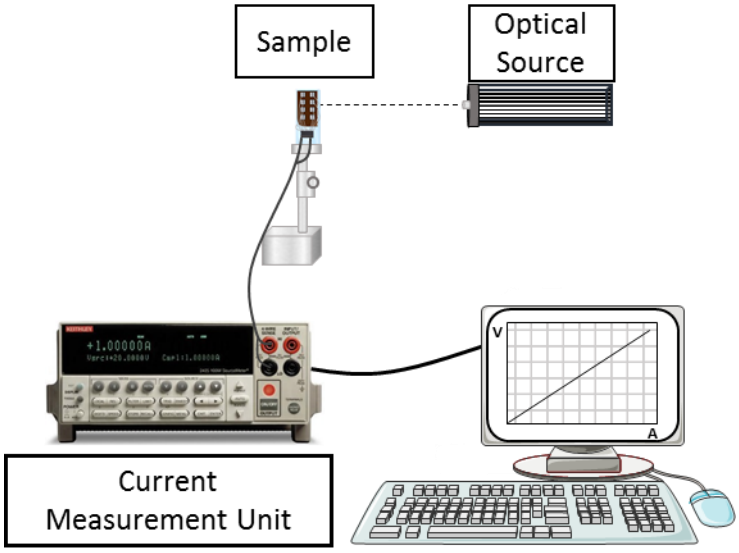

Figure 10: Experimental setup for I/V measurement

Capacitance–frequency and capacitance–voltage measurements were performed using a LCR Meter model 1920 connected in series with the studied photodetector.

Chapter 3 Colloidal Quantum Dots

During the last two decades colloidal NCs have attracted the attention of the scientific community, mostly due to their impressive electronic,[47] catalytic,[48] and optical properties.[49] In this respect, synthetic routes for the production of colloidal semiconductor nanocrystals had so far shown unseen advantages.[50],[4] The most fascinating feature of CQDs is represented by possibility to manipulate the quantum confinement in the NCs, and the related optical and electric properties, by tuning their size,[24] shape[51] and surface states.[27] With this aim, the understanding of the complex mechanisms underlying nucleation and growth of colloidally synthesized QDs has been the focus of many research activities.[52],[53],[54]

The chapter after briefly introducing the principles of the quantum confinement in semiconductors, reviews the more efficient routes reported for the synthesis of high-quality size tuneable PbS CQDs.

Here we examine how the variables involved during the colloidal synthesis influence, each one with its own weight, the NCs morphology and optical properties. The chapter concludes with the synthesis of PbS CQDs and their characterization.

3.1 Quantum confinement in Semiconductor nanocrystals

The concept of "quantum dot" has been defined for the first time by Ekimov at the beginning of 1980s,[55] describing the confinement of electrons and holes in QDs as due to smaller potential energy inside the QD than in the surrounding matrix. In fact, differently to free electrons traveling through vacuum, electrons in a semiconductor experience a periodic potential caused by the atoms of the crystal lattice. A defining characteristic of semiconductors is the energy band gap (E_g), assimilable to the minimum energy required to promote an electron from the valence band to the conduction band. Thus, the absorption of a photon with energy equal to E_g would bring to the promotion of an electron to the conduction band leaving a vacancy (a positively charged electron hole) in the valence band. The lower energy state for an electron-hole pair is called exciton. This bound state can experience the relaxation of the excited electron back to the valence band with the re-emission of a photon (radiative recombination) or, in the presence of an electric field, the dissociation into separate charges. The length of the exciton bound state is the so-called Bohr radius (a_0), a material intrinsic property which ranges approximately from 2 to 50 nm depending on the semiconductor.[56]

When the semiconductor crystals size reaches its Bohr radius length, the exciton will be confined in all three spatial dimensions, leading to a phenomenon known as quantum confinement.[57] Consequently, its electronic structure and optical properties can be tuned by varying the size of the nanocrystal resulting in larger energy gaps with decreasing sizes until the appearance of discrete energy levels. Such a semiconductor nanostructure in which the exciton is confined in all three dimensions is called Quantum Dot (QD). It is worth noting that a_0 and E_g are correlated, so that materials with narrower E_g have larger a_0 and will thus experience quantum confinement at larger NC sizes. Once the quantum confinement condition is fulfilled, an additional adjustment of the energy band gap can be obtained via the control over the shape of the nanocrystals. This corresponds to a change in number of confinement dimensions for the exciton inside the nanocrystal. In QDs the confinement is three-dimensional but it can be reduced to two dimensions or just one dimension with nanostructures, respectively called quantum wires and quantum wells.

3.1.1 QD Surface Properties

The quantum confinement effect on QDs derive principally from the properties of their crystalline core, but in reality the whole particle, surface included, participate on the energetic system that govern the dynamics charge carriers.[58] On the QD surface, the atoms constituting the crystal facet are not fully bonded, as consequence a periodic array of unpassivated orbitals[54] may create to secondary band structure of two-dimensional symmetry.[59] This surface states may energetically lie on the band gap of the core levels, acting as trapping centres for the photogenerated charge carrier.[60] To minimize the concentration of these localized states and improve the stability of the nanocrystals, chemical strategies are commonly approached to passivate QD dangling bonds.[61],[60]

3.2 QDs wet chemistry approach

During the past two decades strong efforts have been put on the development of synthetic routes to produce colloidal semiconductor nanocrystals. Path such as hydrothermal synthesis,[53] co-precipitation,[62] sol-gel processing,[63] microemulsions[62] and the hot-injection method[64] have been intensively explored. These techniques have shown to enable low-cost, solution-processable, high quality QDs with tailored size and shape that results in tuneable optical properties. Among them, the hot-injection method most of the attention since it demonstrated to be a suitable for the production of high quality QD dispersions in highly scalable manufacturing processes.[65]

Organometallic, high-temperature NCs synthesis was introduced in the early 1990s[58] and have been intensively developed to achieve nanocrystals with accurate morphological control and low size dispersion.[66],[67] Most of the attention has been directed to QDs thanks to their exceptional electronic and optical properties for wide range of applications.[49],[68]

The first chemical route for the synthesis of semiconductor nanocrystal by using of non-ionic precursors in a high-boiling nonpolar coordinating solvent has been proposed by Bawendi and co-workers in the 1993.[58] They reported the synthesis of the best luminescent CdSe CQDs at that time with high degree of crystallinity and monodispersity. In the hot injection method reported by Bawendi et al., the nanocrystal precursors are heated up to solved in two different reaction baths, and rapidly injected one into the other once reached nucleation temperature. After the injection a high degree of local supersaturation occurs that brings to a fast nucleation. As the precursor is consumed the nucleation rate decrease. As consequence, the formed nucleus can grow into larger nanocrystals. The sequencing of nucleation and growth steps in the hot injection method is essential to obtain a QDs size dispersion lower than 10%.

The obtained QD-suspension were purified from excess of organic passivant and secondary products by precipitation/redispersion procedures. Finally, the QDs are redissolved in a solvent to form a stable colloidal suspension. This method still represents a base widely applied now days to produce many CQDs semiconductors. Thanks the high degree of tunability that the hot injection method enable over the

morphology of the nanocrystals, many studies have been dedicated to the CQD nucleation and growth mechanisms.[69],[70],[71]

3.2.1 CQDs Nucleation and Growth

The study of mechanisms underlying the CQD formation can be approached by the Classical Nucleation Theory (CNT) which describe the equilibriums underlying nanocrystals nucleation and growth in colloidal disperion.[72]

The initial formulation of the CNT dates back in 1927 by Volmer, Weber and Farkas,[73] with further modification by Becker and Döring in 1935,[74] and it has immediately been accepted from scientific society as a valid tool to describe the nucleation stage in phase transformations. The success of this theory probably relies on its simplicity and on the few parameters required to predict the nucleation rate.

Basically, we can describe the mechanism as follows: the reagents are injected into the solution pre-loaded inside the flask, their concentration increases until a certain level of supersaturation is reached causing a nucleation burst followed by an immediate decrease of the reagent concentration. The fast nucleation is then followed by a slower nanocrystal growth with the gradual consumption precursor species. As follows the reaction equilibrium is reported:

$$c\,Pb \cdot Oleate + c\,S \cdot Oleate \overset{\Delta G}{\leftrightarrow} (PbS)_c Oleate_n + (2c - n)\,Oleate \qquad 14$$

The $(PbS)_c Oleate_n$ clusters formed with the nucleation outburst have free energy that depends on their size. It is positive for small nuclei and increases with the size until a maximum value, then it starts to decrease. This free energy can be related to the NP radius *r* by:

$$\Delta G(n) = \Delta G_s + \Delta G_v = \frac{4}{3}\pi r^3 \Delta G^* + 4\pi r^2 \gamma \qquad 15$$

Where ΔG_v and ΔG_s are the volume and surface free energy respectively, r is the nucleus radius, γ is the surface energy per unit area and the ΔG^* is the free energy of the nucleus per unit volume. While ΔG_s is positive and linearly dependent on the r^2 of the nucleus, the ΔG_v is negative and is linearly dependent on the r^3 of the nucleus. Thus, as reported in the diagram in Figure 11 for cluster with size corresponding to a critical radius r_c there is a maximum in free energy $dG(n)/dr = 0$.

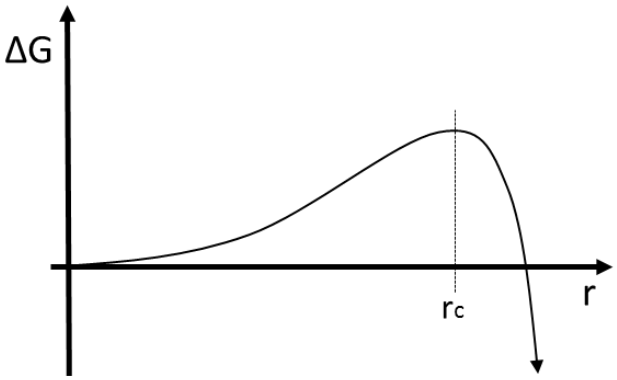

Figure 11: Diagram of NP free energy evolution with size in the nucleation regime.

For the nucleation of crystal nanoparticles with the hot-injection method the CNT theory can be just qualitatively applied to the formation of nuclei. Differently from what affirmed in eq. 17 the decrease in free energy per unit volume ΔG^* due to formation of the crystal structure and the surface free energy per unit of surface area γ are not constant. Indeed, ΔG^* varieties considerably with the size and structure of the forming nanocrystal, γ is strongly influenced from the arrangement of the surface atoms and the binding with the coordinating ligands.

So, it is better to report the equilibrium between the monomers and critical nuclei as equilibrium constant K_c with $n=c$, it will be:

$$K_c = \frac{[(PbS)_c]}{[Pb]^q[S]^c} \qquad 16$$

Now the critical nuclei consist of a well-defined number *c* of PbS molecules. The concentration of critical nuclei remains essentially zero, until the supersaturation regime is achieved, above which the concentration of the critical nuclei rapidly rises with the nucleation outburst.

The NPs nucleation outburst can be described the model proposed in the 1950 by LaMer and Dinegar[75] Figure 12

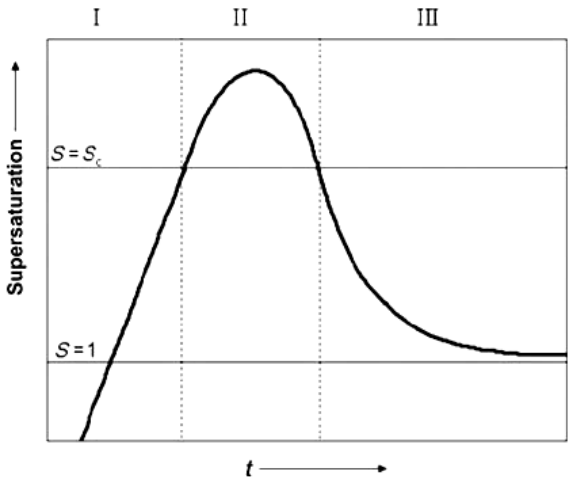

Figure 12: LaMer plot of the precursor concentration as a function of reaction time. (Reprinted with permission from V. K. LaMer and R. H. Dinegar, J. Am. Chem. Soc. 1950, 72, 4847–4854. Copyright 1950)

The continuous increase of reactive concentration with time reported Figure 12 even if efficiently represents the nucleation outburst, is a clear simplification of the hot injection case. In fact, in the hot injection method, the reagents are rapidly introduced in the reaction medium, with the immediate raise of precursor concentration above the nucleation threshold (t_i) that leads to a more discrete nucleation event Figure 13. The nucleation causes a fast decrease of the PbS precursors concentration followed that by the size-focusing growth of the NCs when the precursor species are more slowly consumed. Finally, the reaction is stopped before total precursors consumption (t_f).

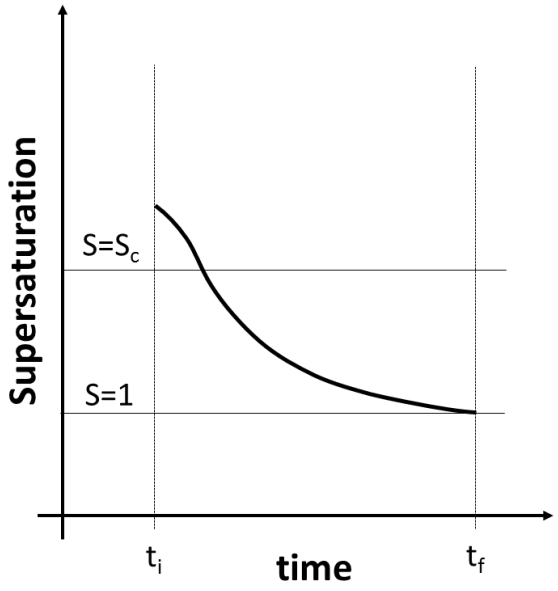

Figure 13: Hot Injection plot of the precursor concentration as a function of reaction time.

The concentration of reagents still available after nucleation is directly related to the degree of NCs size focusing. In fact, after the total consumption of the monomer precursors, the classical Ostwald ripening would take place causing the inhomogeneous shrink of the small nanocrystals to feed the growth of the bigger ones.[76] This mechanism is recognised as a major cause of QDs polidyspersity.[78] The stabilizing ligand and monomer reactivity are thus crucial in order to obtain discrete nucleation events and controlled growth[79]. In an ideal case, stopping the reaction before that Oswald ripening take place would permit that all nuclei created at the same time undergo identical growth. This is a defining principle on which the hot injection method relay for the achievement of a narrow size distribution of nanocrystals.[50]

3.3 Lead Sulphide

Among the different types of QDs materials, lead sulphide (PbS) colloidal QDs have attracted considerable attention for optoelectronic applications. Bulk PbS crystallize with rock-salt structure, possesses a bulk band gap energy of 0.41 eV and its exciton Bohr radius lies around 18 nm.[30] As consequence the decrease of the particle crystal size below the exciton Bohr radius, results in size-dependent optical properties of the PbS NCs. This reduction in size leads to a strong confinement of the charge carrier wavefunctions, giving rise to the quantized energy states and thus tuneable optical absorption and emission spectra.

The onset of the wavefunction confinement at relatively large NC diameters allows bandgap tuning over a large energy range (0.6-1.6 eV).[80] With a direct bandgap, PbS allows high molar absorption coefficient of 10^6 M^{-1} cm^{-1} at 400 nm.[81]

Due to the similar parabolicity of the PbS VB and CB at the L-point bandgap electrons and holes levels varying similarly as the NC sizes is changed.[30] In other words, the similarity between electron and hole wave functions in PbS QDs appear in its strong carrier confinement behaviour.

Size dependence of NCs optical properties has been correlated with eq. 17 proposed by Iwan Moreels et al.[82] that give the QDs size diameter from the spectral position of the first exciton absorption peak ($1S_h$ to $1S_e$ transition corresponding to the E_g in eV).

$$E_g = 0.41 + \frac{1}{0.0252d^2 + 0.283d} \qquad 17$$

Anyway, PbS QDs with diameters bigger than 10 nm typically result in higher size dispersions and poor optical properties. In that case is a better option a lower bulk band gap semiconductor like PbSe with exciton Bohr radius of 46 nm.[83]

3.3.1 PbS CQDs

In the present work we have approached and optimized the synthesis of lead sulphide CQDs by hot injection method with the objective to produce in a reproducible way high-quality solution processable QDs with a high size focusing to obtain a narrow photoluminescence peak in the third window of telecommunications.

3.3.2 PbS QDs Synthesis State-of-the-art

In recent years considerable effort has been dedicated to the development of reproducible syntheses of monodisperse lead sulphide nanocrystals.[84],[67],[85] Among them, during the last decade two chemical routes have shown to be the most promising and thus widely investigated.[50], [49] As it follows a brief overview of these two chemical route will be presented:

A. Hines and Scholes proposed in 2003 a synthetic route to the PbS CQDs using Lead oleate (PbO) and bis(trimethylsilyl)sulphide (TMS) as monomer precursor and oleic acid (OA) as coordinating solvent.[50]

With this synthetic route they have been able to produce PbS nanoparticles of tuneable size with sharp PL peak ranging from 1.2 to 1.6 μm, with FWHM of ~150nm.

B. Following a similar path Cademartiri et al. in 2005 reported the synthesis of PbS NCs with Lead Chloride ($PbCl_2$) and pristine sulphur (S) as monomer precursors and oleylamine (OAm) as coordinating solvent.[52]

The PbS nanoparticles obtained with this route have displayed high monodispersity in a wide range of sizes, they were tuned to produce sharp PL peak ranging from 1.2 to 1.6 μm, with FWHM of ~100nm.

This last one, proposed by Cademartiri et al., is the starting point that we have approached and optimized to produce air stable monodisperse PbS QDs with spherical shape and tuneable size in with absorption peaks covering the NIR spectral region.

3.3.3 Synthesis of colloidal PbS QDs

PbS QDs were synthesized by using a hot injection technique reported by Cademartiri et al.[52], which has been optimized in this work to produce air stable monodisperse PbS QDs with absorption peaks ranging from 1.2 to 1.6 μm, as aforementioned. We focused on the synthesis of large oleylamine-capped PbS nanocrystals around 6 – 7 nm in diameter. This synthesis uses lead chloride ($PbCl_2$) and elemental sulphur (S) as precursors and oleylamine (OAm) as coordinating solvent, which simultaneously acts as ligand and solvent. The reaction was carried out under inert atmosphere and relatively low temperature. A scheme of the reaction set-up is shown in Figure 14.

For a typical synthesis of 1550 nm PbS QDs the ratio of Pb : S is set to 3 : 1. Firstly, a stock solution of 0.05 g of S (1.5 mmol) in 5 mL of OAm is prepared by heating the mixture under N_2 at 125º C for 60 min. For the synthesis, 1.4 g of $PbCl_2$ (5 mmol) and 15 mL of OAm is mixed and degassed under N_2 in a three-neck flask at 125º C for 60 min. In this reaction, the solution of $PbCl_2$ and OAm results in a heterogeneous system and forms a turbid suspension. Afterwards, the solution is heated up to 140º C and the OAm-S precursor solution is swiftly injected into the reaction flask. The reaction time is set to 20 min to obtain the required QD size. Finally, the solution is slowly cooled to stop the reaction.

The size, morphology and composition of the QDs can be tuned by varying the synthetic parameters such as organic ligands, precursor concentrations, injection temperature as well as reaction time. In this synthetic route, the PbS QD size is easily tailored by the injection temperature (typically from 100 – 140 ºC) and reaction time. The increase of T and reaction time leads to the synthesis of larger PbS QDs.

Moreover, it is worth noting that the use of $PbCl_2$ as metal precursor may greatly enhance the QD stability in suspension since Cl^- has been demonstrated to passivate QD trap states and effectively prevents surface oxidation over time in solution, as confirmed by our XPS results (see Chapter 4) and previous studies.[52]

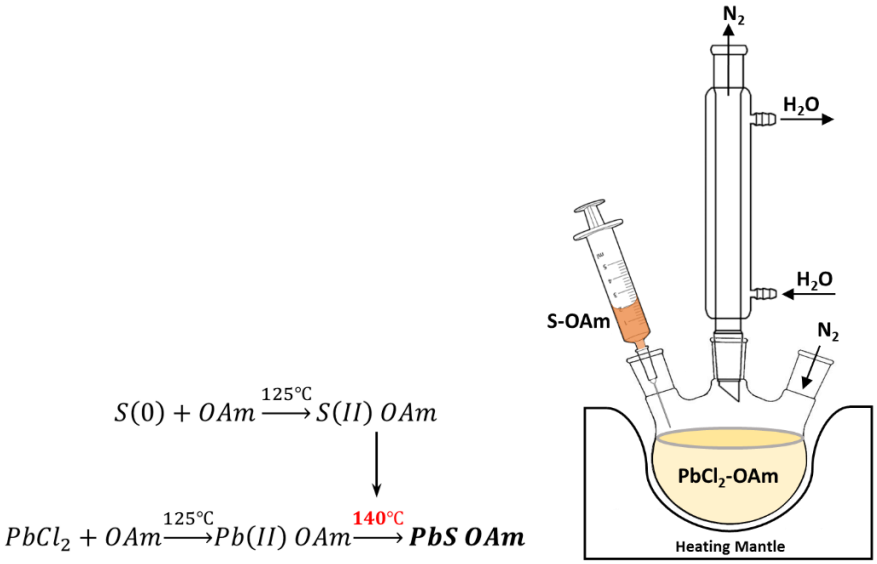

Figure 14: (Left) Synthetic route of 1550 nm PbS CQDs; (Right) Scheme of the hot-injection setup.

3.3.4 Purification and Solvent Exchange

After the synthesis, a solvent exchange procedure is carried out to remove excess of unreacted precursors and OAm and to prepare PbS QD solution at a desired concentration.[86] This step is very important and has to be done carefully because QD film quality dramatically depends on the purity of the resulting QD solution. For such a reason, once the reaction finishes, the solution is centrifuged. Then, the QDs are re-dispersed in 15 mL of toluene and a polar solvent like methanol is added to precipitate them. The mixture was centrifuged again and the supernatant decanted. This process was repeated twice.[87] It is worth noting that the PbS QDs cannot be precipitated and redispersed more than twice due to a loss of oleylamine ligands and subsequent QDs aggregation. Finally, the QDs are dispersed in octane under N_2 in a sealed vial at a concentration of 150 mg/mL.

3.4 Characterization of colloidal PbS QDs

The characterization of the synthesized PbS CQDs has been firstly carried out by photoluminescence (PL) measurements. In Figure 15a, it is reported the PL spectra of PbS CQDs solutions obtained at different reaction times. As observed, the PL peak shifts towards longer wavelengths with increasing the synthesis reaction time, corresponding to a QD size of 3.1 – 6.5 nm. Furthermore, the full width at half maximum (FWHM) of the PL, which directly relates with the QD size distribution, decreases at larger wavelength indicating an enhancement of the size focusing for larger nanocrystals. However, for reaction times longer than 20 min, the size dispersion drastically increases the synthesis must then be based on a ripening mechanism, either Ostwald ripening or involving the coalescence of smaller QDs.[52]

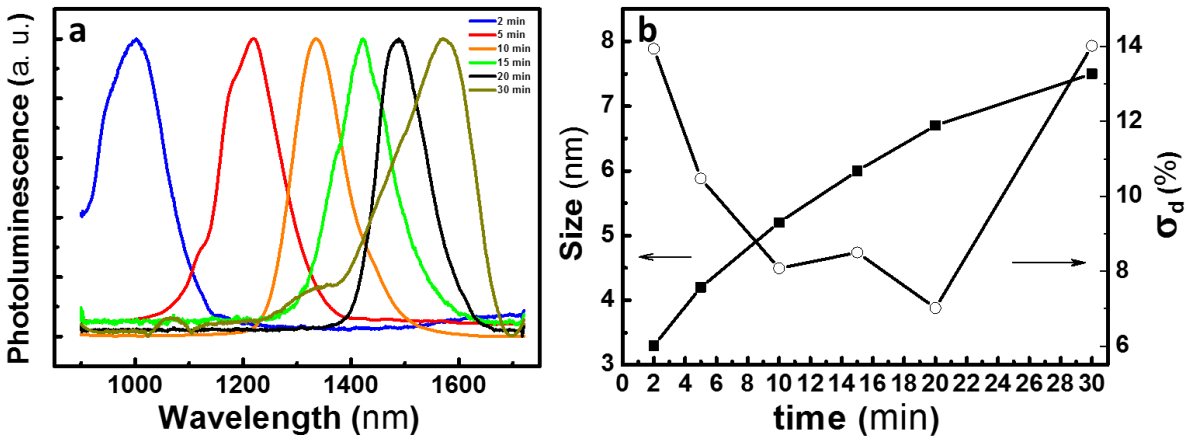

Figure 15: **a)** Series of PL spectra for PbS QDs synthesized with different growth time; **b)** PbS nanocrystals size and relative size dispersion as a function of growth time.

The trend reported in Figure 15b, calculated from the QD sizes with eq. 17, shows the dependence of the QDs size and size dispersion with respect to the reaction time. Here it shown, the improvement of the QD size dispersion with growth time with σ_d decreasing until 20 min of reaction time, thereafter the ripping mechanism starts and σ_d drastically increases. As reported in Table 1, for QDs with average diameter of 3.1 nm the size dispersion is σ_d = 13.9 %, and decreases to σ_d ~ 7.0 % for QDs with diameter ~ 6.7 nm.

Table 1: Reaction time and outcomes in PL peak position and FWHM with the related PbS NCs size and σ_d.

Reaction Time (s)	**PL λ (nm)**	**PL FWHM (nm)**	**d (nm)**	**σ_d (%)**
2	1000	139	3.1	13.9
5	1220	126	4.2	10.4
10	1335	109	5.2	8.0
15	1420	121	6.0	8.5
20	1500	105	6.7	7.0
30	1577	221	7.5	14.0

As aforementioned, we have investigated and properly optimized this synthetic route to produce large PbS QDs emitting at around 1550 nm. Figure 16 shows the optical properties of 7 nm PbS QDs, which exhibit a well-defined excitonic peak in absorption centred at 1500 nm with a full width at half- maximum (FWHM) of 140 nm, whereas the corresponding photoluminescence (PL) band is located at 1550 nm with a FWHM of 130 nm.

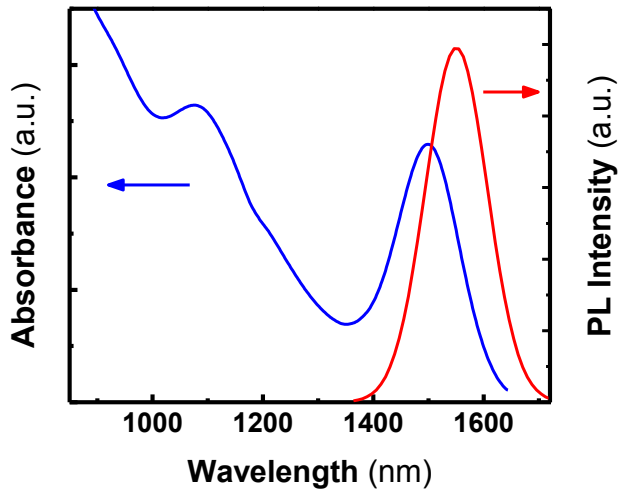

Figure 16: Absorbance (blue line) and photoluminescence (red line) spectra of the PbS QDs with diameter ~7 nm in octane.

The average size of the PbS QDs was extracted from TEM images. In Figure 17a is reported the TEM image of the spherical PbS QDs with average size of 6.8 nm and relative size dispersion σ_d = 8.3 % (histogram in Figure 17b). This size is in good agreement with the one calculated with eq. 17.

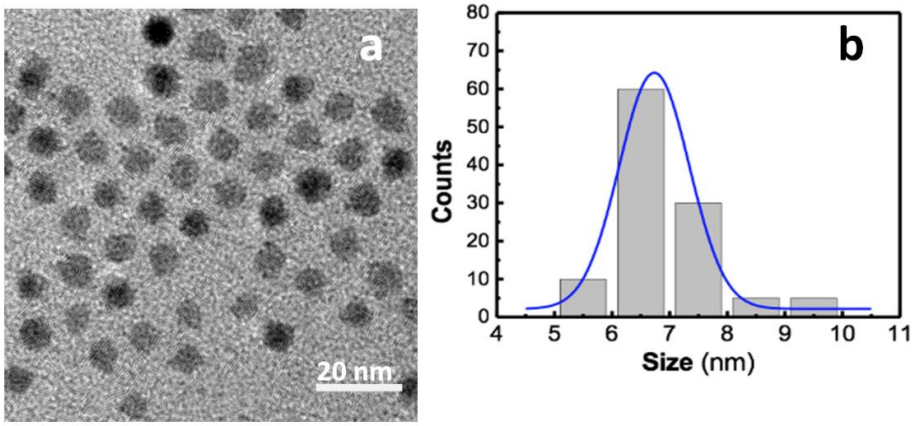

Figure 17: **a)** TEM image of spherical PbS QDs. **b)** Size histogram of the colloidal PbS QDs. The mean size equals 6.7 nm, with a size dispersion of 8.5 %.

In Figure 18a is reported a high-resolution transmission electron microscopy (HRTEM) image of the PbS QD evidencing the high level of crystallinity and low concentration of stacking faults and lattice

defects. The selected area electron diffraction (SAED) pattern (Figure 18b) is consistent with the rock salt structure of bulk PbS. Furthermore, the lattice d-spacing of the PbS nanocrystal shown in Figure 18b is estimated to be 0.30 nm, which is in good agreement with the {200} lattice plane for bulk PbS (JCPDS Card No 02-0699).

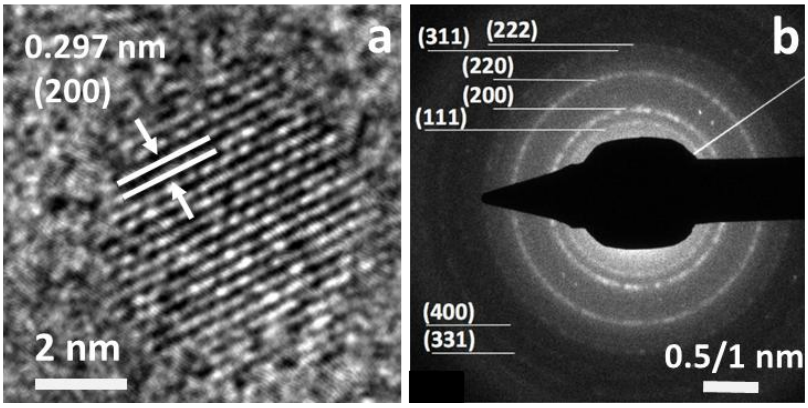

Figure 18: **a)** HRTEM image of a PbS QD showing crystallinity and absence of lattice defects. **b)** HRTEM-SAED image showing a diffraction of crystal planes consistent with PbS bulk lattice parameters.

The composition of the QD core and its Pb/S ratio were analysed by energy-dispersive X-ray spectroscopy (EDX) (Figure 19). Pb and S are observed in the pattern (carbon and copper signals come from the carbon-coated copper grids), with a Pb:S ratio 55:45.

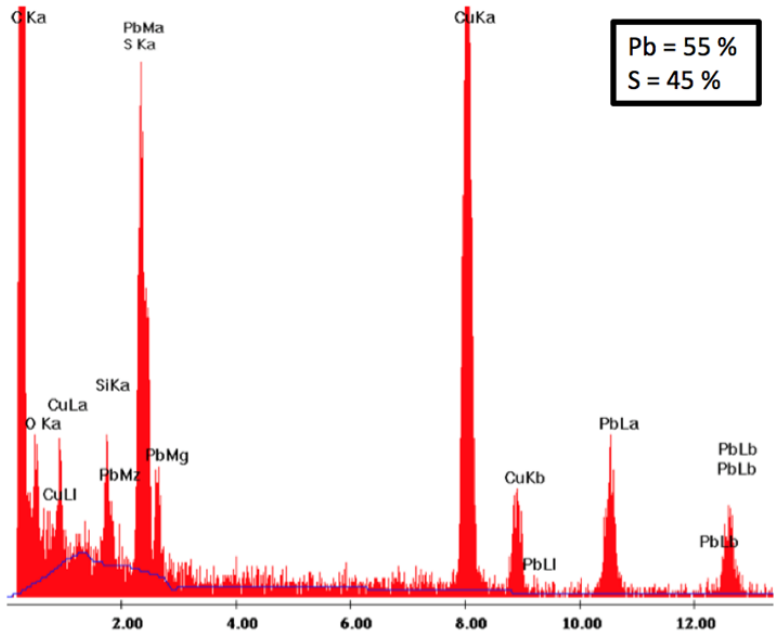

Figure 19: EDX analysis of OAm-PbS QDs.

We have also investigated the efficiency of the QDs passivation by OAm. In Figure 20 is reported the comparison of the emission spectrum of a freshly prepared PbS QD solution before and after two months. Only a small shift could be noticed as a proof of stability of the colloidal dispersion.

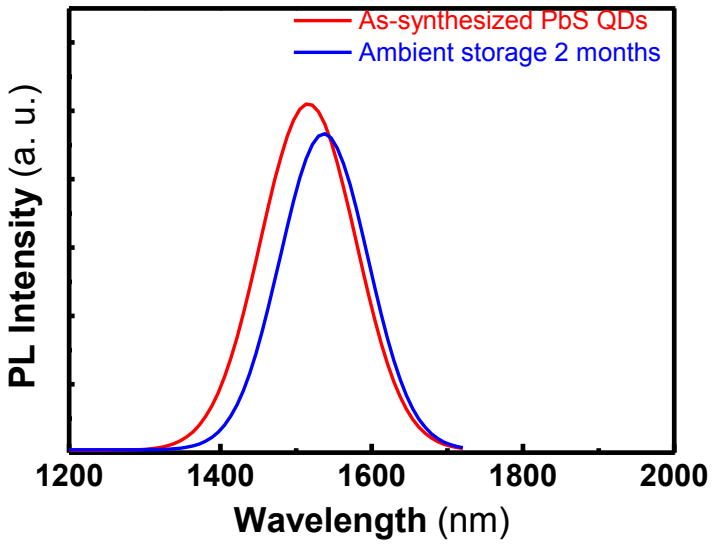

Figure 20: Photoluminescence spectra of a freshly prepared PbS QD solution before and after two months.

Chapter 4 PbS QD-solid

Great part of the attention captured by CQDs as a candidate material for optoelectronic applications arises from their solution processability. It facilitates ready integration in an almost limitless variety of substrates, including post-processing atop other integrated circuits. Indeed, so far light-emitting diodes,[88],[89] lasers,[90] optical modulators,[91] solar cells,[92],[93] photodetectors,[94] have all been reported. Thanks to their solution processability, CQDs represent a suitable path for to enable the development of highly scalable manufacturing processes.[6],[95]

This chapter begins with a review of the most diffused solution processing technique for NPs dispersions. Many of these techniques have been approached for the fabrication of high quality QD-solids.[24] We analyse with most details the doctor blading technique as it resulted to be the most promising for our purposes.

The chapter also describe the steps we overtook for the formulation of a nanoink for the produced PbS CQD dispersion. This step has the objective to optimize the rheological properties of the PbS dispersion to better suit the doctor blading deposition technique. The chapter ends with the production of PbS QD-solids by doctor blading method and their characterization.

4.1 CQD Deposition Techniques

In this section, we will introduce and describe an array of methods used to produce thin films from colloidal solutions. A brief overview of the most important methods to produce QD thin films is presented. In our case, colloidal dispersions facilitate the processing of QDs by techniques such as drop casting, dip coating, spin coating and doctor blading. These deposition methods, differently to conventional vacuum-based techniques, have the main advantages of being low cost, simple and scalable.

4.1.1 Drop Casting

It consists on dropping a small volume of the solution carrying the material to deposit on a substrate and let the solvent evaporate spontaneously. After drying, the sample is thermally beaked to improve the layer adhesion to the substrate.

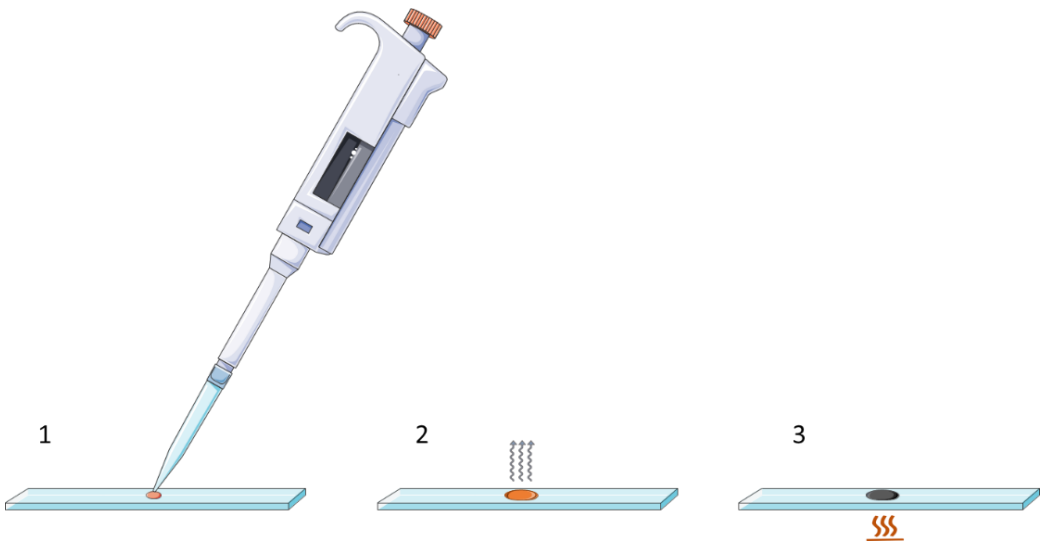

Figure 21: Schematic illustration of the drop casting fabrication technique in three steps: 1) dropping; 2) spontaneous evaporation; 3) thermal baking.

The film thickness depends directly on the particle concentration and on the deposited volume. Other significant variables with deep influence on the film morphology are: the vapor pressure of the solvent, its surface tension and the capillary forces associated with the drying process.[96]

This method give the best results with volatile solvents since a fast drying process the decrease the probability of thin film defects issues.[83] Organic solvents (such as hexane, toluene or halogenated solvents) are often very good choices for nanoparticles with hydrophobic capping ligands.[97]

Drop casting is a quick and accessible method suitable for small substrates, involving practically no material waste and can be carried out at standard temperature and pressure. The drawbacks of drop casting are associated to its strong dependence to the solvent properties, the differences of the evaporation rates across the substrate or QDs concentration fluctuations can lead to inconsistencies of the thickness of the film and structural defects.[97] This technique is widely applied for deposition of thin films (100 nm thick) over really small areas (less than 1 mm^2).[24]

4.1.2 Spin Coating

The spin coating thecnique generally involves the application of a small volume of solution (from hundreds of µm to few ml) on a substrate. The material to deposit forms a coating on the substrate while the solvent is slowly flung off as the rotation starts.

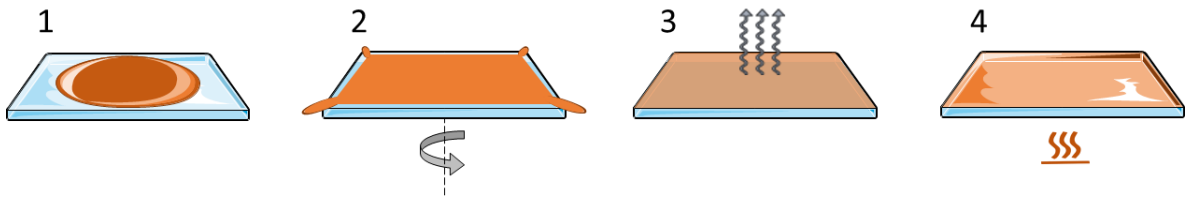

Figure 22: Schematic illustration of the spin coating deposition technique.

We can separate the deposition steps of spin coating method as follow:

1. First the substrate is coated in the ink containing the material to deposit.
2. Then the substrate is rotated at high speed and must of the ink is flung off the side.
3. Airflow then dries most of the solvent leaving a film.
4. The substrate backed in a hot plate to make the film adhere to the substrate so that the deposition procedure can be eventually repeated to increase the thickness.

The rotation of the substrate at high speed (usually from around 3000 rpm)[98] means that the centripetal force spread the dispersion generating a thin wet film. The solvent then evaporates to leave the solid on the substrate. The applied solvent is usually volatile, and evaporates simultaneously with the spinning. Consequently, to achieve thin films is necessary high the angular speed of spinning.

The thickness of the film also depends on the viscosity and concentration of the solution, the viscosity of solvent and ambient conditions. The influence of all the parameter over the final thickness of the film cab be described with eq. 18 :[99]

$$h = \left(1 - \frac{\rho_A}{\rho_{A0}}\right) \cdot \left(\frac{3\eta \cdot m}{2\rho_{A0}\omega^2}\right)^{(1/3)} \qquad 18$$

Where h is the film thickness, ρ_A is the density of the solution, η its viscosity, m the evaporation rate, and ω the angular speed.

By this technique is possible to achieve film with thickness from few nm up to around 200 nm with low viscosity solutions (less than 2 cP).[100]

The spin coating has the advantage to be a user friendly and low cost method that can be performed at standard temperature and pressure creating extremely thin films (10 nm or less).[101] Its limits are definable in the strict dependence to the solvent of the ink,[97] the limited substrate size (few cm^2) and geometry.[12] In fact, only substrates of small areas with high symmetry are apt to be coated with this method. Another downside of this technique is a typical coffee ring and striations effects consistent in oriented lines of thickness variation in the as-coated film that compromise the homogeneity of the coating over the entire surface.[101]

4.1.3 Dip Coating

By the dip coating approach, the substrate is dipped into the solution and then vertically withdrawn at a controlled speed. Consequently, a wet film adheres to the substrate, which results in a solid layer upon drying.

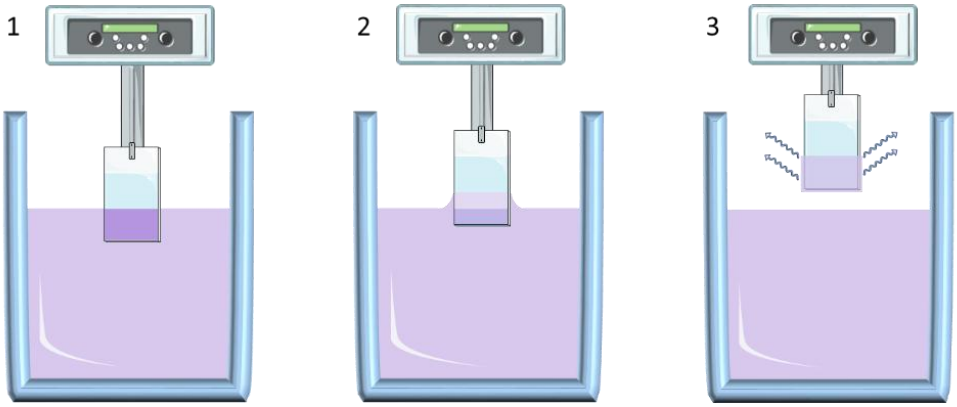

Figure 23: Schematic illustration the dip coating deposition technique.

The dip coating process can be separated into three fundamental steps (as reported in Figure 23):

1. Dipping: The substrate is immersed in the solution of the coating material at a constant speed (preferably jitter-free).
2. Deposition: a thin layer of the solution adheres on the substrate while it is pulled up. The withdrawing is carried out at a constant speed to avoid any jitters.
3. Evaporation: The solvent evaporates resulting in the production of a thin film of the solid on the substrate surfaces.

Taking into account the balance of forces at the liquid-substrate interface is possible estimate the final coating thickness using the Landau and Levich Equation:[99]

$$H = \frac{0.94(\mu V)^{2/3}}{\gamma^{1/6}(\rho g)^{1/2}} \qquad 19$$

here μ is the fluid viscosity, v the withdrawal speed, ρ the fluid density, g the gravitational acceleration and γ the surface tension between the liquid and the air.

This is a method industrially employed to apply protective, decorative, or functional coatings on a variety of rigid substrate, flexible sheet or filament.[102] For research activity it is largely used to produce thin films from sol-gel precursors where has enabled the fabrication of extremely homogeneous thin films of around 2 nm thick over large areas.[103]

The disadvantages of this technique reside on its high material consumption, the long processing time necessary to provide homogenous film deposition avoiding gradient effects and the double side coverage that in many cases is not desired.

4.1.4 Blade Coating

The doctor blading concept finds its origin on the metering blade that have the function of remove the inks excess from non-engraved portions of the image carrier, as for example rotogravure printing units.[104] Most recently, the doctor blading for industrial application is one of the most efficiencies techniques for producing thin films on large area surfaces. It is a relatively new process which was originally developed during the second half of the 40's in the first recorded tape-casting machines which were patented by Glen Howatt, as a method of forming thin sheets of piezoelectric materials and capacitors[105]. One patent, issued in 1952, focuses on the use of aqueous and non-aqueous slurries applied to moving plaster batts by a doctor blading device where a well-mixed slurry consisting of a suspension of ceramic particles along with other additives (such as binders, dispersants or plasticizers) is placed between the substrate and the blade.[106] Here when a constant movement is established between the blade and the substrate, the colloidal dispersion spreads on the substrate to form a thin sheet which results in a solid layer upon drying.

Then, the patent deposited from Glen Howatt has been the represent the origin for the doctor blading and tape casting methods known recently known for playing an important role in solution processing as in optical films, medical films used as drug delivery systems, microporous membranes and ceramic body armour.

It is reasonable to say that the technique take its name from the blades used in flatbed letterpress equipment, where blades were used to wipe the ductor rolls, and it is from here that "ductor" became doctor.[107]

Most recently this deposition technique has found application in the manufacturing of printed bulk heterojunction solar cells and QD-sensitized organic infrared photodiodes, whose performances are similar to those processed by spin coating.[108],[99] It has been also applied for the production of large-area ordered magnetic nanocrystal thin films, resulting in a degree of ordering that outperforms those provided by

alternative deposition techniques such as inkjet printing or drop casting.[109] Nevertheless, to the best of our knowledge, this technique has not been applied to form solution-processable QD-solids so far.

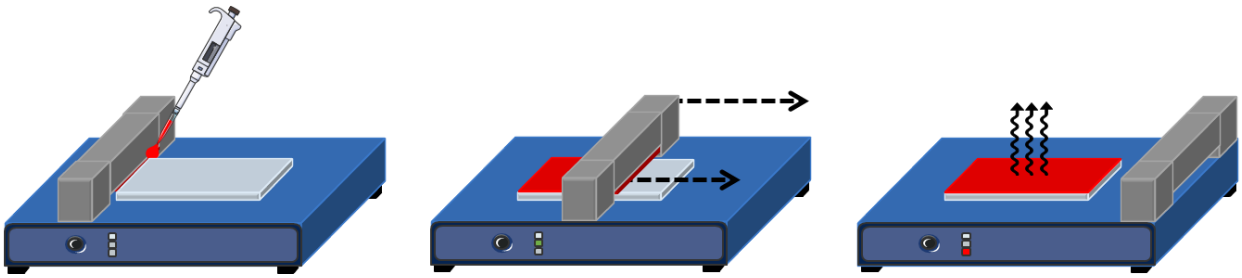

Figure 24: Schematic illustration of the doctor blading deposition technique.

Doctor blading (depicted in in Figure 24) basically is equipped with a coating knife that, mechanically activated, spread the ink uniformly over the substrate. The necessary amount of the solution is applied either directly onto the substrate or, in case of low viscosity solvents is poured in the gap between the substrate and the blade. Then the blade uniformly moves forward spreading the solution along the substrate leaving a wet thin film behind. Most of the solvent rapidly evaporates and the film obtained is then beaked in hot plate to dry and optimize the adhesion onto the substrate. Subsequently, other layers can be deposited following the same procedure without damaging the underlying layers.

Doctor blading is a scalable, simple, low-cost and low temperature solution-based thin film deposition technique that is compatible with roll-to-roll fabrication of large area devices with a high throughput.[24]

4.2 Nanoink Formulation

The PbS CQDs synthesizes as described in the previous chapter have to be now converted into a QD-ink with the rheological properties optimized selected deposition technique, in our case to the doctor blading coating technique.[110],[103] At first we decided to take under study the surface tension of the nanoink as it is related to the wetting properties over the substrate, the homogeneity of deposition and it can be also tune to minimize the "coffee ring effect".[97],[100]

We found the optimum formulation of the QD nanoink with a NCs concentration of 150 mg mL^{-1}. The QDs were dispersed in octane. The obtained colloidal solution exhibits a surface tension of 36 dyn cm^{-1} and a contact angle on the PEDOT layer of around 7° and 6° on silicon-SiO_2 substrates. The selection of octane as solvent is also due its volatility (octane vapor pressure 1.47 kPa at 20.0 °C), lower than the toluene one (toluene vapor pressure 2.8 kPa at 20°C)[96] which allows the wet film processed by doctor blading to slowly dry leading to an optimal self-assembly of QDs into a close-packed superlattice for the QDs on the equilibrium "super-lattice" sites, leading to an optimal self-assembly of QDs into a close-packed superlattice.

4.3 PbS QD-solids fabrication by doctor blading

For the fabrication of QD-solids by doctor blading approach we have considered several parameters to obtain a homogeneous film with the desired thickness. To produce QD-solids for Schottky devices, the distance between the blade and the substrate has been fixed at 2 mm then 10 µL of the nanoink has been injected and spread at 1.5 cm s^{-1} over a 10 cm^2 area to create a first thin (30 nm) coat of QDs. This first deposition has the function of create a smooth ground prone for following faster spreading of 6 cms^{-1} accountable for greater contribution (80 nm each) to the ultimate solid thickness of ≈350 nm. Backing treatments of 5 min at 100°C has been performed after every deposition and ultimately a thermal cure under vacuum for 90 min at 100°C. In Figure 25 is reported a picture of the as produced QD-solid over a glass substrate.

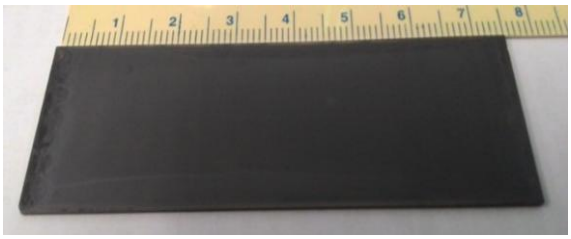

Figure 25: Picture of a QD-solid produced by doctor blading on a 7.5 x 2.5 cm2 glass substrate.

For the production of QD-solids for microgap photoconductor devices, due to the smaller deposition surface, the distance between coating blade and the substrate has been fixed at 1 mm for the injection of 4 µL of PbS nanoink followed by spreading at 1.5 cm s^{-1} over the electrodes gap to create a first thin (30 nm) coating of QDs. This first deposition has the function to create a buffer layer followed by faster spreading at 6 cm s^{-1} to obtain thicker QD layers, of ~90 nm each, until the desired thickness is achieved. A baking process of 5 min at 100 °C is performed after every deposition, whereas a thermal curing process is carried out at 100 °C for 90 min under vacuum conditions. In Figure 7 is reported a picture of the as produced PbS QD-solid onto silicon-SiO_2 substrates with gold electrodes.

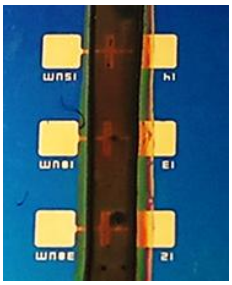

Figure 26: Picture of a QD-solid produced by doctor blading on a onto silicon-SiO2 substrates with gold electrodes.

With a slower drying process of the film deposited by doctor blading the NCs can easily self-assemble into a close-packed “super-lattice” as observed in the TEM images in Figure 27a. The SEM images of the QD-solid surface (in Figure 27b) and cross-section (in Figure 28) evidence that the removal of OAm ligands by solid state ligand exchange (described in section 4.4) does not cause significant morphological defects such as cracking or pinholes within the film.

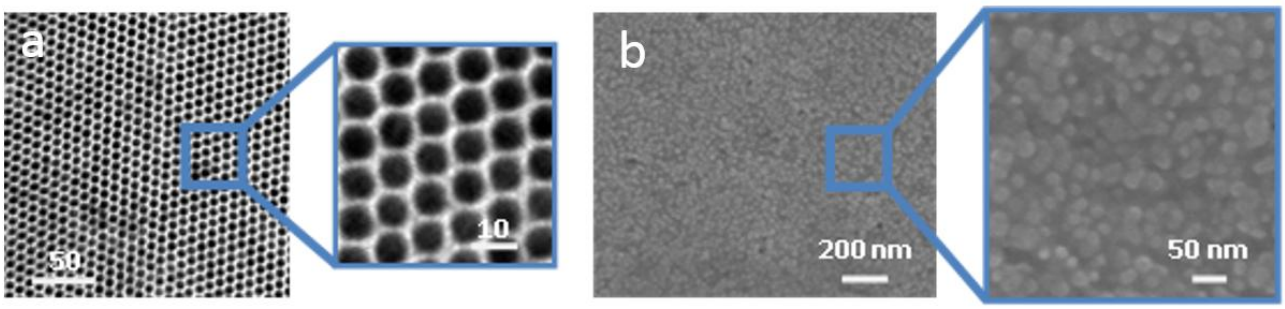

Figure 27: (a) TEM images of a self-assembled monolayer of OAm-capped PbS QDs. (b) SEM images of the PbS QD-solid surface.

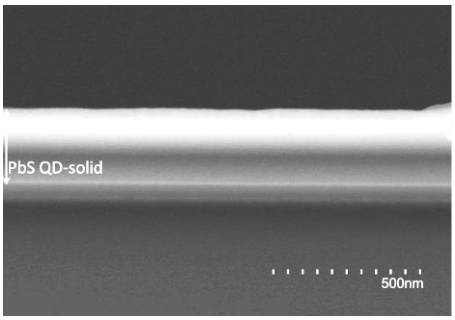

Figure 28. Cross sectional scanning electron microscopy (SEM) images of the PbS QD-solid deposited on a SiO_2 substrate by the doctor blading method.

4.4 Ligand Exchange Strategy

In QD-solids the capping ligand of the QDs has a direct impact on the film conductivity since the charge transport among nanocrystals occurs mainly by ligand-assisted hopping.[30],[60] High charge carrier mobility can, thus, be achieved by decrease of the inter-nanoparticle spacing [15]. The as synthesized OAm-capped QDs yield to films with insulating properties since OAm is a long ligand of eighteen-carbon-atom chain (~3.6 nm). That hinhibits carrier transport among the nanocrystals.[86] To improve the film conductivity we carry out a solid-state ligand exchange strategy that by replacing the long OAm ligand with a shorter one that still providing a good passivation to the QD surface improve the carrier mobility. Different ligand exchange strategies have been reported for lead chalcogenides QDs, among them bidentate thiols,[111] primary amines,[51] carboxylic acids,[112] thiocyanate ions,[60] and halide ions[113] have attracted the most interest.

Among them we have used the 3-mercaptopropionic acid (MPA) and tetrabutylammonium iodide (TBAI).

MPA is a short (0.68 nm) bidentate ligand that allows an efficient electron coupling among neighbouring QDs without drawback in the quantum confinement.[114],[115] The OAm is efficiently replaced by the MPA due to the high affinity of the thiol group to the lead ions on the QD surfaces, in agreement with the HSAB theory.[116] Furthermore, MPA which also present a carboxylate functional group, provides a high passivation action over a broad distribution of PbS surface states.

Studying the TEM images in

Figure 29 with an image analysis software, we estimate that the average centre-to-centre distance among nanocrystals gets from 9.0 ± 0.7 nm before the ligand exchange to 7.4 ± 0.5 nm after the MPA passivation. The interparticle spacing then reduced from 2.3-2.4 nm to 0.7-1.1 nm with the MPA ligand exchange.

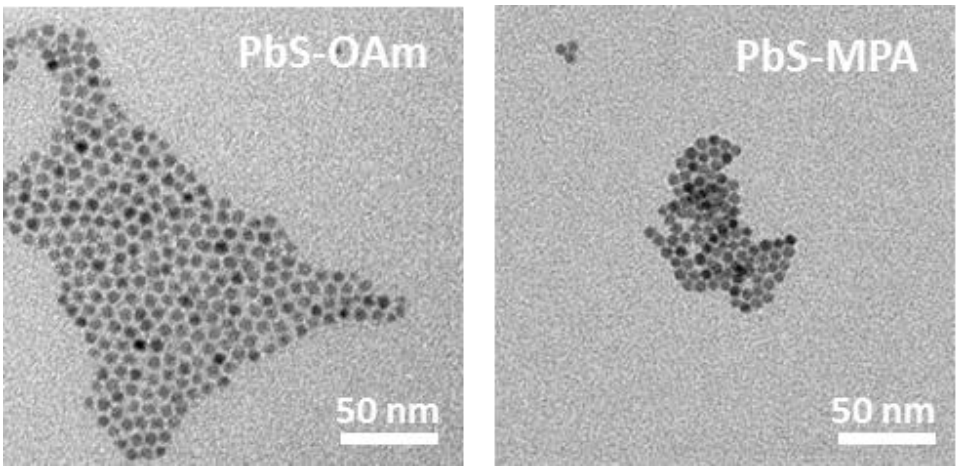

Figure 29: TEM images of PbS QDs before (left) and after the ligand exchange process (right). Image analysis of the images reveals an interparticle separation of OAm-capped PbS QDs (6.7 nm in diameter) of 2.3 nm, which is significantly reduced up to 0.7 nm after the ligand exchange.

The iodine-containing TBAI, has been then approached aiming to further enhance the QD-coupling introducing I^- ions as passivating agent that bind to Pb^{2+} dangling bonds at the PbS surface.[117] Additionally, the formation of PbI_2 at the surface with I^- : Pb^{2+} ratio 1 : 1 can result in the formation of a PbI_2 shell-like structure to the PbS core, which can be considered as a tune up of the passivating action provided by Cl^- ions resulting from the reaction precursor.[118]

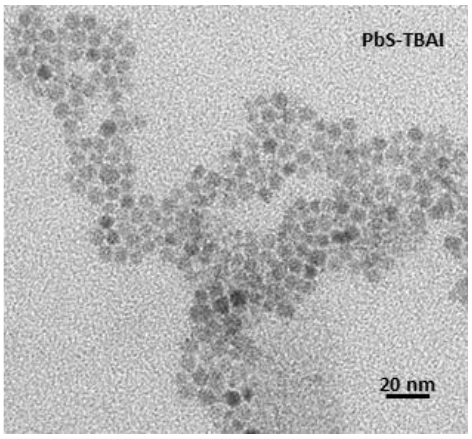

Figure 30: TEM images of PbS QDs after the ligand exchange process with TBAI. Image analysis of the images reveals an interparticle separation among QDs dramatically decreased and presence of particles agglomeration.

4.4.1 Ligand Exchange Experimental Procedure

The solid-state ligand exchange with MPA has been carried out dipping the OAm-capped PbS QD film in a solution of MPA in methanol (10 %) for 60 seconds, rinse with MeOH and dried under a N_2 stream then thermally cured under vacuum for 90 min at 100°C. The resistivity of the QD-solid after ligand exchange decreases of approximately five orders of magnitude ($\rho \approx 10^5$ Ωcm, as measured using ohmic contacts on a 500 nm thick QD-solid deposited on glass).

The same process has been carried out for the solid-state ligand exchange with TBAI. In this case the resistivity of the QD-solid decrease of about six orders of magnitude, measured under the same condition of the MPA threaded sample.

4.5 QD-solid Characterization

The produced PbS QD-solids have been structurally characterized by Grazing incidence X-ray diffraction (GIXD). In Figure 31a is reported the GIXD patterns of a 400 nm thick PbS film deposited on glass by doctor blading and cured at 100 ºC for 10 min. The diffraction peaks at 2θ = 25.8º, 29.9º, 42.9º, 50.9º, 53.3º, 62.5º, 68.8º, 70.8º, and 78.9º are well matched with (111), (200), (220), (311), (222), (400), (331), (420) and (422) crystalline planes of cubic phase (galena) of PbS (JCPDS Card No 02-0699). Furthermore, the absence of significant peaks at 22.9 º, 35.8 º, and 46.5 º in both GIXD and XRD patterns (Figure 31b) prove that no trace of $PbCl_2$ lasted after synthesis purification. We determined the lattice constant of 0.5957 nm, comparable to the standard value of 0.5936 nm for bulk PbS. Moreover, the average diameter of the QDs in the thin film was estimated to be ≈ 6.7 nm, i.e., similar to the value extracted from TEM images, as deduced from the Debye-Scherrer formula[85] applied to the linewidth of the (200) in GIXD and XRD patterns in Figure 31a and Figure 31b.

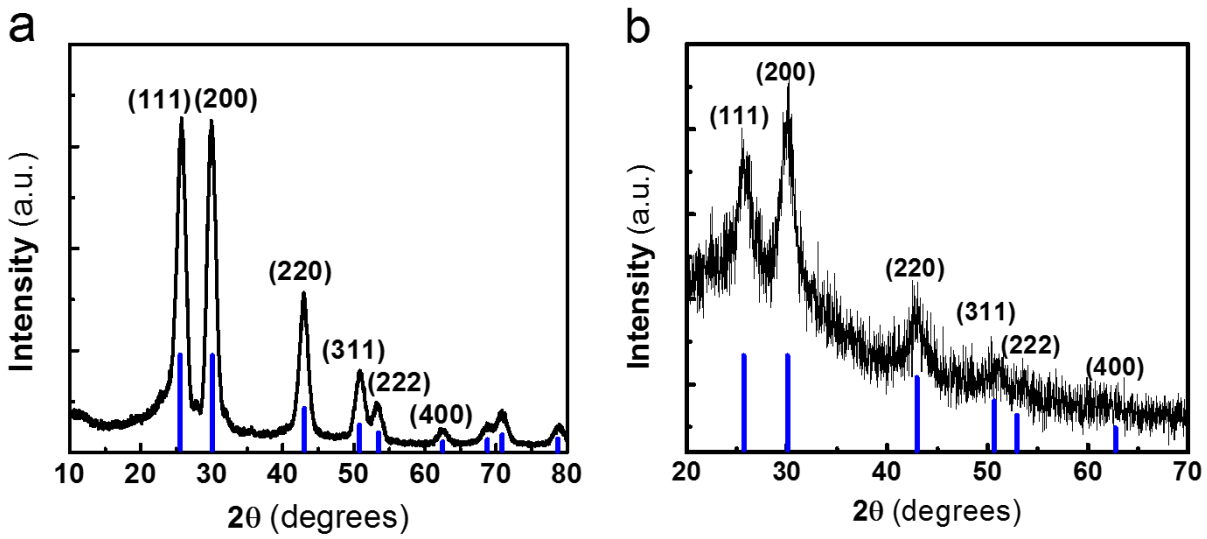

Figure 31: a) GIXD pattern of OAm-capped PbS QD film deposited by doctor blading. b) X-Ray Diffraction pattern of PbS QDs.

To investigate the outcome of ligand exchange treatment we have carried out Fourier Transform Infrared Spectroscopy (FTIR) measurements.

The effective exchange of OAm by MPA in QD films is evident by the loss of the C=C stretching vibration peak at 3005 cm^{-1} and the strong intensity decrease of the aliphatic C–H stretching peaks at 2845–2915 cm^{-1}, as observed in Figure 32a. Moreover, the symmetric and asymmetric stretching vibrations of the carboxylate group of MPA appear at 1380 and 1510 cm^{-1}, respectively, and the N–H bending vibration at 1550 cm^{-1} is not observed after the ligand exchange. The absence of S–H bond stretching vibration modes in the region 2500–2600 cm^{-1} suggests that any excess of free MPA has been completely removed after washing with methanol.

The binding of MPA to PbS is accomplished through chemical bonding between thiols and free coordination sites on Pb(II) atoms. The characteristic broad band at 3300 cm^{-1} from hydrogen bonds between $–NH_2$ groups of free adjacent OAm molecules observed for the OAm-capped PbS is no longer observed in the MPA-treated PbS QD film.

The ligand exchange process was also analysed by thermogravimetric analysis (TGA) from room temperature to 300°C under O_2 (Figure 32b). At temperature ranging from 25°C to 50°C both samples have a gradual decrease in mass, which is attributed to the loss of residual solvent and water adsorbed on the surface of the films. The weight loss for the MPA treated QDs at 100–115°C is attributable to the MPA ligand itself as it has the boiling point at 110–115°C. This mass reduction does not appear for the untreated PbS QDs, hence providing further evidence of the complete ligand exchange from OAm to MPA ligands. The continuous mass reduction from 150°C is only observed in the OAm-capped QDs, which is due to the progressive burnt off of the alkyl chains.

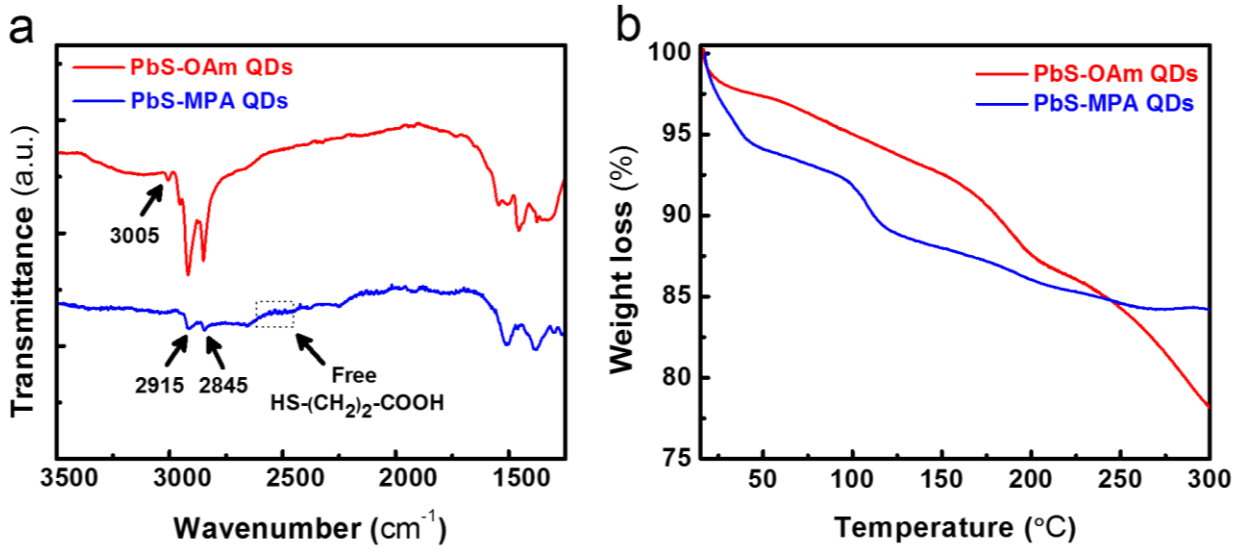

Figure 32: a) FT-IR spectra of OAm-capped PbS and MPA-capped PbS QD thin films. b) TGA of the OAm-capped PbS QDs and after treatment with MPA.

The self-organization of the PbS QDs into close-packed BCC superlattice structure showed in Figure 27a related at the OAm passivated PbS NCs is fundamental to be maintained also after MPA ligand exchange, this is an essential requisite to make of the slid state ligand exchange a viable experimental route. To do so we can use low angle X-ray diffraction pattern of the OAm-capped and the MPA-capped PbS QD-solid films prepared by doctor blading in Figure 33 to verify that no modification take place in QDs ordering. Low-angle X-ray diffraction pattern provides diffraction patterns associated to the superlattice formed by self-organization of the QDs during deposition onto the substrate. In the sample with MPA-capped PbS QDs three main diffracting planes are observed at 2θ≈1.38, 2.37 and 3.43º. The corresponding superlattice planes would respectively be (110), (211) and (222) to attribute to a body-centred cubic (BCC) Bravais lattice. The lattice constant of the non-primitive cubic unit cell turns to be a = 9.05 nm, from which we obtain a diameter of 7.8 nm for solid spheres (D) forming the lattice, which is consistent with the sum of the QD diameter plus the MPA ligand length. In the case of the OAm-capped PbS QDs, given that we only observe two diffraction angles (greater than 1º) at 2θ ≈ 2.05 and 3.19 º, we assume that QD-ligand units self-organize into a BCC structure and hence these angles would correspond to diffracting planes (211) and (222) respectively. From this assignation we can attribute a lattice constant a ≈ 10.5 nm and hence D = 9.1 nm, which is consistent with the higher length of OAm ligands as compared to MPA ones.

The values obtained for the diameter of the QDs before and after the ligand exchange are also consistent with the results of the TEM analysis reported in Figure 29 where the interparticle separation of OAm-capped PbS QDs is of 2.3-2.4 nm and shortened to 0.7-1.1 nm after the ligand exchange.

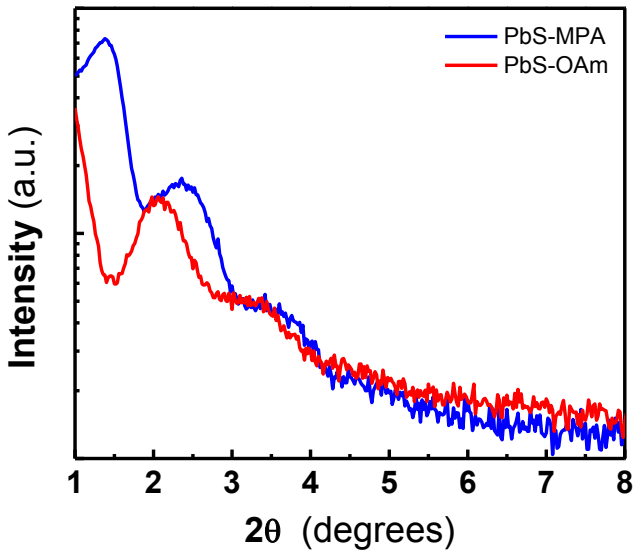

Figure 33: Low-angle X-Ray diffraction pattern of OAm-capped (red line) MPA-capped (blue line) PbS QD-solid films deposited by doctor blading.

Another evidence of the large scale order conservation after solid-state ligand exchange is given by the GIDX pattern of MPA-capped PbS QD film Figure 34, where we can observe that there is not evident change with respect to the pattern of the OAm-capped PbS QDs Figure 31a.

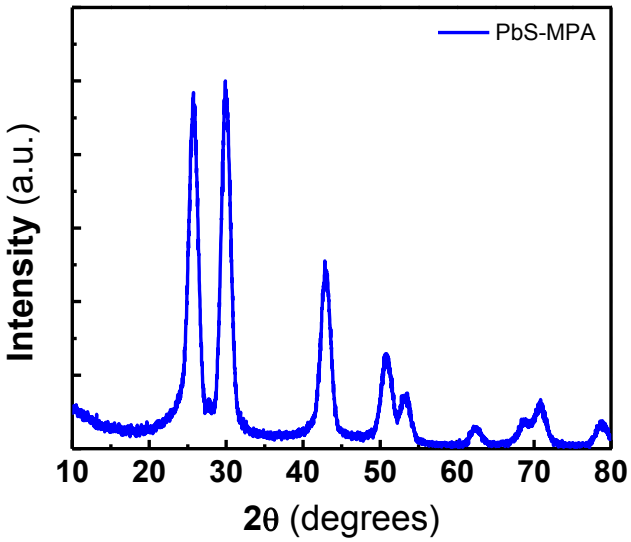

Figure 34: GIXD pattern the MPA-capped PbS QD film deposited by doctor blading.

The stability of doctor blading processed QD-solid is relevant in view of their optoelectronic applications. For this reason, the surface state of the PbS QD-solids in air before and after the ligand exchange was further studied by X-ray photoelectron spectroscopy (XPS). Figure 35a–c shows detailed XPS spectra of the S 2p, Pb 4f and O 1s core levels acquired in the QD-solids prepared for different ligand-exchange processing times. Several doublets, (p and f core-levels) and singlets (score-levels) can be deconvoluted from the XPS spectra. Before the ligand exchange, the S 2p and Pb 4f XPS spectra of the PbS QD-solid seem to be dominated by the presence of S $2p_{3/2}$ (Figure 35a) and Pb $4f_{7/2}$ (Figure 35b) lines at 160.9 0.2 and 137.9 0.2 eV, respectively, which are attributed to bulk-like PbS present at the core of the QDs.[119] This assumption is also supported by the fact that the intensity ratio analysis of these Pb 4f and S 2p components gives a S : Pb ratio of 1.4 : 1, reasonably close to unity. Besides the signal coming from bulk-like PbS, additional weak components at 164.0 and 166.6 eV can be resolved in the S 2p spectrum (Figure 35a), which stem from S–S bonds and $PbSO_3$ species located at the surface of the QDs. No traces are detected from other oxidized states of sulphur, such as $PbSO_3$. In the Pb 4f spectrum (Figure 35b) a component at 138.6 eV is resolved, which presumably arises from $PbSO_3$ and $Pb(OH)_2$ species.

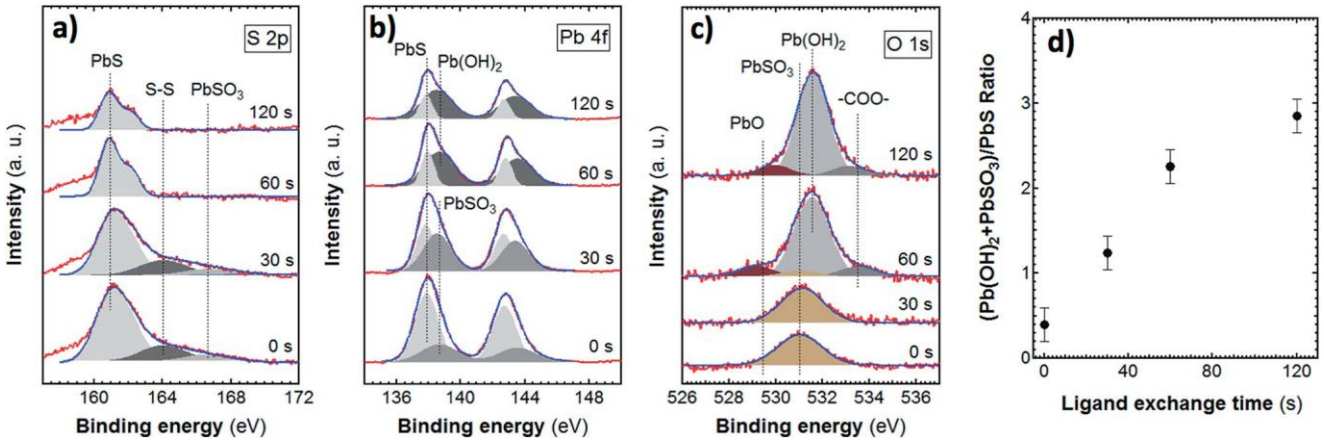

Figure 35: X-ray photoelectron spectroscopy of the PbS QD-solid before and after different times of ligand exchange. a) S 2p spectrum. b) Pb 4f spectrum. c) O 1s spectrum. d) Relative atomic ratio between oxygen-containing species and Pb bound to S at different ligand exchange process times.

Our XPS results also can bring some light into the question of the structural composition of the oxidized shell formed after the ligand exchange. Deconvolution of the O 1s peak measured in samples prepared for 60 and 120 s of ligand-exchange process reveals that the $PbSO_3$ component detected in PbS QD-solid before the ligand exchange becomes extremely reduced. At the same time, a new O 1s component emerges at 531.6 0.2 eV as well as two weak peaks located at 529.4 0.4 and 533.5 0.2 eV. The first weak peak at 529.4 eV can be attributed to PbO[120],[121] whereas the last weak peak at 533.5 eV seems to come from carboxyl groups of MPA. The main peak, at 531.6 eV, can be attributed essentially to $Pb(OH)_2$. This suggests that also the high energy Pb 4f component located at 138.6 eV mainly comes from $Pb(OH)_2$ after the ligand exchange, which is consistent with previous observations.[122] In fact, after aging the samples under room conditions (Figure 36a–c), XPS measurements revealed a continuous increase, of the $Pb(OH)_2$-related components to the whole Pb 4f and O 1s core levels, due to water adsorption from room atmosphere. In spite of these evidences, we cannot completely discard that other oxygen-containing species, such as carboxyl groups, may also contribute to the main O 1s peak.[123] The analysis of the XPS intensity ratio between the main O 1s component and the Pb 4f component corresponding to the oxygen-containing species yields an effective atomic ratio of 4 that becomes 2 after sputtering in ultra-high vacuum (Figure 37a–c), as expected for $Pb(OH)_2$. We can also notice that the Pb 4f and S 2p core level components attributed to PbS did not evidence any change in width, which indicates that oxidized shell effectively

passivates the surface and protects the bulk-like PbS core. XPS analysis also indicate the presence of Cl in every samples. Figure 37d exhibits a typical Cl 2p core level spectrum measured in the sample treated with 60 s of ligand exchange and kept in air for 3 months. The presence of this element raises the question about its residual role and the nature of its bonding to the PbS QD even if a clear Cl 2p core-level peak, no Pb–Cl related component have been clearly detected in the measured Pb 4f spectra around 139 eV. This fact may imply that Cl is a residual product of the PbS preparation but the behaviour of the Cl 2p peak after Ar^+ sputtering (Figure 37d) suggests that Pb–Cl bonding would take place, given that Ar^+ sputtering should enhance the signal from the PbS QD core and even break the existing Pb–S and Pb– O bonds.[87],[124] But, what is relevant here, is the observation that all core-levels related to PbS QDs shift by 0.4 eV to higher binding energies, which can be originated by a QD size reduction inherent to the sputtering process (the C 1s binding energy from residual C remains at 285 eV, which is not shown here). As all the PbS-related core levels do, the Cl 2p core level appears also to shift to higher binding energies, which indicates that these Cl are bound to the excess of Pb on the QD surface. This result is consistent with those recently reported and prove that the use of Cl anions for the synthesis introduces a Cl-based passivation layer that effectively prevents significant oxidation during long-term air exposure, passivate trap states, and provide charge balance. As a summary of XPS results for QD-solid after of 60 s of ligand exchange, the principal oxidation product $PbSO_3$ is extremely reduced but there is an increase of the overall size of the oxidized shell of the PbS QD because of the formation of other oxygen-containing species, mainly $Pb(OH)_2$. The exposure of the QD-solids to air leads to the increase of the $Pb(OH)_2$- related components due to water adsorption as confirmed by XPS after Ar^+ sputtering of the QD-solid surface but this oxide shell does not affect the structural quality of the bulk-like PbS core and effectively passivates the QD surface. Additionally, the use of Cl anions for the synthesis introduces a Cl-based passivation layer that increase the stability of the QD-solid during long-term air exposure. These findings should be specially considered for the development of optoelectronic devices based on these PbS QD-solid films.

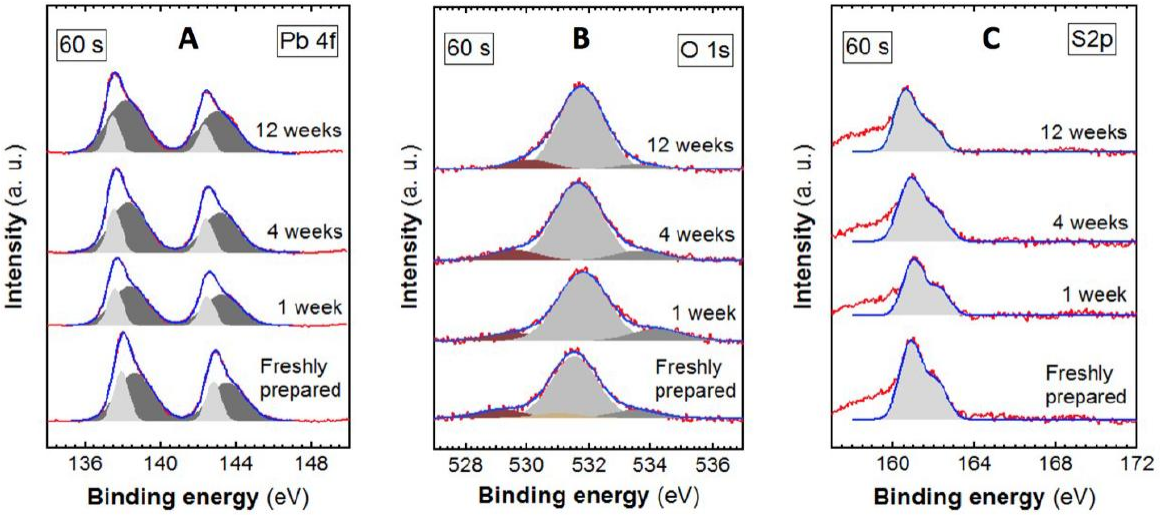

Figure 36: XPS measurements of the PbS QD-solids exposed to air for different times: a) Pb 4f, b) O 1s and c) S 2p spectra.

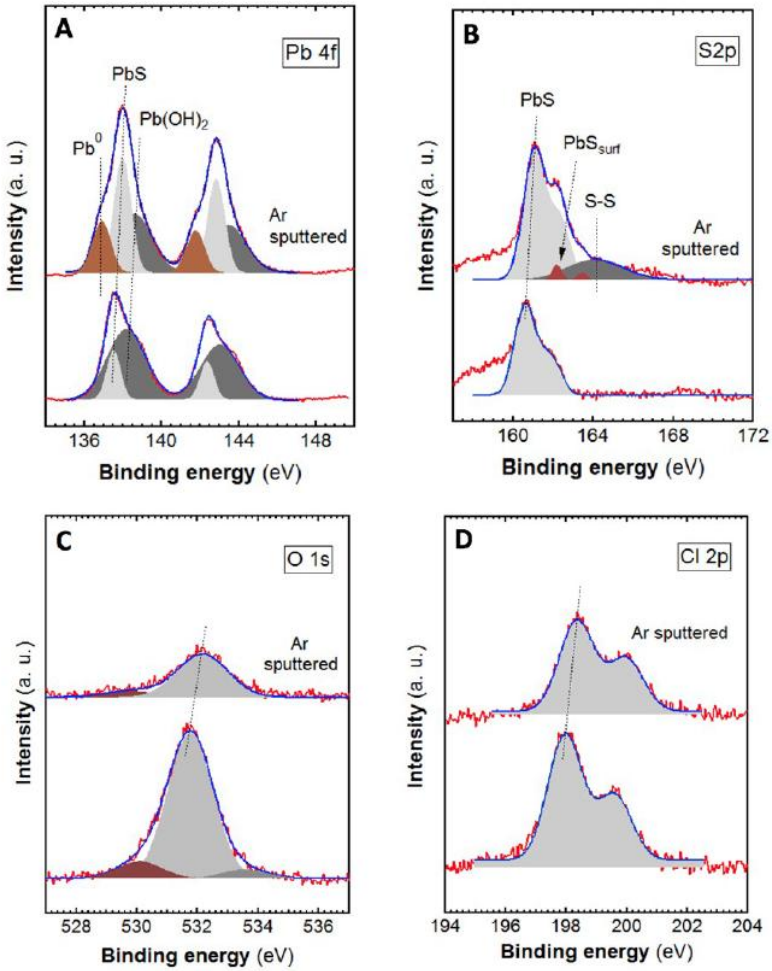

Figure 37: XPS measurements of the PbS QD-solids before and after Ar+ sputtering in ultrahigh-vacuum: A) Pb 4f, B) S 2p, C) O 1s and D) Cl 2p spectra. The samples were prepared under 60 s of ligand exchange

In final instance we carried out XPS analysis to compare TBAI and MPA ligand exchange on PbS QD-solids. Figure 38(a) shows the XPS spectrum in the case of TBAI-treated PbS QD-solids, where we observe an intense I 3d photoelectron doublet (brown-shaded peaks), whose j = 5/2 component appears at 619.1 eV. The presence of this peak is attributed to I bound to Pb at the QD surface with a I/Pb ratio of 1.2. At higher energies, a weaker I 3d photoelectron doublet (green-shaded peaks) is observed, whose j = 5/2 component is located at 620.6 eV, in this case ascribed to residual I-atoms forming IO_2^- ions, which in turn prevent the formation of lead oxidative species, as discussed below.

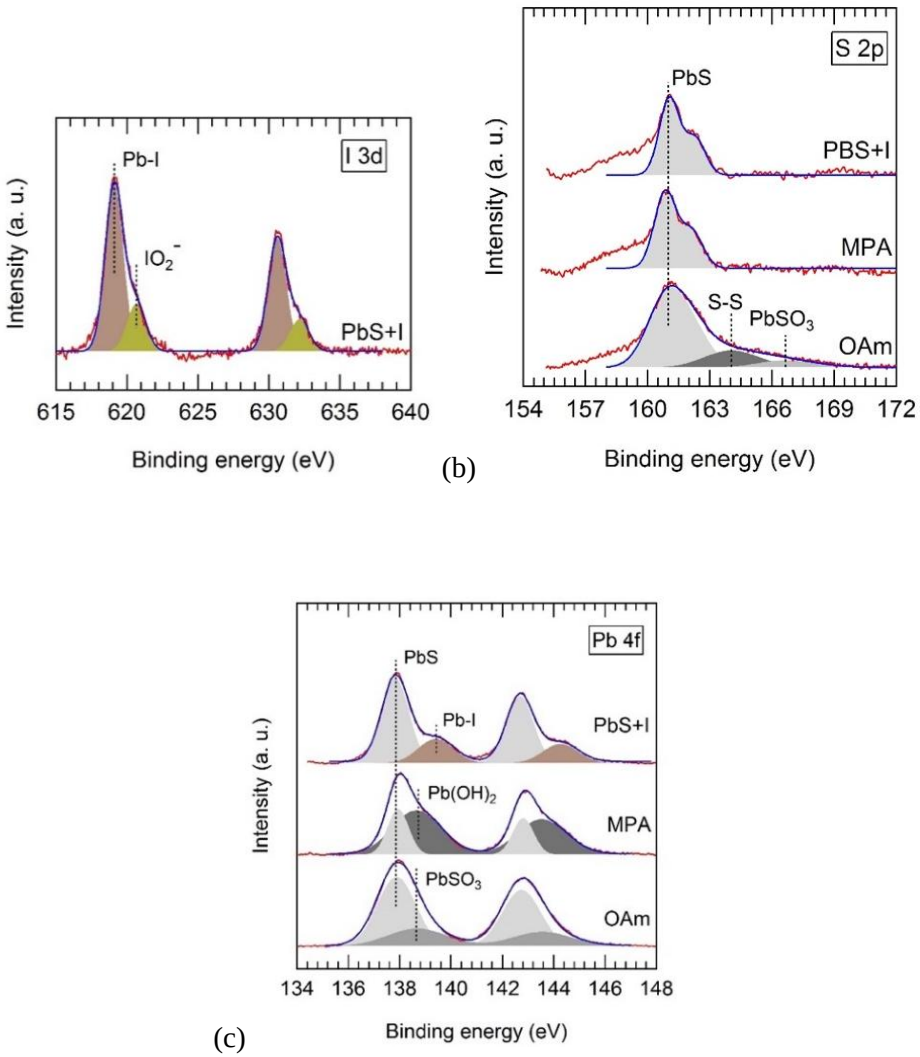

Figure 38. XPS spectra of the PbS QD-solid treated with TBAI (I 3d photoelectron lines) (a) and treated with TBAI and MPA compared to the untreated film in the energy regions of S 2p (b) and Pb 4f (c) photoelectron transitions.

The ligand exchange process produces strong changes on the chemical state of atoms at the surface shell of PbS QDs. The S 2p and Pb 4f XPS photoelectron spectra (Figure 38(b)-(c), respectively) were measured in samples prepared before and after ligand exchange. Before ligand exchange, the acquired XPS spectra appear to be dominated by spin-orbit doublets whose S $2p_{3/2}$ and Pb $4f_{7/2}$ components are located at 160.9 ± 0.2 and 137.9 ± 0.2 eV, respectively. These transitions can be attributed to bulk-like PbS present at the core of the QDs, as their XPS intensities, corresponding to a S:Pb ratio of 1.4:1, are reasonably close to unity.[35] Additional weak components at 164.0 and 166.6 eV can be resolved in the S 2p spectrum, which can be associated to S–S bonds and $PbSO_3$ species located at the surface of the PbS QDs. These species are

suppressed after the ligand exchange with both MPA and TBAI, as shown in Figure 38(b). However, a strong Pb $4f_{7/2}$ component located at 138.7 eV is revealed in the case of the MPA passivated sample that is ascribed to the presence of $Pb(OH)_2$ species at the surface shell of the QDs. This component seems to be strongly reduced with the TBAI post-deposition treatment where, instead, a new Pb 4f doublet is observed, whose j = 7/2 component appears at 139.4 eV, which is attributed to Pb atoms at the shell surface of the QDs forming Pb-I bonds as a PbI_2-like compound.

Chapter 5 Charge transport in trap-sensitized infrared PbS quantum dot-based photoconductors: pros and cons

In this chapter we present a PbS QD-solid-based photoconductor device operating in the third window of telecom wavelengths. By approaching this device architecture, we have been able to investigate the effects of altering the surface chemistry of PbS CQDs in QD-solids via solid-state ligand exchange using organic and inorganic passivating agents, respectively 3-mercaptopropionic acid (MPA) and tetrabutylammonium iodide (TBAI). More in detail, we investigate how the QD surface chemistry treatments influence the charge carrier dynamics in the PbS QD-solid thin film.

After the introduction of the state of the art and objectives of the study, the chapter unfolds with the device fabrication from the PbS CQDs deposition, (except the PbS synthesis that was described in Section 3.3.3), until the subsequent solid-state ligand exchange processes.

The resulting optoelectronic performances of the devices, supported by the QD-solids characterization, have been then discussed. We conclude that the devices treated with MPA lead to higher device performances in photo-sensitivity, responsivity and detectivity, mainly due to the smaller dark current and lower noise level as compared to the devices where ligand exchange with TBAI was performed.

In the chapter we also discuss how trap sensitization of the PbS CQDs occurs in the QD-solid after ligand exchange and influences the photoconductivity. We describe how it produces very high gain but slow time response under very low incident optical power (< 1 pW), as clearly established in the case of MPA-treated photodevices. For TBAI-treated photoconductors, dark and noise currents are more important and responsivity cannot be measured at such very low optical powers. In the case of high incident optical powers, where most traps are filled, the photocurrent is mostly determined by mobility and free carrier

lifetimes in both materials (MPA- and TBAI-treated PbS QD-solids), which is the reason to observe very close performance, but much smaller gain and responsivities.

5.1 Photoconductor detectors

As highlighted for photodiodes, photoconductor detectors based on conventional single-crystalline semiconductors introduce limitations in some massive applications (different kinds of optical sensors for domotics and biomedicine, for example) due to the high production costs, material incompatibilities, and the necessity of highly customized deposition systems. In Chapter 2 we presented the fundamental mechanism underlining photoconductor devices, focusing the attention on the case of semiconducting QD-solids as photoactive component of the device. The great potential of this new class of semiconductor materials reside in the possibility to directly tune their optical properties by quantum confinement effect and their solution processability which makes possible their application over a wide range of substrates, including post-processing atop integrated circuits. In this way, the application of lead chalcogenide QD-solids as thin films has revealed outstanding potential applications in high efficiency optoelectronics, such as solar cells,[125],[113] field-effect transistors,[12] light emitting diodes,[126] and photodetectors.[108],[87] Aiming for high optoelectronic performances of QD-solid-based devices the engineering of the QD-solid and the control of their chemistry have shown to be key factors.[82] ,[17]

The processing of CQDs for the production of solid-state films has been experimented through low cost, fast and straightforward solvent-based deposition techniques. Methods as drop casting, dip coating and spin coating have been extensively and mostly used for the fabrication of devices, as reported in literature.[86],[127],[128] Regardless the solution processing deposition method, the fabrication of compact and homogeneous QD-solids of controlled thickness with low structural defect concentration have been addressed to develop high efficiency photoconductor devices.[12],[68],[129] Alongside to the QD-solid fabrication techniques, significant work has been devoted to the study of chemical composition of the nanocrystal dispersion since it has shown to be a crucial factor in the optimization of charge carrier dynamics in QD-solids.[130]

In colloidal dispersion, lead chalcogenide CQDs are commonly surrounded by long aliphatic ligands, which have a stabilizing and passivating role allowing a flexible control over their size, shape and composition[131] while preventing the formation of aggregates. Since ligands set the potential barrier for

charge carrier transfer and transport in CQD-solids, long insulating ligands must be replaced with shorter ones in order to enhance the coupling between CQDs while still efficiently passivating their surface.[132],[17],[133] Several ligand exchange strategies have been reported for lead chalcogenides CQDs, both in solution and in solid-state using bidentate thiols,[111] primary amines,[51] carboxylic acids,[112] thiocyanate ions,[60] and halide ions.[113] Each one of these ligands has different chemical properties and selective affinity to the nanocrystal facets, bringing to distinctive behaviour of the charge carrier dynamics in the QD-solids.[59] Also, the ligand exchange procedure is relevant for charge carrier dynamics in the QD-solids, since CQDs surface defects can be also generated due to an incomplete ligand substitution or charge imbalance between the ligand and the surface states.[132] These surface defects in QDs are dependent on the length and the chemical structure of the capping ligands surrounding and interconnecting the QDs,[134] and introduce trapping states energetically located within the QD band gap that modify the photoconductivity kinetics.[6] On the one hand, the presence of these intra-gap states has detrimental effects on optoelectronic devices, so that a great effort has been dedicated to their passivation.[135],[136] On the other hand, all studies carried out on photoconductor detectors based on QD-solids suggest that some other intra-gap states are acting as sensitizer centres (or safe traps) leading to very high photoconductive gain (G).[27,28] This is because after electron–hole photoexcitation, electrons can easily be captured, while holes remain relatively free to move through the QD-solid. In any case, despite the available literature, the exact origin, the behaviour and the influence that intra-gap states have on the optoelectronic properties of QD-solids is yet not fully understood.[29] In PbS CQDs, the origin of intra-gap states has been attributed to an off-stoichiometry Pb-rich surface [17] or to charge imbalance between Pb atoms and capping ligands.[111] More recently, it has been demonstrated that lead oxides species, formed on the surface of the QDs after air exposure, play an important role on the electrical properties of PbS QD-solids They can firstly act as p-dopant agent and furthermore, acting as trapping centre whose charge carrier capture coefficient is about 400 times higher for electrons, [28] also being traps responsible for the increase in the effective minority carrier lifetime, as discussed below. Such a behaviour can be detrimental for the application of these nanocrystals in solar cells or light-emitting diodes: however, in photoconductors it gives rise to a high G-value under very low power excitation, when an external electric field is applied.[28] This mechanism can lastly be a path to efficiently increase the photoconductor detectivity, but it also limits the temporal

response of the device, which requires short carrier lifetime and fast charge-carrier collection. Is then evident that these conditions establish a fundamental trade-off towards the achievement of high gain and large bandwidth in photoconductors.[36]

Here we present the study of PbS QD-solids-based infrared photodetectors fabricated in ambient condition using a simple and low-cost techniques.

The devices metal contacts were patterned by UV-photolithography and lift-off processing prior to the PbS QD-solid formation. We initially approached the production of QD-solid-based photoconductors by spin coating, drop casting and doctor blading method for the deposition of PbS Nanoinks over microgaps and interdigital electrodes, in order to determine the most promising technique. The best performances have been achieved by processing the nanoink using the doctor blading deposition method. Then we focused our efforts on defining the influence of QDs passivation strategies on the charge dynamics in the QD-solids. Specifically, we direct our findings on the effects of two different post processing solid-state ligand exchange treatments using the bidentate aliphatic thiol 3-mercaptopropionic acid (MPA) and the iodine-containing ligand tetrabutylammonium iodide (TBAI). The interest on approaching these two passivation strategies arise from the understanding of how their different chemical nature influences the QD-solid properties and the effects on the electro-optical properties of the device. The use of ligand exchange by MPA, which has both thiol and carboxylate functional groups, provides a high passivation action over a broad distribution of PbS surface states, simultaneously enabling high electronic coupling among QDs (enhanced electronic wavefunction overlap) [132] Instead, the post-processing treatment with TBAI has been approached aiming to further enhance the QD-coupling introducing I^- ions as passivating agent that bind to Pb^{2+} dangling bonds at the PbS surface.[117] Additionally, the formation of PbI_2 at the surface with I^- : Pb^{2+} ratio 1 : 1 can result in the formation of a PbI_2 shell-like structure to the PbS core, which can be considered as a passivation action resulting from the reaction precursor.[118] We finally compare TBAI to achieve short interparticle distances, with MPA, which likely would lead to a more complete passivation of the QD surface defects,[132] in order to define how these different strategies influence the optoelectronic performances of QD-solid-based photoconductors. Our results, based on the correlation between the electronic properties of the film deduced from XPS-measurements and the electro-optical properties of the

photoconductor devices, confirm that MPA-treated films lead to superior responsivity (≈ 80 A/W at 1550 nm), due to very low conductivities under dark conditions (low free carrier concentration or doping), and higher detectivities (D* ≈ (1-5) $\times 10^{12}$ Jones). Contrary to the aprioristic assumption expressed above, TBAI-treated QD-solids lead to higher dark conductivities that limits the sensitivity and detectivity of photodevices. This is ascribed to an additional charge transport mechanism related to mid-gap states, even if mobility is significantly smaller than in MPA-treated films. We have modelled the photocurrent (and responsivity) by including the excess of minority carrier photogenerated by absorption and the presence of a single trap level that nicely reproduces the observed evolution with light power received by photoconductors, both MPA- and TBAI-treated. This modelling explains the high observed responsivities under very low incident powers (if photocurrent is superior to noise current) because most of photogenerated carriers are trapped (usually known as sensitization of the photoconductors), whereas free minority carriers are responsible of photocurrent/photoconductivity in the QD-solid.

5.2 Architecture and devices fabrication

The photoconductor devices are schematically represented in Figure 39, where a QD-solid film 300 nm thick is deposited by doctor blading approach onto silicon-SiO_2 substrates with gold electrodes pairs (80 nm thick) at of 2, 5, and 20 µm interelectrode distances.

The electrode patterns were previously prepared by UV-photolithography and lift-off processing, while the gold was deposited by thermal evaporation under vacuum (2-4x10-5 Torr) at a rate in the range 0.1-0.3 nm/s. Gold electrodes allow the formation of an ohmic contact with the QD-solid. Due to the planar configuration of the photoconductor the illumination can be performed from the top surface.

Prefabricated OFET ("Organic Field Effect Transistor") Test Chips, which are very similar to our own fabricated chips, were mounted on an Ossila High Density OFET Test Board, designed to reduce external noise, leakage current and stray capacitance. Once deposited the PbS QD-solid on these chips we were able to measure I-V characteristics for different gate voltages in order to estimate carrier mobility. We have also fabricated simple Schottky-like diodes glass/ITO/PEDOT/QD-solid/Ag, where the QD-solids (MPA and TBAI treated) were produced using the same fabrication process and conditions carried out for the photoconductors.

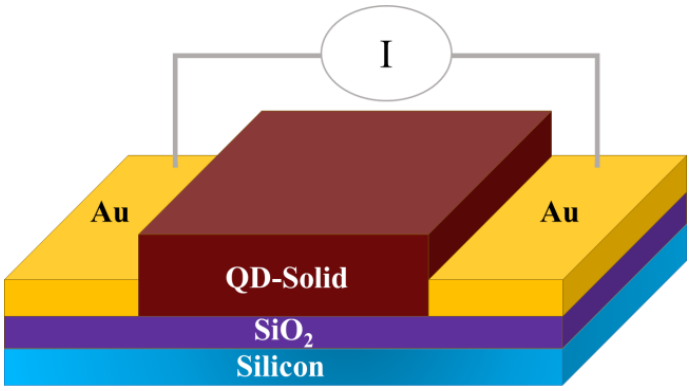

Figure 39: Structure scheme of a QD-solid-based microgap photoconductor.

5.2.1 Results and Discussion

The fabrication of PbS QD-solid-based photoconductor detectors was carried out by solution processing of a PbS nanoink formulated for doctor-blade technique, as aforementioned.

The formulated nanoink exhibits a surface tension of 36 dyn cm^{-1} and a contact angle of ~ 6° onto SiO_2/Si substrates (full details were given in Chapter 4). The PbS QDs synthesized for this study, presented an average diameter of 6.4 nm with a size dispersion of ~9 % (Figure 40(a)), showing the excitonic absorption and the photoluminescence resonances cantered at 1520 and 1575 nm, respectively, with a bandwidth of 140 nm, (Figure 40(b)).

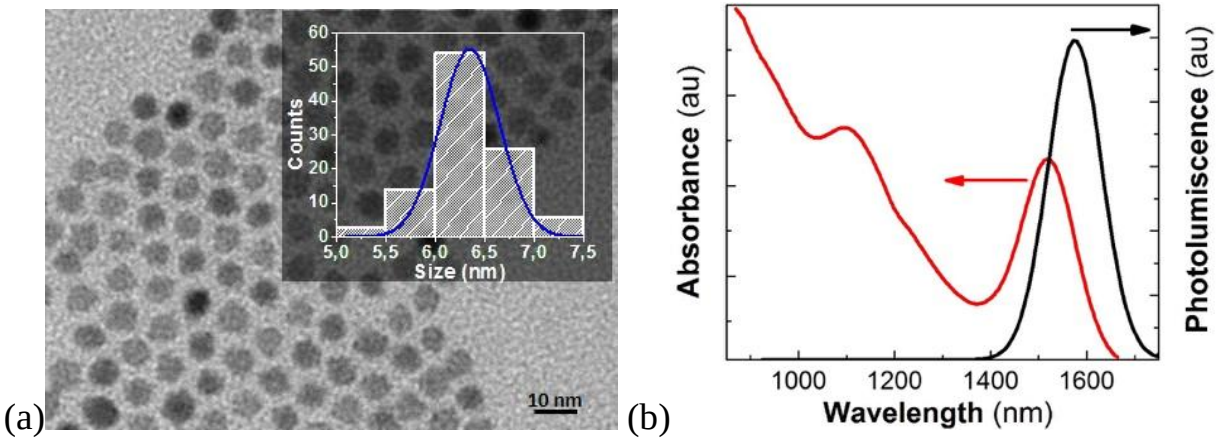

Figure 40: (a) Transmission electron microscopy image of PbS QDs and size histogram (inset). (b) Absorbance and photoluminescence spectra measured in the QD nanoinks.

Thin films 300 nm-thick of PbS QD-solids were fabricated by doctor blading technique. The ligand exchange process was carried out with TBAI and MPA after the film formation as described in Chapter 4. High quality homogeneous films were obtained. Neither cracks nor pinholes appeared in the QD-solids after the ligand exchange as evidenced by the cross-sectional SEM imaging (Figure 28, Chapter 4), and previously reported by us and other authors.[108],[137] In Figure 41 we can observe the influence of the ligand exchange on the absorbance measured in the corresponding PbS QD-solids. The exciton absorption resonance is clearly observed very close to 1600 nm before and after MPA ligand exchange. However, the TBAI treated film shows a more important broadening of the absorption band.

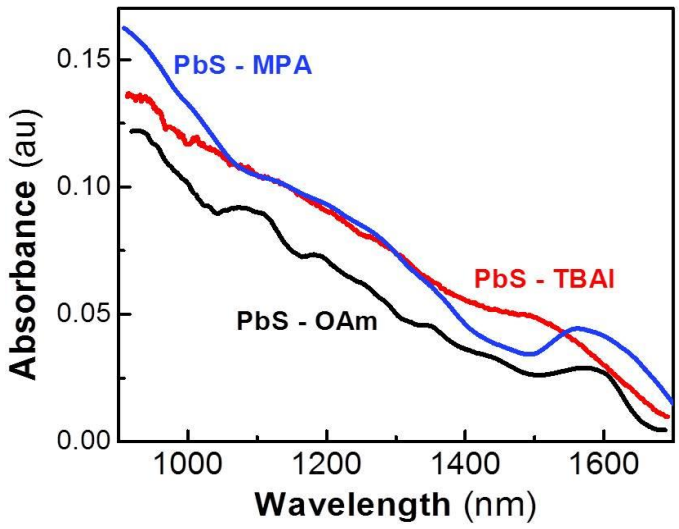

Figure 41: Absorbance spectra of PbS QD-solids measured (a finite background absorbance due to scattering was subtracted from the raw spectra) in untreated (black) and after post-deposition ligand exchange with tetrabutylammonium iodide (TBAI; red) and 3-mercaptopropionic acid (MPA).

Given that inter-particle spacing among PbS QDs decrease dramatically after ligand exchange (Figure 42), the QDs treated with TBAI probably merge into bigger PbS particles (or agglomerates), losing part of their quantum confinement character.[17] On the other hand, this effect is not observed in the MPA-treated PbS solids, which in turn allows to maintain the quantum confinement properties while keeping short interparticle distances (Figure 42), and hence, leading to a more homogeneous QD-solid with given electronic coupling between QDs.

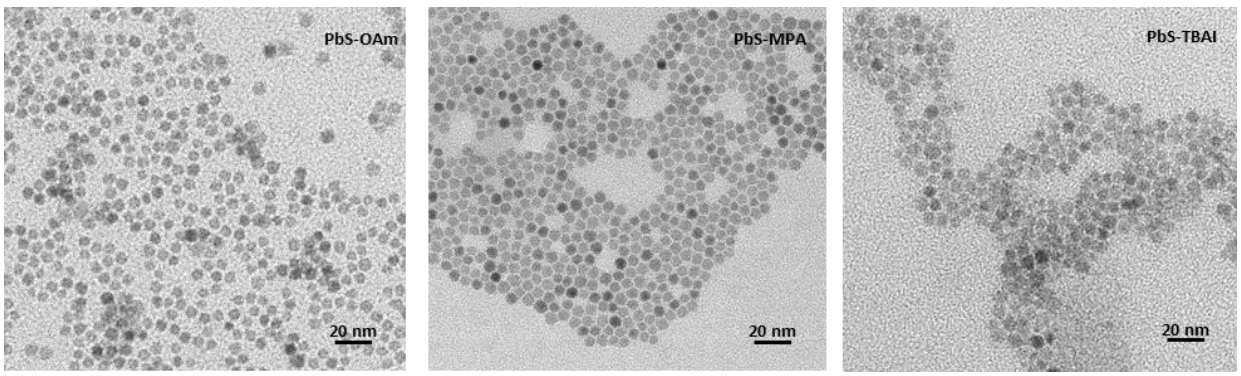

Figure 42: Transmission electron microscopy image of PbS QDs with different surface ligands. From left to right: PbS-OAm; PbS-MPA; PbS-TBAI.

Ligand exchange of PbS solids with TBAI and MPA was also followed by XPS measurements (see the results and the corresponding discussion in Chapter 4), where we can see in detail the strong changes that the ligand exchange process produces on the chemical state of atoms at the surface shell of PbS QDs. Before ligand exchange, the acquired XPS spectra appear to be dominated by transitions that can be attributed to bulk-like PbS present at the core of the QDs with additional weak components associated to S–S bonds and $PbSO_3$ species located at the surface of the PbS QDs. These species are suppressed after the ligand exchange with both MPA and TBAI. However, a strong component ascribed to the presence of $Pb(OH)_2$ species at the surface shell of the QDs is present in the MPA passivated sample. Such effect seems to be strongly reduced with the TBAI post-deposition treatment, where Pb atoms at the shell surface of the QDs are forming Pb-I bonds as a PbI_2-like compound. From XPS results we can finally conclude that QD-solid films prepared under ambient conditions are very different. When conserving the original ligands (OAm), oxidation is observed at the surface shell of PbS QDs, whereas after ligand exchange by MPA and TBAI different bonds are revealed, Pb-OH and Pb-I, respectively, other than the presence of IO_2^- ions in the latter case. We will see in the next section how these different passivation treatments influence the electro-optical properties of the corresponding PbS QD films.

5.3 Optoelectronic Characteristics

5.3.1 Current Voltage Measurements

Figure 43 shows the current-voltage curves for photoconductor devices (see insets) presenting various inter-electrode gaps under dark and white light illumination between 0 and 10 V of bias voltage, and all the parameters extracted from these curves are listed in Table 2. Clearly, MPA treated PbS-QD layers (panels in Figure 43 (a)) display smaller dark current levels (black curves) and larger photocurrents (red curves) than TBAI treated ones (panels in Figure 43(b)). Such differences are translated into photo-sensitivities, defined as $S = (I_L-I_D)/I_L = \Delta\sigma/(\sigma_0+\Delta\sigma)$ (I_L and I_D are the currents measured under illumination and dark conditions at a given voltage, σ_0 and $\Delta\sigma$ the QD-solid conductivity and photoconductivity, respectively), which are very close to the unit in the first case, as listed in Table 2, and also in more important responsivities and detectivities, as will be presented and discussed below.

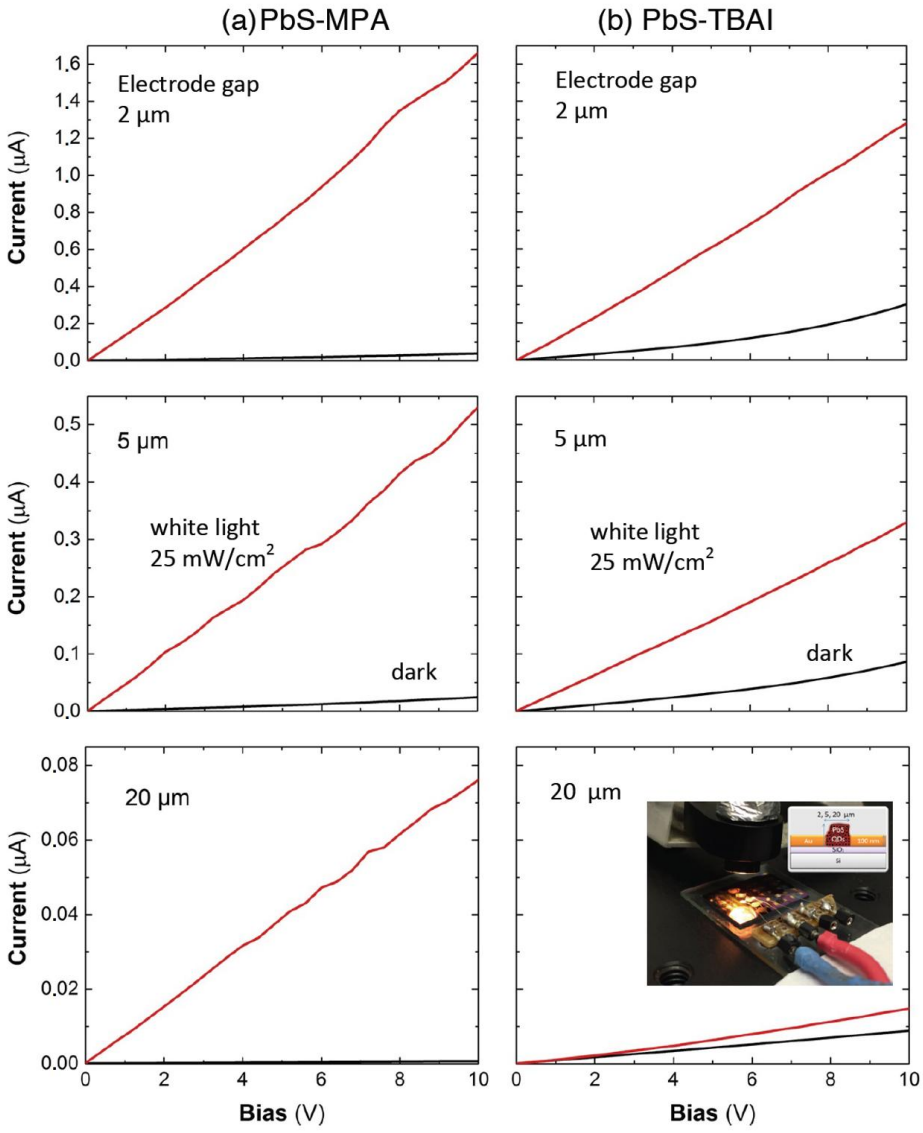

Figure 43: Current–voltage characteristics in the dark (black lines) and under 25-mW/cm^2 halogen lamp illumination (red lines) of processed PbS colloidal QD photoconductors: MPA-treated (**a**), and TBAI-treated (**b**). The inset in the bottom-right panel shows the three contacted photodevices under white-light illumination (the picture also includes a scheme of the photoconductor detector).

The dark current is not linear in the whole range of applied voltage(0-10 V), more evident in the case of TBAI-treated samples for 2- and 5-µm-wide electrode gaps (see Figure 43 (b)), which was the reason to give a range of variation for the dark conductivity σ_0 (see note in Table 2).

Table 2: Conductivity under dark conditions (σ_0), photoconductivity ($\Delta\sigma$) and photoconductive sensitivity (S) of processed PbS QD photoconductors treated with MPA and TBAI ligands, as deduced from I-V curves in Figure 43.

	MPA			TBAI		
Gap (μm)	σ_0^* (μS/cm)	$\Delta\sigma$ (μS/cm)	$S = (I_L-I_D)/I_L$	σ_0^* (μS/cm)	$\Delta\sigma$ (μS/cm)	$S = (I_L-I_D)/I_L$
2	0.20-0.37	8.5	0.97	1.0-4.0	6	0.82
5	0.33-0.58	5.3	0.93	0.9-2.6	4	0.76
20	0.03-0.05	0.95	0.93	0.58	0.20-0.65	0.2-0.4

* The I-V under dark conditions exhibit a near-quadratic behaviour on applied voltage more evident above 4-5 V, hence we have included a range of variation for σ_0, being the smallest/highest value corresponding to low and high bias voltage regions; this effect is less important in the case of the photoconductor with electrodes separated 20 μm (weaker electric fields). In the case of $\Delta\sigma$ deduced from I_L-I_D versus voltage the variation is mostly linear, and the value is obtained with a relative error of around 10 % (except for the photoconductor with the largest gap treated with TBAI in which the range of variation is included).

The aforementioned nonlinear behaviour is better observed in a double logarithmic plot (Figure 44). The measured I-V curves (data symbols in Figure 44) can be nicely fitted through a response function:[138]

$$I = aV + bV^m \qquad 20$$

where a, b and m are fitting parameters. The coefficient a would be the ohmic conductance, whose associated conductivity would be very close to the smallest value listed in Table 2 for the different photoconductors. This response is due to space-charge limited current (SCLC) effect that occurs when uncompensated charge carriers are injected in the material, as reported for Si-nanocrystal films.[138]

The best fit to previous SCLC equation (continuous lines in Figure 44) yields m = 3.5 for the I-V curves measured in photoconductors with 2 and 5 μm of channel length (in the 20 μm device the potential

behaviour is practically absent in the measured voltage bias range) and only b is decreases with the channel length (b would contain the channel length that defines electric field inside the material). In the presence of traps, part of the injected carriers can be considered as free and exponent m may be greater than 2.[138] The I-V curves measured under dark conditions in MPA-treated PbS QD-solid the nonlinear behaviour is less important in this voltage range, but similar fits can be made by using approximately the same values for m and smaller b-values (a factor 3 smaller when comparing TBAI- and MPA-treated photoconductors with 2 μm of channel length).

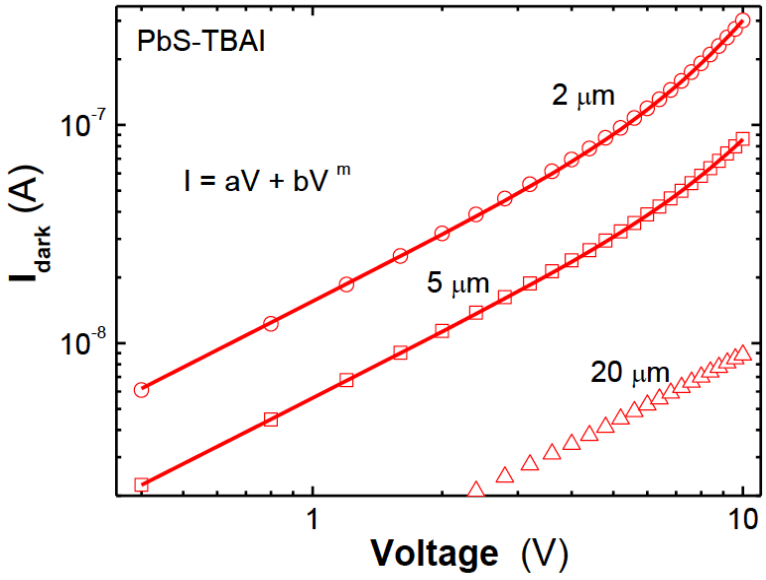

Figure 44: Double logarithmic plot of the I-V curves (data symbols) measured under dark conditions in the PbS-TBAI photoconductors. The best fit to the SCLC equation is obtained for *m* = 3.5. Coefficient *b* is smaller and practically negligible for the photoconductors with 5 and 20 μm of channel length, respectively.

The conductivity values estimated in the case of the photoconductor devices with a gap electrode of 20 μm (mostly for MPA-treated QD-solids) are smaller than those obtained in the case of devices with gap electrodes 2 and 5 μm wide, possibly because the resulting thickness of the QD-solid film is smaller in the first case. In average, the conductivity measured in the QD-solid through 2 - 5 μm wide electrodes is

$\sigma_0(MPA)$ ≈ 0.4 µS/cm after MPA treatment and increase up to a factor six, $\sigma_0(TBAI)$ ≈ 2.5 µS/cm, in the case of TBAI (despite the absolute values, a similar increase in conductivity from MPA to TBAI processing is observed for the 20 µm wide electrode). Given that $\sigma_0 = q\ \mu_p\ p$, where μ_p and p are the hole mobility and concentration, respectively, assuming that the QD-solid is p-doped (particularly after MPA treatment),[36] the smaller dark conductivity in MPA-treated films could be attributed to smaller values of one or both magnitudes as compared to TBAI-treated ones.

5.3.2 Effective Mobility and Acceptor Concentration Estimation

The small dark conductivities and very low hole mobility of the QD-solid films make very difficult to achieve precise Hall effect measurements; hence two independent estimations were made in the present work. The first one is related to the hole mobility measured in FET devices and the second one is the acceptor concentration deduced from the slope of $C^{-2}(V)$ curves measured in Schottky-like ITO/PEDOT/QD-solid/Ag devices, presented in Chapter 6.

The field-effect mobility measurements give an important insight of how the passivation strategy influence the charge carrier transport in the PbS QD-solids, as shown in Figure 45. The field-effect mobility in the linear regime is determined using the characteristic output curves of the field-effect transistor (FET), given by the plot of drain–source current (I_{DS}) versus gate voltage (V_{GS}) for a given drain voltage (V_{DS}) bias. The output curves can be divided in two regions: the linear region and the saturation region. The slope of the linear region can be used to obtain the charge carrier mobility by the following Equation, valid if charge carrier mobility is assumed to be temperature and field independent:

$$\frac{\partial I_{DS}}{\partial V_{GS}} = \frac{W}{L}\mu C_S V_{DS} \qquad 21$$

where L is the channel length (results in Figure 45 correspond to 30 µm), W (1 mm) is the channel width and C_S the capacitance of the insulating layer 300 nm thick in Ossila substrates, whose value is 1.15×10^{-8} Fcm^{-2}. The Drain-Source voltage has been set at 1V. To ensure field independency, mobility has been measured for different channel lengths. The mobility obtained in several PbS-MPA FET devices result in

the range of (1-4) $x10^{-4}$ $cm^2V^{-1}s^{-1}$, whereas PbS-TBAI passivated films displays a carrier mobility of (2-6) $x10^{-5}$ $cm^2V^{-1}s^{-1}$, as represented by the linear fits in Figure 45 (continuous lines).

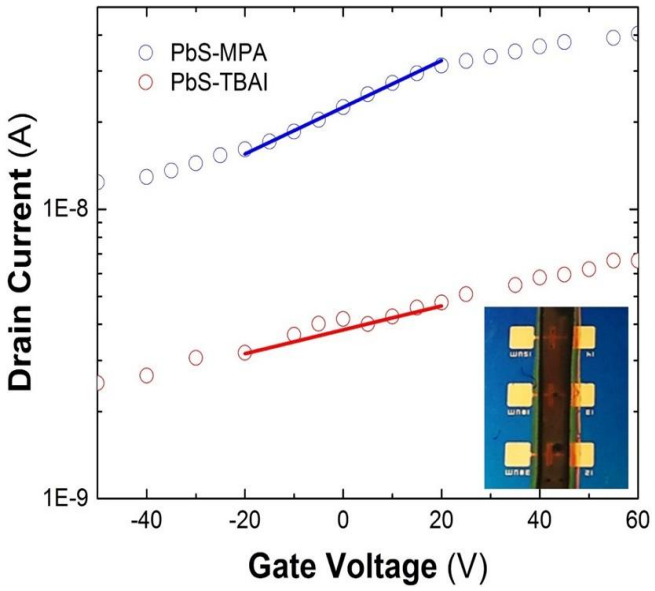

Figure 45: Transfer FET curves of processed PbS colloidal QD photoconductors treated with MPA (red curve) and TBAI (green curve). The inset shows the QD-solid film deposited by doctor blading technique in three FET devices prior to treatment by TBAI and MPA.

For PbS-TBAI QD-solids we found higher dark conductivity levels than in the case of PbS-MPA Table 2. The electrical conductivity in a p-doped semiconductor is directly proportional to the hole mobility and the free hole concentration. Above we estimated carrier mobilities from FET devices, but they are a factor five different, being smaller for TBAI-treated QD-solids, hence the free hole concentration should be significantly higher in this case with respect to MPA-treated films, as demonstrated below. From the slope of $C^{-2}(V)$ curves measured in Schottky-like diodes glass/ITO/PEDOT/QD-solid/Ag devices (Figure 46), we can deduce the doping concentration for both TBAI- and MPA-treated PbS QD-solids giving rise to the built-in Schottky barriers[139].

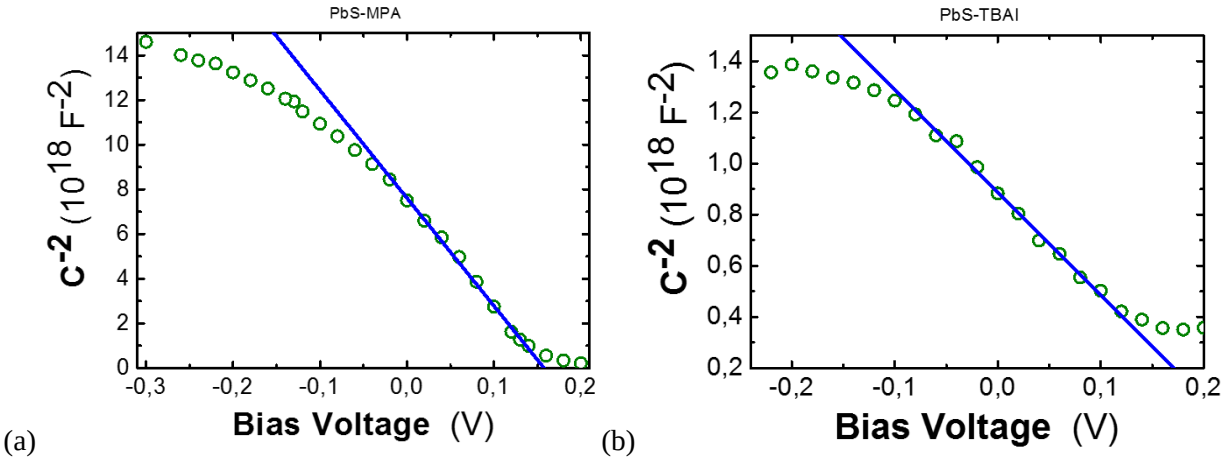

Figure 46: C–V characteristics of ITO/PEDOT/PbS/Ag Schottky devices with ligand exchange (a) PbS-MPA and (b) PbS-TBAI.

In Table 3 are listed the effective mobility, estimated from drain current versus gate voltage in FET devices (Figure 45), and the acceptor concentration, obtained from the $C^{-2}(V)$ curves in Schottky photodiodes form (Figure 46).

Table 3: Acceptor concentration and mobility of processed PbS QD-solids treated with MPA and TBAI ligands, as obtained from data shown in Figure 45 and Figure 46. From these values, estimated conductivity and drift/transit time are also listed.

	MPA	**TBAI**
Acceptor concentration, Na (cm^{-3})	1.9×10^{15}	2.3×10^{16}
Hole Mobility, μ_p ($cm^2V^{-1}s^{-1}$)	$(1\text{-}4) \times 10^{-4}$	$(2\text{-}6) \times 10^{-5}$
Conductivity, $\sigma_0 = q\,\mu_p\,p$ (µS/cm)	0.03 – 0.12	0.07 – 0.22
Transit time, $\tau_t = L^2/\mu V$ (µs) L = 5 µm, V = 100 V	6 – 25	40 – 125

The concentration of acceptor impurities estimated for TBAI-treated films is one order of magnitude higher than that for MPA, but mobilities are significantly smaller, possibly due to an effect of nanocrystal agglomeration, as suggested above, instead of an average smaller inter-particle distance. From these values, the conductivity deduced for MPA-treated QD-solid films (Table 3), within the spread found in the hole

mobility, (1-4) x 10^{-4} cm^2/Vs (values recently reported are within this interval),[137] is consistent with values deduced from I-V curves of photoconductor devices (Table 2). A greater difference is observed in the estimation of dark conductivity for TBAI-treated QD-solid films, 0.07 – 0.22 µS/cm (Table 3), as compared to those measured from I-V curves of photoconductors, from 0.58 up to 4 µS/cm (Table 2), which can be attributed to a noticeable contribution to charge transport of a weakly conducting mid-gap energy band formed from deep levels originated at the surface of the PbS QDs after formation of the QD-solid.[140] In this sense, the low built-in potential barrier, V_{bi} ≈ 0.15 V, deduced from C^{-2}(V) curves in the Schottky photodiodes (Figure 46), is also consistent with V_{OC} values (≈ 0.1 - 0.3 V, see Figure 47) as deduced from I-V curves under AM1 illumination in these diodes. Such low V_{bi} and V_{OC} are a signature of the presence of mid-gap states in both TBAI- and MPA-treated QD-solid films. However, in the latter case, the charge transport seems mainly due to free holes in the valence miniband of the QD-solid, as formed from the three-dimensional electronic coupling of QDs, which are spatially ordered as a BCC Body Centred Cubic lattice.[108]

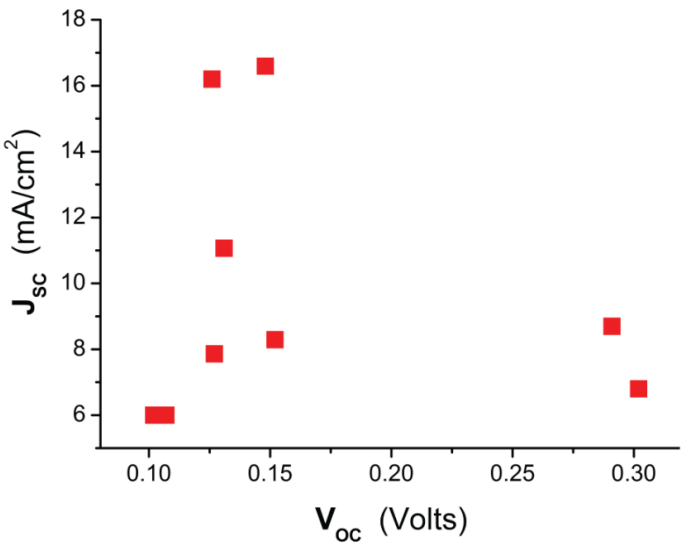

Figure 47: Short circuit photocurrent densities plotted against open circuit voltages measured in the same device under AM1 conditions for different Schottky photodiodes based on MPA-treated QD-solids (300-600 nm thick).

5.3.3 Responsivity Measurements and Safe Traps Modelling

The responsivity curves in Figure 48(a) exhibit a very similar wavelength dependence to that observed in the corresponding absorbance spectra reported in Figure 41 , as expected if the photocurrent was proportional to the absorption coefficient spectrum of the material (if diffusion and surface recombination does not have an important effect). Again, the exciton resonance is much less pronounced in the TBAI-treated photoconductor device, as discussed above for absorption spectra in Figure 41. The photoconductors (electrodes with 5 µm of channel length) exhibit peak values of around 0.45 and 0.35 A/W at the exciton resonance (≈1550 nm) for MPA- and TBAI-treatments, whereas increases for shorter wavelengths due to the larger absorption coefficient of the PbS QD-solid up to 0.9 and 0.7 A/W at 950 nm, respectively. It is worth noting here that the spectral dependence of responsivity was measured at the maximum optical power of the halogen lamp (power density of ~40 µW/cm^2 at the exit slit of the monochromator at 1550 nm, i.e., ≈ 2 nW captured by the photodevice with 5 µm of channel length). The effect of incident optical power on photocurrent (Figure 48(b)) and responsivity (Figure 48(c)) will be discussed below on the basis of the *safe trap* model illustrated in Figure 48(d).

Figure 48 shows the power dependence of photocurrent measured at around the exciton resonance, 1550 nm, using a bias voltage of 100 V for all photodevices, except in the case of the 2 µm wide electrode gap, where the photocurrent above 50-60V saturates, because of the sweep-out effect of minority carriers (electrons)[38] under such a high electric field (>200 kV/cm), for which the transit time, on the order of 1 µs for this electrode, is comparable to their lifetime. The photocurrent increases over the entire range of incident power, but much faster above ≈ 20 pW in the case of photoconductors with 5 µm wide gap electrodes (above ≈ 100 pW in the case of the 20 µm ones). This behaviour would be consistent with the expected linear power evolution of the photocurrent, or, similarly, proportional to $g\tau$, where g is the carrier generation rate and τ, the minority carrier lifetime, from the simplest generation-recombination model for photogenerated minority carriers. However, we can see that below those powers the photocurrent practically does not vary significantly, which cannot be reproduced with such a simplest model, but it is the origin of the huge increase of the responsivity at very low powers, as observed in Figure 48(c). In the case of the MPA-treated photoconductor with 2 µm wide channel length and the 5 µm TBAI-treated one we

were not able to observe the photocurrent saturation effect at very low optical powers, but here the dark and noise currents are more relevant and hence near impossible to measure very low photocurrents (using 1-3 s of integration time in the lock-in amplifier). Correspondingly, the two optical power regimes described for photocurrent are translated into a sharp decrease of responsivity by increasing the incident optical power and a saturation regime above such indicated powers.

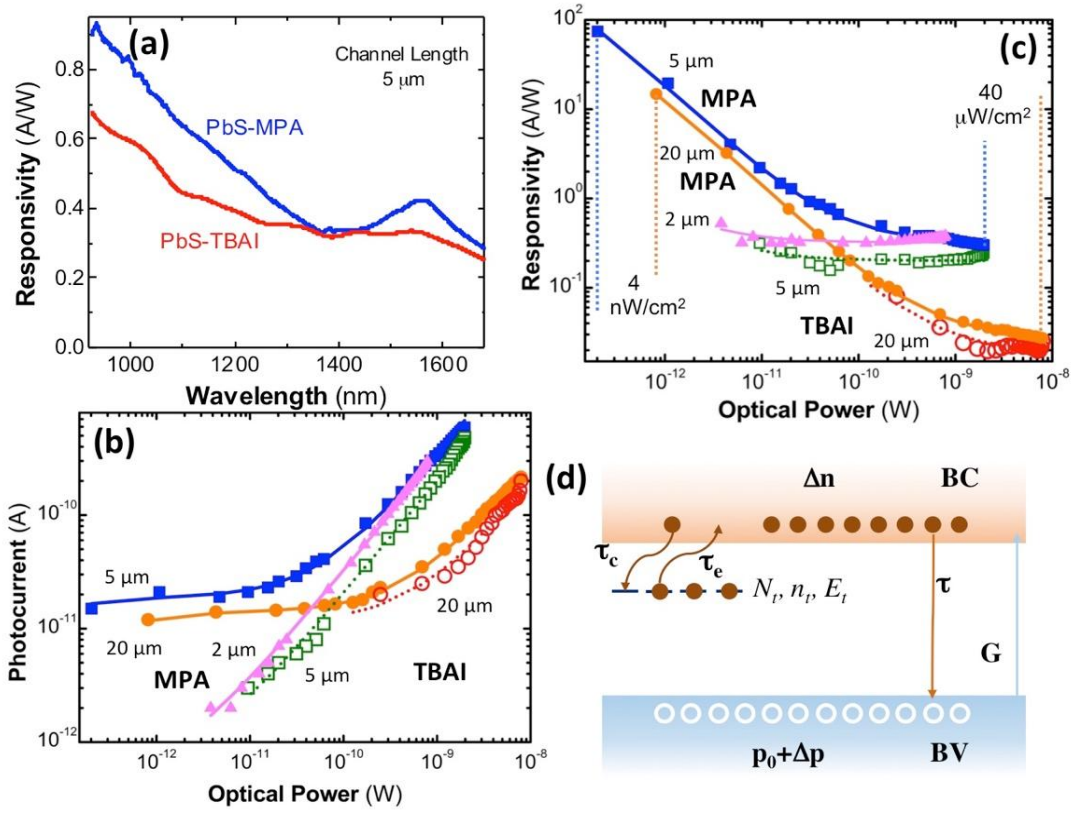

Figure 48: (a) Responsivity spectra of 5 µm gap photoconductors under 100 V bias for PbS-MPA (blue) and PbS-TBAI (red) treated films. (b) Experimental (symbols) and calculated (lines) photocurrent of MPA- (solid symbols) and TBAI-treated (hollow symbols) photodevices as a function of optical power received by them (electrode gap width is indicated in the plot) at 1550 nm and 100 V of voltage bias (50 V for 2 µm wide electrode gap) (c) Idem for Responsivity; the measured range for power density is indicated. (d) Illustration of the kinetic model for minority carrier recombination including the presence of photoconductive sensitized centres (safe traps).

The great responsivity values at very low incident powers and the subsequent fast decrease with power is typically attributed to trap assisted sensitization of photoconductivity in semiconductors and, particularly, in PbS QD-solids.[141] The best measured value in our MPA-treated PbS QD-solid photoconductors reaches ≈ 80 A/W for the MPA-treated photoconductor with 5 µm wide channel length under 200 fW of incident monochromatic light of λ =1550 nm. Given the spectral dependence depicted in Figure 48(a), the responsivity at 950 nm would be a factor two bigger than those measured at 1550 nm (≈ 160 A/W). Therefore, the responsivities measured in MPA-treated photodevices are among the best values reported in literature at the near-infrared region 1000-1600 nm, as summarized in Table 4, where some of the most important results collected in Reference [30] and more recent data are listed.

Table 4: Performances of different photoconductive detectors based on PbS nanocrystals (standard data for PbS bulk is also included).

Photoactive Material (Ligand treatment)	**Type**	**Spectra range (nm)**	**Responsivity**	**Detectivity (Jones)**	**Rise/Decay time and/or Bandwidth**	**Reference**
PbS-bulk	Photoconductor	1000-3000	5×10^{4} V W^{-1} (0.1 A W^{-1} for 500 kΩ load)	1×10^{11}	-	[30]
PbS NC (Butylamine)	Photoconductor	800 - 1500	2700 A W^{-1}	1.8×10^{13}	18 Hz	[30]
PbS NC (Butylamine)	Photoconductor	400 - 900	113 A W^{-1}	5×10^{12}	8 Hz	[30]
PbS NC (As_2S_3)	Photoconductor	900-1550	200 A W^{-1}	1.2×10^{13}	8 Hz	[30]
PbS NC (OH^-/ S^{2-})	Photoconductor - interdigitated	NIR < 2400	50 / 8 A W^{-1} (1550 nm, 230 K)	$(3.4/2.8)\times10^{8}$	40 Hz	[30]/[142]
PbS NC:Ag NP (EDT)	Photoconductor	400-1700	5 A W^{-1}	2.5×10^{11}	200 Hz	[30]
PbS NC:Ag NC (MPA)	Photoconductor	350-800	4 mA W^{-1}	7.1×10^{10}	9.4 Hz	[30]
PbS NC:PBCM (EDT)	Photoconductor	800-1400	57 %	4.4×10^{7}	330 kHz	[30]
PbS NC:MWCNTs (MPA)	Photoconductor	VIS-NIR	0.583 A W^{-1}	3.2×10^{12}	-	[30]
PbS NC (Oleic Acid)	Photoconductor - interdigitated	850 - 1550	30 A W^{-1}	2×10^{10}	160 ms / 3 s 0.1 Hz	[143]
PbS NC (bilayer EDT/TBAI)	Photoconductor	450 - 1100	0.27 A W^{-1} (580 nm)	1.7×10^{12}	3.6 / 30 ms 0.1 Hz	[144]
PbS/Graphene (EDT)	Phototransistor	600-1600	10^{7} A W^{-1}	7×10^{13}	10 Hz	[142]

PbS/MoS_2 (EDT)	Phototransistor	500-1150	6×10^5 A W^{-1}	5×10^{11}	-	[142]
PbS/WS_2	Phototransistor	vis-NIR	14 A W^{-1}	3.9×10^8	153/226 µs	[145]
PbS/ZnO	Phototransistor	UV-NIR	0.051 A W^{-1}	3.4×10^8	9/2 s	[146]
PbS/Graphene	Phototransistor	-	420 A W^{-1}	2.1×10^9	12/198 ms	[147]
Organic/PbS	Phototransistor	400-1000	6.32 A W^{-1}	1.12×10^{13}	0.42/0.37 s	[148]
PbS NC (perovskite shells)	Photoconductor	850 - 1400	1.3 A W^{-1} (1100 nm)	2×10^{11}	3.6 / 30 ms 110 kHz	[149]
PbS NC (MPA)	Photoconductor	950 - 1650	70 / 15 A W^{-1} (1550 nm, 5 / 20 µm gap)	$10^{12}/5\times10^{12}$ $< 10^{11}$	1 / 15 µs	This work
PbS NC (TBAI)	Photoconductor	950 - 1650	0.3 / 0.1 A W^{-1} (1550 nm 5 / 20 µm gap)	$1.7\times10^9/5\times10^{10}$	2 / 16 µs	This work

NC = NanoCrystals, NP= NanoParticles, PBCM (conducting polymer), MWCNTs (Multi Well Carbon Nanotubes)

The lower responsivity measured in TBAI-treated photodevices at 1550 nm is a consequence of their larger dark current, as also reflected by their overall (white light illumination) lower photo-sensitivities (Table 2) as compared to MPA-treated photoconductors. The TBAI treatment of QD-solids can induce the introduction of one energetically dominant trap state level at 0.34 eV below the conduction band of PbS, as pointed out in recent publications.[135],[140] This mid-gap band level and similar ones for MPA treated photodevices, even if associated to different surface species as deduced from XPS measurements, could be responsible for the QD-solid conductivity when not completely populated (trap sensitized semiconductor),[141] i.e., under very low illumination intensities. Moreover, the effect of QD agglomeration and the expected strong electronic coupling in TBAI-treated PbS QD-solids, could also convert such trap state level into an energy band responsible of the higher dark current levels in comparison to MPA ones, as discussed above. Another consequence of this effect will be a higher noise signal influencing the minimum measurable photocurrent under very low illumination intensities (below 2-3 pW for 5 µm wide channel photoconductors).

As discussed above, photoconductors based on PbS QD-solids are characterized by very large responsivities or very high photoconductive gain, but only at extremely low incident optical powers. Moreover, the origin of such a high photoconductive gain has its origin in the presence of trap states for electrons (the minority carriers in the PbS QD-solid) close to the conduction band, i.e., centres that do not

emit/capture holes, as illustrated in Figure 48(d). From this model, by assuming the charge neutrality condition $\Delta p = \Delta n + n_t$, where Δn (Δp) and n_t are the excess photogenerated electron (hole) and occupied trap concentrations, respectively, the rate Equations for minority carriers and trap states are:[150]

$$\frac{d\Delta n}{dt} = g - \frac{d\Delta n}{\tau} + \frac{n_t}{\tau_e} - \frac{\Delta n}{\tau_c}\left(1 - \frac{n_t}{N_t}\right) \qquad 22$$

$$\frac{dn_t}{dt} = -\frac{n_t}{\tau_e} + \frac{\Delta n}{\tau_c}\left(1 - \frac{n_t}{N_t}\right) \qquad 23$$

where τ_c (τ_e) is the capture (emission) time of electrons by (from) the traps whose total concentration is N_t (and energy depth E_t). The Equations can readily be solved under steady-state conditions, $d\Delta n/dt = dn_t/dt = 0$, to obtain for Δn and n_t:

$$\Delta n = g\tau \qquad n_t = \frac{g\tau N_t}{g\tau + N_t\left(\frac{\tau_c}{\tau_e}\right)} \qquad 24$$

from which the photoconductivity results:

$$\Delta\sigma = q(\mu_n + \mu_p)\Delta n + q\mu_p n_t = q\mu_p\left[\left(1 + \frac{\mu_n}{\mu_p}\right) + \frac{N_t}{g\tau + N_t\left(\frac{\tau_c}{\tau_e}\right)}\right]g\tau \qquad 25$$

From eq. 25 we clearly obtain the limits: (i) $\Delta\sigma \approx q\mu_p\left(\frac{\tau_e}{\tau_c}\right)g\tau$ for very low carrier generation level, $g\tau \ll N_t\left(\frac{\tau_c}{\tau_e}\right)$, and (ii) $\Delta\sigma \approx q(\mu_n + \mu_p)g\tau$ for high carrier generation levels, $g\tau \gg N_t\left(\frac{\tau_c}{\tau_e}\right)$. Approximation (i) is leading to very high photoconductivity gain and responsivity, provided $\frac{\tau_e}{\tau_c} \gg 1$, i.e., very low (thermal) emission of electrons from trap states to the conduction band. On the opposite, approximation (ii) explains the saturation of photoconductor responsivity for high incident optical powers

i.e., where photocurrent turns to be proportional to the incident optical flux, the only regime for photodiodes.[108] The photocurrent and responsivity dependence with the incident optical power are nicely accounted for by eq. 25 (multiplied by the applied electric field and the photodevice surface and expressing g as a function of the absorbed optical power), whose best fits are shown by continuous lines in Figure 48(b)-(c) for MPA- (solid lines) and TBAI-treated (dotted lines) photoconductors. From these fits (the most representative is the one for the 5 μm channel photoconductor with MPA-treated) we obtain trap concentrations of ≈ 10^{11} cm^{-3}, $\tau_e/\tau_c \approx$ 2000-6000 and $\tau/\tau_d \approx 0.05$, where $\tau_d = L^2/\mu V$ (L the photoconductor channel length, μ= the effective carrier mobility and V the applied voltage) is the drift/transit time for minority carriers. If we use $\tau_d \approx$ 10 μs based on the mobility measurements reported in Table 3, the minority carrier lifetime would result ≈ 0.5 μs, which is not far from values measured in literature for colloidal PbS QDs and QD-solids.[151],[152] On the other hand, the ratio τ_e/τ_c should be due to the thermal exponential factor related to E_t, hence the energy depth of the trap level turns to be in the range 195-225 meV, consistent with values estimated for trap states in PbS QD-solids.[35],[135],[153],[140].

5.3.4 Transient Photocurrent Measurements

As aforementioned, the high responsivity regime of PbS QD-solid photoconductors is simultaneously accompanied by a slow operation speed of photoconductors due to the term $\left(\frac{\tau_e}{\tau_c}\right)\tau$ under very low incident optical powers. From our estimate, the expected response time $\left(\frac{\tau_e}{\tau_c}\right)\tau \approx 1 - 3$ ms, which is consistent with reported values under low optical excitation densities.[134],[154] On the contrary, when increasing the incident optical power, one would expect a decrease of the photodevice response time, by increasing the carrier generation level. Indeed, the transient photocurrent signals measured under relatively high power using a ns pulsed laser at 1064 nm, where free minority carriers dominate and responsivity tends to saturate, exhibit a decay with time constants in the order of some tens of μs, as shown in Figure 49, where the rise time is

practically negligible (<1 μs) within the time resolution of the oscilloscope used in the experiment. Particularly in the case of the MPA-treated photodetector, the photocurrent signal exhibits a main decay time of ~15 μs (Figure 49(a)) after a first fast decay <3 μs (the fit was made using these two decay times and a rise time <1 μs), which is also consistent with the effective recombination time of minority carriers measured under high incident optical power in solar cells based on PbS QD-solids after MPA ligand exchange.[134] In the case of TBAI-treated photoconductor there is only one dominant component with a time constant of ~16 μs (Figure 49 (b)) without the initial fast decay observed in the MPA-treated photodevice (the fit was made using this single decay and a rise time of ~2 μs). Both decay times, 15–16 μs, are not far from the drift/transit times expected in these QD-solids (Table 3) at the bias voltage used in the experiment (100 V), because it is carried out under high incident light power where most of the traps are filled. Under these conditions, it is also important to highlight that the response time of the photoconductors is faster than that obtained in Schottky-based photodiodes (both treated with MPA), where a value of ~135 μs was measured.[108]

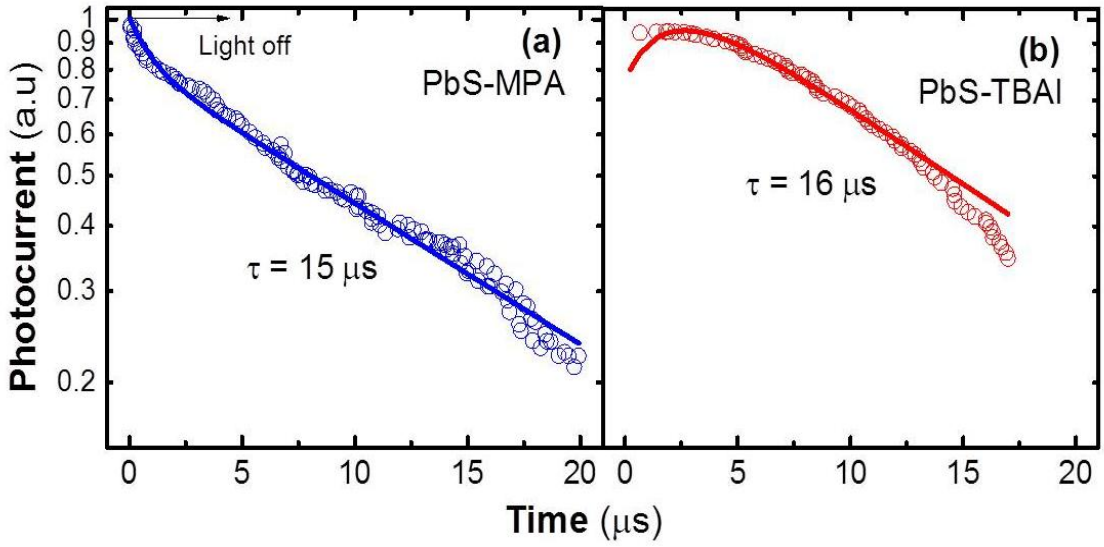

Figure 49: Transient photocurrent measurements for (**a**) MPA- and (**b**) TBAI-treated PbS QD-solid photoconductors with 5-mm channel length under pulsed laser excitation at 1064 nm.

The expression for calculating detectivity at a given light wavelength and bias voltage can be written as a function of the dark current in the photoconductor if shot noise dominates, as recently used in Reference [148] to estimate detectivity in organic/PbS bilayers.

$$D^* = R_\lambda \sqrt{\frac{S}{2qI_{dark}}} \qquad 26$$

Where R_λ is the responsivity at the wavelength of λ (1550 nm in our case), S is the effective area of the photoconductor $S = LxW$ (L and W the channel length and width, 2-5-20 µm and 1 mm, respectively), and q is the absolute value of electron charge. The best values for detectivity are found for MPA, as expected from previous discussions, concretely, ≈ 10^{12} Jones (I_{dark} (100 V) ≈ 1 µA) for the photoconductor with 5 µm of channel length and ≈ 5.10^{12} Jones for the case of the 20 µm one (I_{dark} (100 V) ≈ 6 nA), whereas it is below 10^{10} Jones for the 2 µm one, because of the smaller area and higher dark current (0.45 µA at 50 V). Again, D^* values at 1550 nm are among the best reported for photoconductor devices based on PbS QD-solids, particularly in those using MPA ligand exchange (see Table 4). For the corresponding photodevices using TBAI treatments we obtain ≈ $1.7x10^9$ and ≈ 5.10^{10} Jones, again because of the high dark currents for these photodevices (150 nA and 5.4 µA at 100 V for 5 and 20 µm wide channel lengths, respectively), as discussed above.

It is also important to highlight here that the high detectivities deduced in MPA-treated photodevices by eq. 26 only occur under very low incident light due to the presence of sensitizing trap centres for minority carriers, which produces a saturation of the photocurrent value very close to the noise current. Furthermore, it was reported recently that 1/f noise can be more important in PbS QD photoconductors than shot noise [48,49]. For this reason, it can be more accurate the use of the more general expression for estimating D^* given in Chapter 2:

$$D^* = \frac{\sqrt{S\Delta f}}{NEP} \qquad 27$$

where *NE*P is the noise equivalent power that can be estimated experimentally from photocurrent as a function of incident power to the value of the also measurable noise current, which in our case is ≈ 10 pA within a bandwidth of 1.6 Hz in the photodevice with 5 μm of channel length, very close to the smallest measured photocurrent value at the lowest incident power (100 fW) that would imply D* > 10^{11} Jones. However, this experimental determination of NEP is not exempt from inaccuracy due to the saturation effect of photocurrent in the low incident power range in PbS QD-solid photoconductors (MPA-treated ones, mainly), as discussed above. This is not the case for the other photoconductors where trap sensitization is not effective over noise (trap-level densities $<10^{11}$ cm^{-3}), which also occurs in photodiodes where short-circuit current always varies linearly with incident power [108]

A final question to be considered for photoconductors, including those based on PbS QD-solids, is the high bias voltages (20–100 V, depending on the channel length) used to get large responsivities. The solution to this issue is the use of interdigitated photoconductor devices, because smaller bias voltages are needed in a factor approximately equal to the number of metal finger pairs, for which promising results have reported in literature (see also Table 4).[143],[142],[155]

We have also fabricated some previous generations of interdigitated photoconductors (Figure 50(a)) using the doctor blading deposition and MPA ligand exchange for the formation PbS QD-solid over them. Figure 50(b) shows the photocurrent as a function of the applied bias recorded under solar-AM1 illumination (i.e., an incident density power of 100 mW/cm^2 that gives different collected light in the three devices because of their different active area: 200 and 20–10 μW in the 20 μm - interdigitated and 20–10 μm gap photoconductors, respectively). As expected, the photocurrent measured in the interdigitated photoconductor at 10 V is similar (smaller) to that measured at 100 V in the 20 (10) μm gap photoconductor. The measured responsivity obtained in the interdigitated photodetector decreases with incident power (Figure 50(c)), as previously observed and discussed for two-electrode photoconductors (Figure 48(c)). The absolute value of responsivity in this interdigitated device, 7 mA/W at 10 V, is not far

from the value reported in Reference[143] for the same finger gap (40 mA/W at 1V, but their interdigitated device has 5 times more finger pairs).

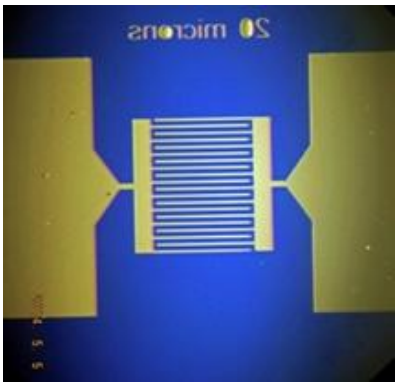

(a)

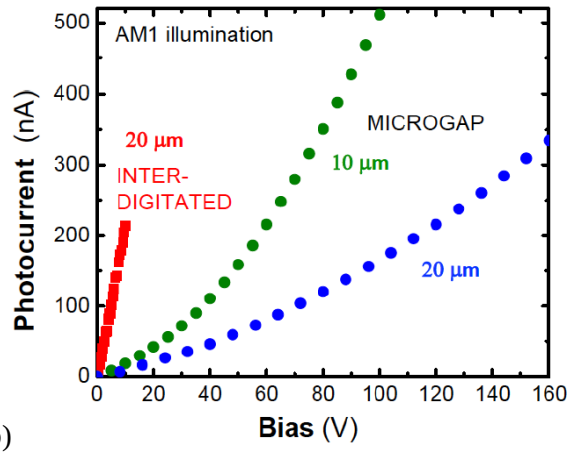

(b)

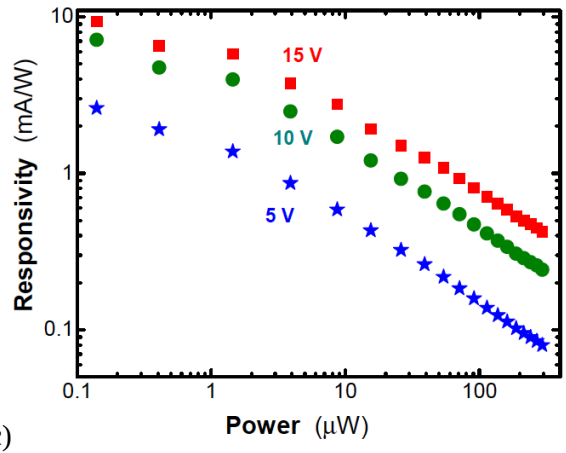

(c)

Figure 50: (a) Microscope photography of a 20 µm gap interdigitated device prior to the PbS QD nanoink deposition. (b) Photocurrent measured in the interdigitated device (red symbols) as compared to 10 (green symbols) and 20 (blue symbols) µm gap two-electrode photoconductors as a function of applied bias under AM1-solar illumination. (c) Responsivity in the interdigitated photoconductor device at several applied bias as a function of the incident power using a 1550 nm laser source (the responsivity is estimated by assuming that the whole laser beam is collected by the device).

However, the responsivity value reached in the preliminary generations of interdigitated photoconductor devices cannot be compared with the new generation of optimized two-electrode-gap photoconductors whose results were presented above, for which the doctor-blade deposition and thickness have been

optimized. In interdigitated photoconductors, our doctor-blade technique produces more inhomogeneous PbS QD-solid films over the interdigitated area, and further optimization (or a different deposition technique, as the one used in Reference [142]) is needed to develop efficient photodetectors operating at low voltages in the future.

Chapter 6 Infrared PbS CQDs Solution-Processed Schottky Photodiode

In the present chapter we show as proof of concept a PbS QD-solid Schottky-heterostructure photodiode operating in the third window of telecom wavelengths. We select a Schottky architecture for our photodiode to exploit the potential barrier formed between the nanocrystal film and a metal contact. In fact, large built-in potential at the metallurgical junction could led to the desired combination of sensitivity and speed.

Concordantly with the findings presented in Chapter 5, we have achieved the most performing Schottky photodiodes approaching the PbS nanoink deposition by doctor blading technique end processing the obtained QD-solid by MPA ligand exchange. We followed this path towards the achievement of high sensitivity and detectivity values by reducing dark currents and noise signals.

The chapter opens with the overview of the key parameter underlying QD-based Schottky photodiodes for efficient sensing applications. The device architecture and its parameter optimization study are then discussed.

The optoelectronic characterization of the photodiodes showed, despite the relatively simple device architecture, a maximum responsivity (R) of 0.27 A/W corresponding to an internal quantum efficiency (IQE) higher than 30% at 1500 nm, a detectivity $D^* \approx 10^{11}$ Jones and a response time $\tau \approx 135$ μs.

6.1 Schottky Photodiodes

Semiconductor-based photodetectors works under the basic mechanism of the generation of electron-hole pairs under light exposure and their collection through conductive electrodes, being one of them transparent (e.g., a transparent conductive oxide). The semiconductor will constitute the photoactive component of the device, because its band-gap energy defines the longest light wavelength achievable for photodetection. For an intrinsic semiconductor, the absorption of a photon of energy equal (or higher) to its band-gap allows an electron to be promoted from the valence band to the conduction band thus leaving holes in the valence band. In the case of a photodiode (in the most common cases constituted by a p-n, p–i–n or a Schottky junction), the photogenerated electron-hole pair under the influence of the intrinsic electric filed of the depletion region, are swept to the electrodes giving rise to a photocurrent. If we consider the formation of excitons upon the electron-hole pair generation it would be dissociated by such electric field. Such devices are usually compact, does not need the application of a (negative) bias voltage, exhibit fast response and typically is characterized by a high quantum efficiency (one electron hole pair is generated per incident photon and non-radiative recombination times of minority carriers are longer than their lifetimes). In particular, Schottky photodiodes are potentially faster than p-n photodiodes, with large bandwidths and low levels of internal noise, but suffer of low responsivities.

Initially, thin strained layers of GaAs and AlGaAs were used to create a high built-in potential in forming heterostructures with InGaAs (semiconductor-semiconductor photodiode) but high leakage currents and low gains were observed due to a significant trap density.[156] Later, thin layers of intrinsic InAlAs were used for barrier enhancement, which improved the device performance due to the lattice matching between InAlAs and the InP substrate.[157],[158] Recently, with flip-chip bonding of InGaAs Schottky diode on a Si substrate, responsivities as high as 0.74 A/W at 1550 nm and 1 μA of dark currents under low applied bias (~1 V) has been achieved.[159]

In the past, important limitations accompanied the development of photodetector devices based on conventional single-crystalline semiconductors, because of production high costs, material

incompatibilities, and the necessity of highly customized deposition systems, even if most of them have been overcome for Si and InGaAs photodetectors, may be except the higher cost of the latter.

With this purpose the approach to CQDs for realization of solution-processable photodetectors has offered a field for the development of optoelectronic devices with low costs production and the applicability over light weight, large area and flexible platforms in a wide range of wavelengths.[40],[127],[160]

In the last years, among all the candidate materials, PbS QDs have emerged as the most promising for fabricating infrared photodetectors and solar cells.[128],[139] PbS QD-solid-based Schottky photodiodes have been proven as a suitable solution towards the achievement of simultaneously high speed and sensitivity, important characteristic for applications requiring high modulation frequencies such as, high-speed process monitoring and optical communications.[7][6]

Other low-dimensional materials systems as transition metal dichalcogenides (TMDC) and some semiconductor nanowires (ZnO, GaAs, Si, …) have also demonstrated good photodetection capabilities and bandgap tuning in some cases. However, most of TMDCs and nanowires generally possess wide bandgap energies > 1 eV,[161],[162] hence they are not suitable for telecommunication applications, whereas CQDs can absorb photons from visible to mid-infrared region owing to its size-dependent band gap for certain base materials (PbS, PbSe, PbTe, HgTe,…).[163] The responsivity of the QD photoconductor can achieve 2700 A/W from visible to 1300 nm.[10] However, the bandwidth of these photoconductors is quite small and the dark current is relatively high. The QD-solid-based Schottky photodiode has proven to fulfil the requirement of telecommunication applications, with high sensitivity and response speed.[7] In the next sections the most important results we have obtained fallowing this architecture will be discussed.[95],[30]

6.1.1 Architecture of the fabricated devices

For the fabrication of Schottky diodes with PbS CQDs as photoactive material (Figure 51 left) we have chosen commercial ITO-coated glass substrates of 10 cm^2 whose resistivity is in the order of 10 Ω.sq. These substrates were cleaned prior to film deposition by rinsing with isopropanol and water, then dried with N_2 flow. Once dried, a PEDOT:PSS film is deposited onto the substrate by doctor blading method and

subsequently beaked for 5 min at 100°C to improve the film adhesion. The photoactive film of PbS CQDs is deposited onto the PEDOT:PSS film by doctor blading method following the procedure reported in Chapter 4. The device is then completed with 100 nm thick Ag metal contacts deposited by PVD at a rate below 1 nm/s. A shadow mask was used to define a 4 x 9 array of 1 mm side square contacts. Even though the QD-solid shows great long-term stability, as deduced from the XPS analysis in Chapter 4, the device was encapsulated with a silicone-based film to avoid the oxidation of the Ag electrode in the case of optimized photodiode generation where a complete electro-optical characterization was made thanks to the stability and durability achieved by the encapsulation.

Due to the vertical configuration of the Schottky-photodiode the incident light has to travel through the glass/ITO substrate and the PEDOT:PSS film to finally reach the QDs-solid. Here the generated electron and holes are respectively collected at the Ag and ITO contacts (Figure 51 right). The PEDOT:PSS layer contribute to reduce the dark current, thanks to its blocking role for electrons other than promoting a smoothing effect between the ITO and the QD-solid.

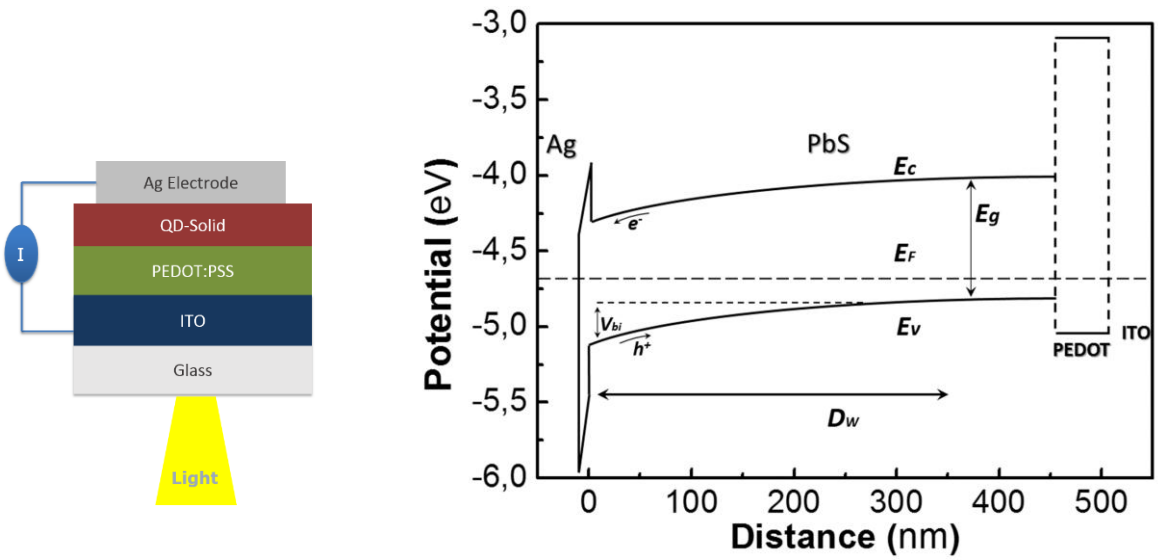

Figure 51: Structure scheme (left) and energy band profile (right) of the Schottky-heterostructure ITO/PEDOT/QD-solid/Ag.

6.1.2 Influence of the PbS-QD film deposition on the photodiode performance

The production of QD-solids has been initially approached by spin coating and doctor blading technique to evaluate the most promising one by device performances comparisons. In Figure 52 the results of the I-V characteristics under dark and under monochromatic light exposition of λ = 810/820 nm for two QD-based Schottky photodiodes, one prepared by spin coating (Figure 52a) and by doctor blading coating technique (Figure 52b). Both samples underwent the same MPA ligand exchange treatment. In the graphs, firstly, is evident a big increase by more than a factor ten in the open circuit voltage (V_{OC}). This difference in V_{OC} is attributable to the smoother film surface obtained with doctor blading technique with a sensible reduction of the film granularity. A smoother surface brings to a significant reduction of the series resistance that deteriorate the V_{oc} performances of the device.

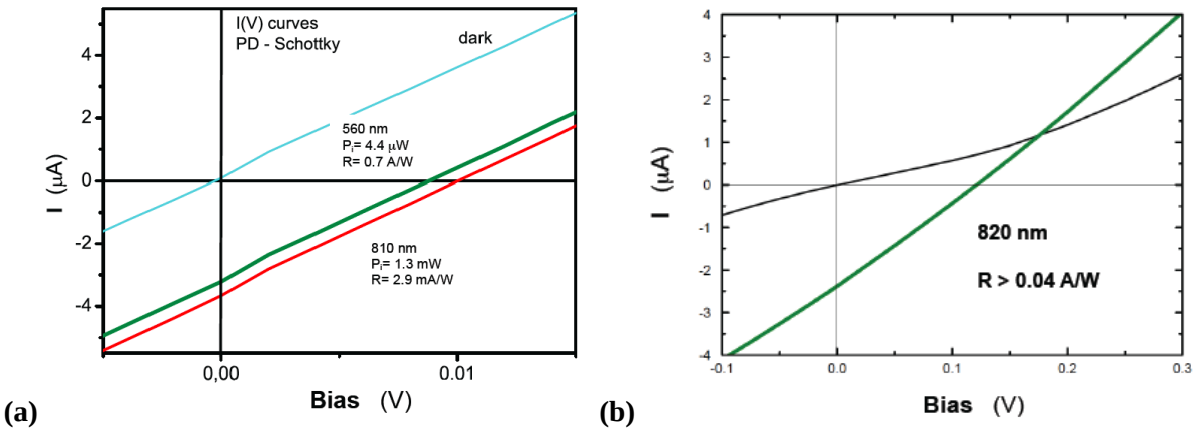

Figure 52: Comparison of the I-V characteristics of the Schottky photodiodes with PbS QD-solids deposited by spin coating (a) and doctor blading (b). The QD-solid thickness is in both devices is around 360 nm.

A similar photocurrent was measured in both devices, but this is due to the use of a different light source power in the two measurements. In fact, the responsivity of the doctor blading processed device which is enhanced by a factor ten (R>0.04 A/W) compared to that of the device produced by spin coating (R≈ 2.9 mA/W). In a first period of the present thesis this was the best responsivity value measured at wavelengths close to the exciton resonance in Schottky heterostructure photodiodes fabricated with spin-coated films of

PbS CQDs, as shown in Figure 53. The responsivity of these photodiodes was much higher at wavelengths shorter than that of the ground-exciton absorption resonance for these CQDs (in the range 1-1.1 μm, see Figure 53), but our objective was to obtain such high values at the exciton wavelengths, which was the reason to change the deposition method for the formation of the QD-solid, from spin coating to doctor blading (see Chapter 4).

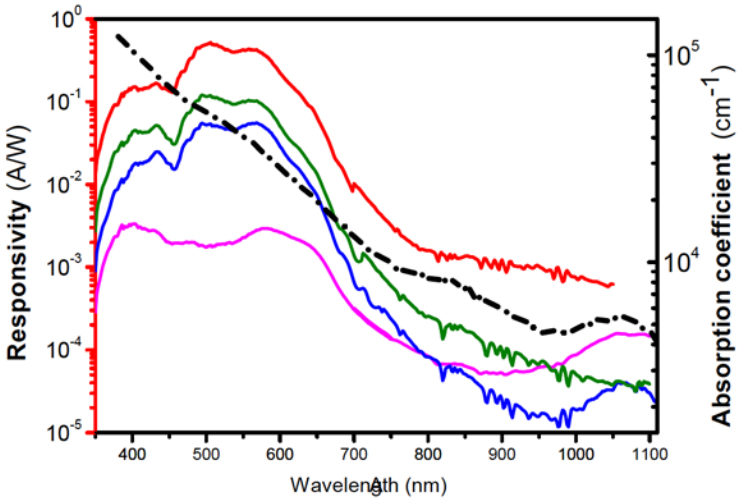

Figure 53: Responsivity curves (colour continuous lines) measured for different photodiodes fabricated by spin coating the CQD film and its average absorption coefficient spectrum (black discontinuous line).

6.1.3 Optimization of Near-Infrared PbS-CQD Photodiodes

The focus towards the improvement of Schottky photodiodes has been put on the principle operating characteristics that a photodetector for high speed telecommunication must possess: high sensitivity, which is possible by reaching a low noise current, and high response speed.

In a semiconductor photodiode the operating principle consist on the separation and collection of the photogenerated electrons and holes by the built-in electric field. Considering a Schottky-barrier type photodiode formed between the nanocrystal film (PbS CQDs) and the metal (Ag), we expect an efficient carrier transport and the formation of a sufficiently large built-in potential in order to lead to the desired

combination of sensitivity and response speed.[87] So, it is mandatory to define at first the best structural parameters to facilitate the transit of charge carriers throughout the device and their collection at the electrodes. Subsequently, the focus must be put on the QD-solid optimization for the best performances of generation and recombination of the charge carriers, from the point of view of both the QD synthesis (Chapter 3) and film deposition/formation (Chapter 4), other than the influence of the photoactive layer thickness (see below).

As discussed in Chapter 5, the charge transport in the QD-solid take place by ligand-assisted NC-to-NC tunnelling (hopping) and it is therefore strongly dependent on the NC separation, which is governed by the length of capping ligands. The long length of oleic ligands (~2.5 nm) therefore acts as a tunnelling barrier and results in weak coupling between individual NCs, as the wavefunction of charge carriers in each NC will remain effectively localized within it. The charge transport, under both dark and light conditions, for oleic-capped PbS QD films is mostly suppressed.[17] To overcome this limitation, films based on CQDs capped with insulating ligands have to be chemically treated to replace oleic ligands with shorter ligands. The reduced interparticle distance favour the coupling of charge-carrier wavefunctions between NCs thus increasing the charge-carrier tunnelling rate.[164]

Anyway, the decrease of the inter-nanoparticles spacing in the QD-solid has not to be excessive, in fact it may cause a loss of the properties related to the quantum confinement and also increase noise signals in the device.[108] The noise performances of Schottky diodes is mainly determined by the shunt resistance,[165] which can be correlated to the barrier at the metal semiconductor junction. Given that the Schottky diode thanks to the metallurgical junction with a large built-in potential, is prone to shows low noise signals, once obtained the desired charge-carrier coupling in the QD-solid, the main challenge would be represented by the achievement of high photoresponse.[68]

In semiconductor materials, free-carrier lifetime is modified by the presence of surface states. In PbS QD-solid surface states are most likely due to oxidation species, principally lead sulphates ($PbSO_3$).[154] $PbSO_3$ act in this context as p-type dopants that makes of the PbS film a p-type semiconducting with the formation of a built-in potential at the metal-semiconductor interface.[6] Related to the built-in potential is the carriers transport mechanism of and separation efficiency at the electrodes.[166] Nevertheless oxides

species, acting as p-doping species of PbS CQDs, also are acting as intrinsic trapping centres for electrons that would cause the increase of the carrier lifetime limiting the temporal response of the photodiode.[6] Therefore, the concentration of $PbSO_3$ has to be monitored as a function of the device performance in order to find the best relation between photo-conversion and bandwidth.[30]

An important improvement related to the carrier mobility on QD-solid is attributable to the use of methanol as MPA solvent in the ligand exchange procedure. Methanol is a strong non-solvent for the nanoparticles, which, due to the high polarity, we also use to remove the excess of organic ligand from their surface during a short dipping and rinsing of the QD-solids. This procedure is identified under the name of crystal necking.[10]

As shown by XPS analysis in Chapter 4, MPA through its thiol group, chemically reduces the surface of PbS nanocrystals by removing oxides species, especially $PbSO_3$, that are known to act as p-type dopant.[167] This reduction suppresses the effective p-type doping of the QD-solid semiconductor and thus it would lead to a decrease of the built-in potential of the Schottky barrier from which the diode behaviour originates.[132] At the final stage, the re-oxidation of the nanocrystal film was performed to restore the degree of effective doping necessary to create a Schottky barriers with large built-in potential.[168] Therefore, we can sum up the post-ligand exchange optimization treatment of the PbS QD-solids, as a necking then oxidation procedure.

The last step we face towards an improved efficiency and response speed of the photodiode, is the optimization of PbS QD-solid thickness in order to have carriers transport due only to the balance between carrier generation, recombination and drift-diffusion mechanisms. In a fully depleted Schottky diode all photogenerated electrons and holes are sweep directly to the contacts by the electric field due to the built-in potential of the junction (Figure 51). For this reason, we have adjusted the NCs film layer thickness to be similar to the thickness of the depleted layer (value that we have estimated from C-V characterization of our diodes, see next section), so that only the faster contribution to the transient current is involved and the path among electrodes that carriers have to cross is minimized.

The first and second series of PbS QD-solid-based photodiodes for working at the near-infrared spectral range were produced by the doctor blading deposition technique, given the better performance when

compared to spin coating (section 6.1.2). In Figure 54 we report the measured responsivities in these photodiodes whose maximum values were around 0.1 A/W at ≈1200 nm (Figure 54a) and 0.16 at ≈1600 nm. In the first-generation photodiodes (Figure 54a) both the photoresponse and absorbance exhibit structureless spectra, may be due to the formation of QD agglomerates without surface ligands separating them, which can be also the origin of a smaller responsivity value in the near-infrared region as compared to the second generation photodiodes (Figure 54b). In this case, the absorbance and responsivity spectra show a clear resonance at around 1600 nm, where the ground exciton optical transition is expected for the PbS-QD-solid, as observed from typical absorbance and photoluminescence spectra of the colloid in Figure 55, even if a red shift of the optical transitions is expected in the PbS-QD-solid due to the electronic coupling between QDs after the ligand exchange.

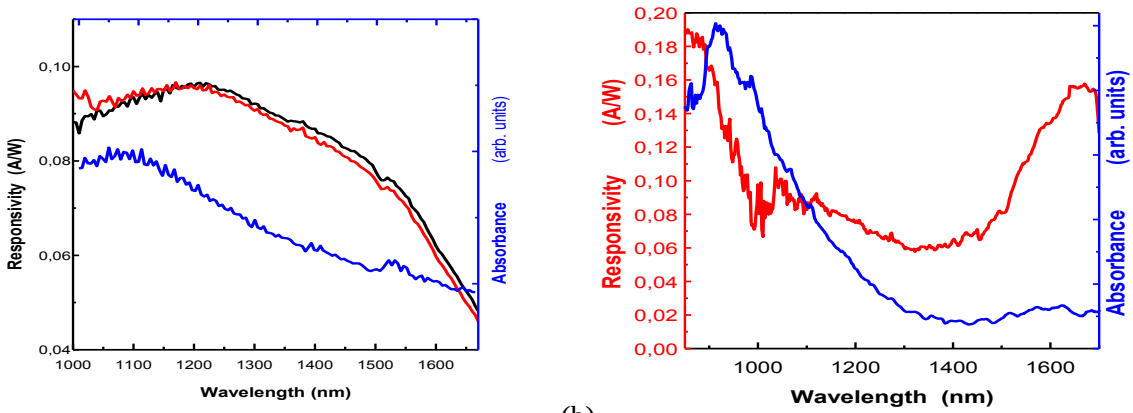

(a) (b)

Figure 54: Responsivity spectra for the first (a) and second (b) generations of glass/ITO/PEDOT/QD film/Ag photodiodes (black and red curves in a and red curve in b) where the QD films (300 and 500 nm for a and b) were prepared by doctor blading; the corresponding absorbance spectra of these films are depicted by blue continuous line curves.

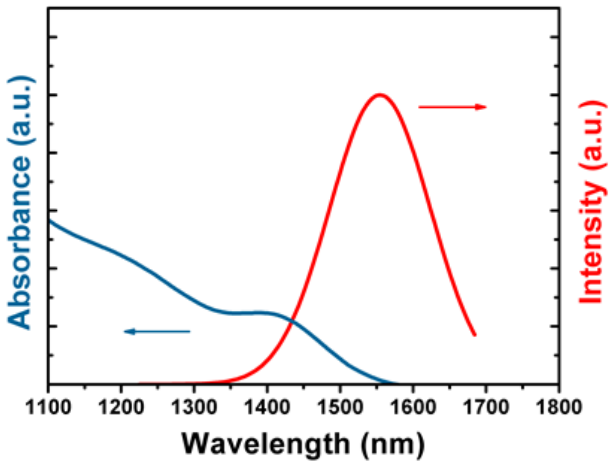

Figure 55: Absorption (blue curve) and PL spectra (red curve) of oleylamine-capped PbS CQDs dispersed in octane.

We have also tested the influence of the PbS-CQD film thickness on the electro-optical performance of the photodiode. Figure 56 shows the responsivity spectra of Schottky photodiodes based on 500 and 250 nm thick PbS-CQD thin solid films, whose peak values are measured to be 0.48 and 0.15 A/W at around 1300 and 1550 nm, respectively, even though if the ground state exciton absorption was outside our spectrometer range, *i.e.*, beyond 1650 nm. The fact that the observed responsivity peak is observed at shorter wavelengths than those of the exciton peak is attributed to the different QD-solids thicknesses which give rise to different reflectance values in the examined wavelength region.

The time response of these photodiodes working in photocurrent mode is estimated to be around 100 μs, very similar to those reported in literature.[154] The measured photovoltage noise signal is around 85 $nV/Hz^{1/2}$ at 1 kHz for the 500 nm thick QD-solid-based photodiode, whereas the photocurrent is perfectly linear over more than three orders of magnitude (constant responsivity), with an estimated detectivity around 10^{11} Jones. These photodiodes have exhibited a stable behaviour in air (no encapsulation was made) during a maximum two weeks; in fact, their electrical parameters degrade progressively and after one month in air the responsivity decreased by a factor two, approximately. Finally, it is also worth noting that these photodiodes, even if they were not fabricated with an optimized architecture to be used as a solar cell, when illuminated under AM1 solar simulator produce open circuit voltages (V_{oc}) greater than

300 mV and short circuit currents (J_{cc}) in the range of 8-16 A/cm^2. These results are comparable to recently published values for PbS QD films in solar cell structures.[165],[6] These results would correspond to solar cell efficiencies of around 1% due to the low fill factor of this simple Schottky architecture. In fact, this degradation of the I-V curve is even observed under monochromatic and low power excitations conditions at telecom wavelengths, as shown in Figure 56b, which is attributed to a sharp decrease of the diode shunt resistance following the increased hole leakage towards the Ag contact.

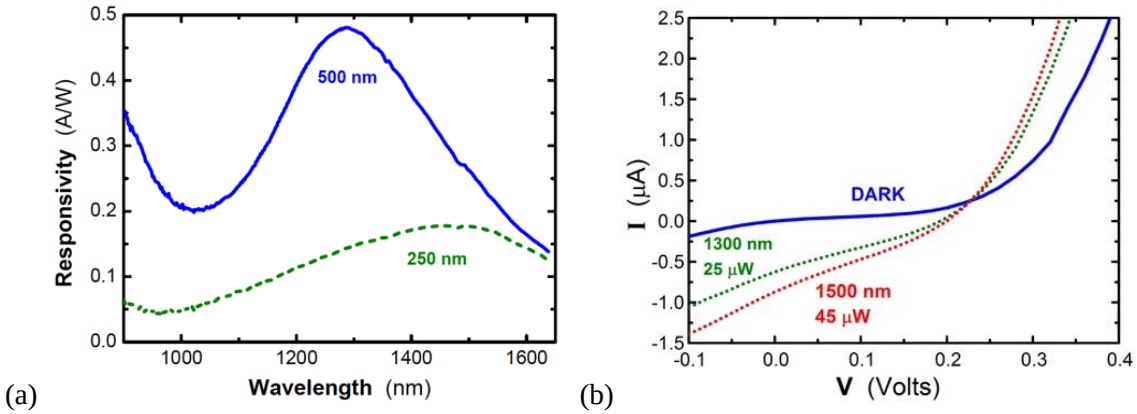

(a) (b)

Figure 56: (a) Responsivity spectra of Schottky photodiodes fabricated with 500 nm (continuous blue line) and 250 nm (dashed green line) thick PbS-QD films; (b) I-V curves under dark and monochromatic excitation at 1300 and 1500 nm (the power indicated in both cases are measured by an InGaAs power meter.

6.2 Optoelectronic Characteristics

6.2.1 Capacitance Voltage Measurements

It is worth to mention that electro-optical characterization was not exhaustive in previous photodiode generations given the negative evolution of the devices, which was the reason to encapsulate them after the wire soldering to the silver electrodes. The PbS-CQD film in this last generation of photodiodes was around 450 nm, a thickness for which we obtained the best performance in photodiodes, as shown in previous section. We carried out Capacitance–Voltage measurements of the Schottky photodiode in the range from -0.3 to 0.2 V while recording the capacitance values at a frequency of 8 kHz, whose typical dependence is shown in Figure 57. By varying the bias voltage applied to the junction it is possible to vary the width of the depletion zone that is the basis of the capacitor behaviour in a semiconductor diode.[128] The dependence of the depletion width on the applied voltage, by Mott-Schottky analysis, provides information on the QD-solid characteristics, such as the acceptor concentration N_a, its corresponding width of the depletion region w and the built in potential V_{bi} at the junction. Here the relation we have applied to describe the depletion region formed in the semiconductor[139] (abrupt doping approximation):

$$C^{-2} = \frac{2}{A^2 q \varepsilon N_a}(V_{bi} - V) \qquad 28$$

$$w = \sqrt{\frac{2\varepsilon(V_{ib} - V)}{qN_a}} \qquad 29$$

Where V is the applied bias, A is the device area, q is the elementary charge and ε is the dielectric constant of the semiconductor that we set as $\varepsilon = 15\varepsilon_0$.[169]

The C^{-2}(V) data (open symbols in Figure 57) were measured at a frequency of 8 kHz, just in the region where C(ω) is approximately constant (Figure 58). In this region the QD-solid the doping density can be considered constant as at reverse bias voltages the slope change of the C(ω) curve reflects the presence of deep traps states that are not fully occupied.[170],[171] In Figure 57 C^{-2}(V) it exhibits a linear behaviour

around 0 V whose fitting thru eq. 28 (continuous line in Figure 57) yields a built-in potential $V_{bi} \approx 0.16$ V, an acceptor concentration $N_a \approx 1.9\times10^{15}$ cm^{-3} near the Schottky barrier and a depletion zone width $w \approx 374$ nm estimated using eq. 29.

The latter value, as compared to the thickness of the PbS QD film (≈450 nm) indicates that the active layer is mostly depleted. By using this acceptor concentration and the independently measured resistivity in doctor blading films, $\rho \approx 10^5$ Ω cm, a mobility of 0.033 cm^2 V^{-1} s^{-1} is deduced, which is consistent with values reported in literature. [30]

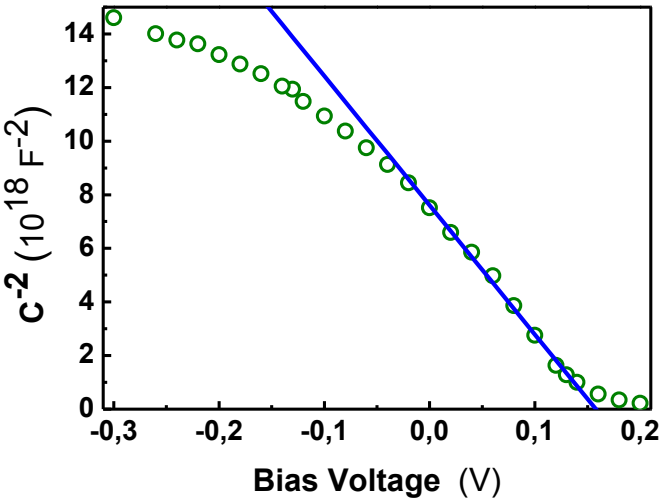

Figure 57: C–V characteristics recorded at a frequency of 8 kHz.

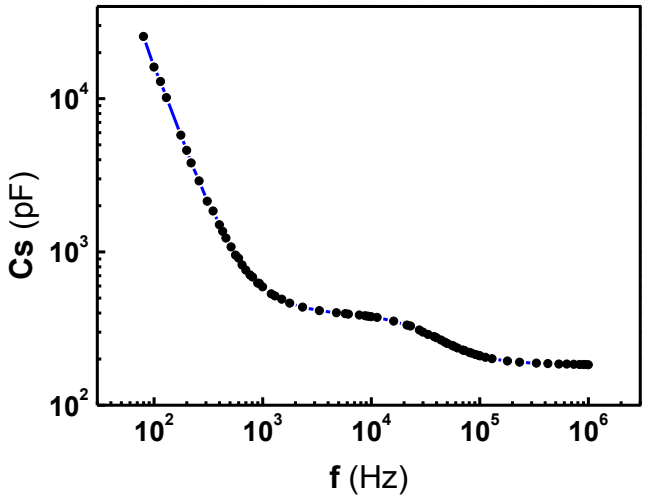

Figure 58: Capacitance as a function of the probe signal frequency measured at 0 V using a LCR meter.

6.2.2 Current Voltage Measurements

The I–V characteristic of our device under dark conditions (red open symbols in Figure 59) yields a dark current of only 35 nA (3.5 mA/cm^2) at V = −0.05 V, whereas exhibits a photoresponse as high as 286 nA at the same bias under a monochromatic light exposition of 2 mW at λ = 1550 nm (blue open symbols in Figure 59). That means a photocurrent over dark current ratio of around a factor ten. This demonstrates the high sensitivity of our photodetector if compared with recent reports.[87] I–V curves were fitted (continuous lines in Figure 59) using the ideal diode Equation (I_{ph} = 0 under dark conditions):

$$I = I_0\left(e^{\frac{qV}{nk_BT}} - 1\right) - I_{ph} \qquad 30$$

Where V is the applied bias voltage, q the elementary charge, k_B the Boltzmann constant, T the temperature (300 K), n the ideality factor, I_0 and I_{ph} the saturation and short-circuit current intensities, respectively. It is worth noting that we tested the fitting with a real diode expression that is, taking into account series and shunt resistances. However, the best fit in the examined voltage range was obtained with the ideal diode Equation (eq. 30), considering the negligible series resistance and the practically infinite shunt resistance, with a saturation current density of 6.8 μA/cm^2. This value is lower than that extracted

from the curve recorded under illumination (9.6 μ/Acm^2), as was noted for I-V curves in previous devices (Figure 56b). The ideality factor resulted to be 3.2 for both curves, which is representative of a generation–recombination carrier transport mechanism limited by deep traps present in the active layer, as it is the case of the PbS QD-solid.

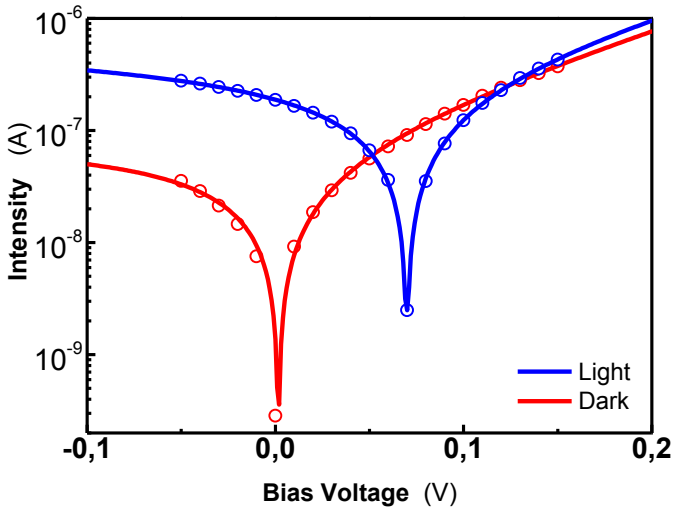

Figure 59: I–V characteristics of the device in dark conditions and under illumination with 2 mW at 1550 nm.

Continuous curves stand for the best fit to the ideal Schottky diode Equation. The noise equivalent power (NEP), as we have introduced in Chapter 2, is defined as the optical power at which the signal-to-noise ratio is equal to 1, which was estimated to be around 2 pW.[108] The NEP value has been graphically extrapolated to the noise level baseline from the linear response of the measured photocurrent at the peak responsivity wavelength as a function of the incident power (Figure 60). The NEP normalized to the electrical bandwidth and to the photo-sensitive area of the photodetector is the detectivity, which results D*≈ 10^{11} jones, comparable to the most efficient photodevices reported in literature.[87],[39],[30] Such high sensitivity is what we aimed to achieve at zero-bias with the QD-solid-based Schottky photodiode since only thermal noise can be generated under this condition.

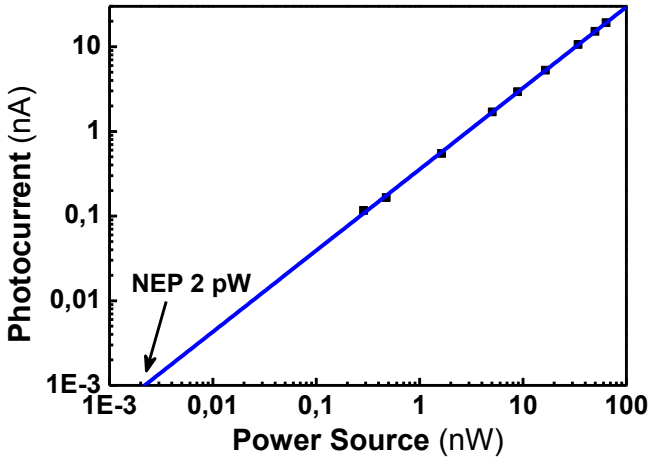

Figure 60: NEP extrapolation from the photocurrent measured as a function of the incident optical power at 1550 nm.

6.2.3 Responsivity and External Quantum Efficiency

The Responsivity and External Quantum Efficiency of our photodiode without external bias voltage (i.e., from the direct measure of the short circuit current using a lock-in amplifier under modulated monochromatic light, as described in Chapter 2). A peak value of R ≈ 0.27 A/W was measured at ≈1460 nm that corresponds to an EQE of 22% (Figure 61). The photocurrent spectrum was measured for various photodiodes in the same sample with comparable results as a proof of the fabrication reproducibility. The recorded photocurrent spectrum follows quite well the absorption spectrum of the QD-solid in the wavelength range from ~1.6 μm to 0.9 μm. We monitored the responsivity along 120 days since the device fabrication (Figure 62). As we let the device aging under standard ambient temperature and pressure (SATP) conditions during this period of time, the evident raise in Responsivity is attributable to the increase in the concentration of PbS sensitizing centres. After 90 days the peak responsivity at ≈1500 nm reaches its maximum value of around 0.27 A/W, which is maintained for further 30 days, as shown in Figure 62. After 120 days under SATP the concentration of mid-bandgap states would dominate over the p-doping and the subsequent decrease of the barrier height of the Schottky contact cause the deterioration of the photodiode and its responsivity together with an increase of the response time. These results are among the best reported in literature for a similar device architecture and wavelength range.[87],[6],[39]

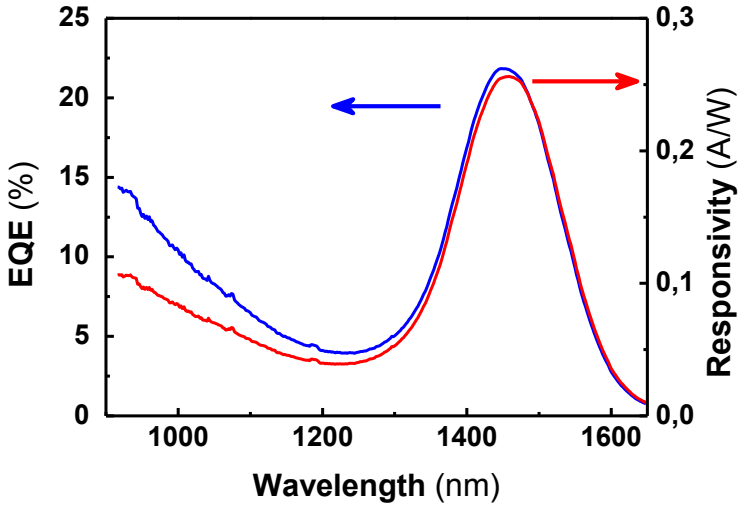

Figure 61: External Quantum Efficiency (blue line) and Responsivity (red line) of the Schottky photodetector as a function of the light source wavelength.

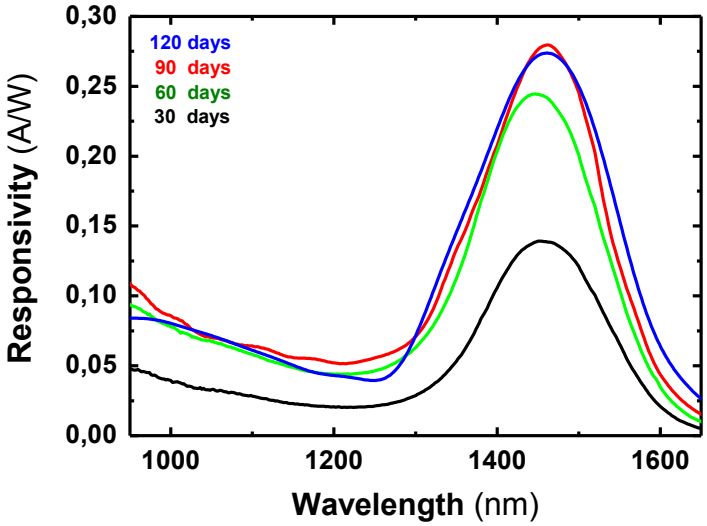

Figure 62: Responsivity as a function of the light source wavelength after 30, 60, 90 and 120 days since the device fabrication.

6.2.4 Absorbance and Internal Quantum Efficiency

The separation from EQE of the reflectance at the QD-solid interfaces with PEDOT and Ag leads to the internal quantum efficiency (IQE), which only takes into account the photogeneration of photons inside the active layer and the carrier recombination/trapping kinetics. Figure 63 shows the wavelength dependence of

IQE (red line), deduced from the relationship $IQE=EQE/T^2$, where the square of the transmission coefficient T of the QD-layer (once corrected by the substrate transmittance) is incorporated to consider the reflectivity at the PbS–Ag interface, i.e. the double path of light being absorbed at the QD-solid film. The IQE is more important for the ground excitonic absorption band as compared to shorter wavelengths, because the double path of light is less significant in this case. Therefore, the absorbed light increases notably at wavelengths shorter than that of the peak excitonic absorption, as shown in Figure 63 (blue line). The double path of light is also responsible of the observed shift (≈40 nm) between the excitonic-resonance peak wavelengths in IQE and absorbance spectra. The maximum value of IQE (at ≈1430 nm) is around 40% and represents a very good value among other reported in literature for a QD-based photodetector at telecom wavelengths.[39]

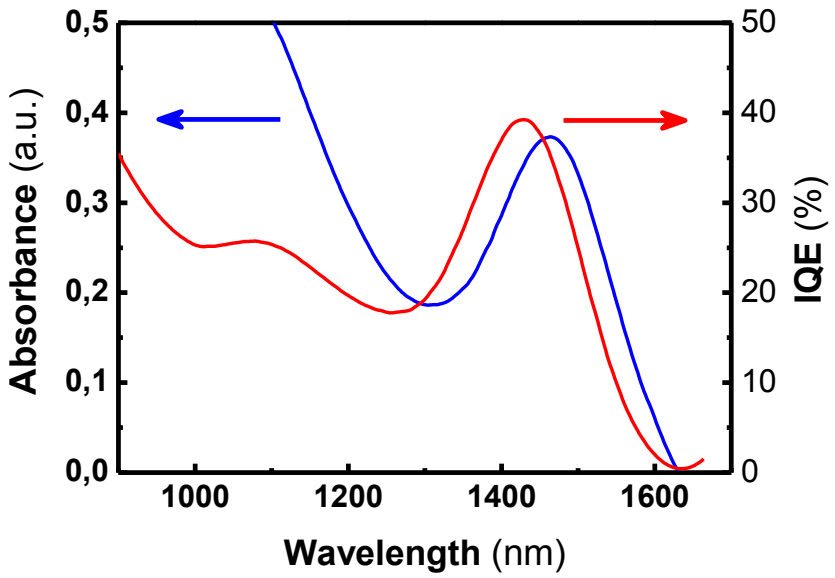

Figure 63: Absorbance (blue line) and Internal Quantum Efficiency (red line) of the Photodiode as a function of the light source wavelength.

6.2.5 Temporal Response Studies

To characterize the temporal response of charge carriers in our photodetector we have used a square-shape modulated photocurrent measurements (chopper frequency of 780 Hz) under monochromatic light of

λ =1550 nm. The transient photocurrent was recorded using a fast oscilloscope, in Figure 64 several periods are recorded.

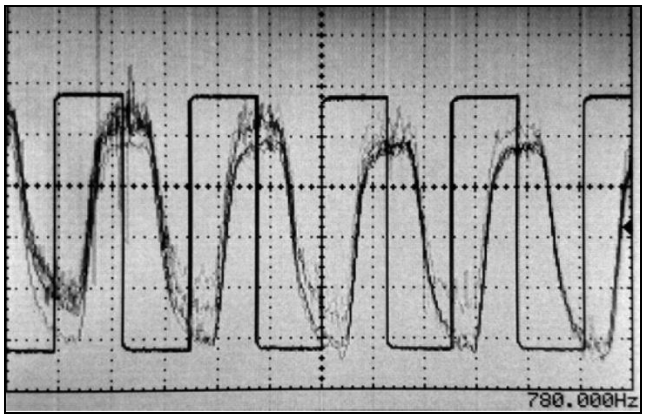

Figure 64: Photocurrent transient response measured under chopped light at 780 Hz.

After light-on or light-off conditions, the steady state is reached under exponential dependences following the respective equation:

$$I_0 = (1 - exp(-t/\tau)) \;\; ; \;\; I_0 = (1 - exp(-t/\tau)) \qquad 31$$

We take then into study one period of the transient current (Figure 65), after fitting with eq. 31 (continuous lines) to the experimental curve (data symbols) we can estimate a time constant τ ≈135 μs. This temporal response is comparable to similar devices in literature[87] and it mainly corresponds to minority carriers photogenerated in the depletion zone of the PbS QD-solid drifting to the metal contact (Figure 51).

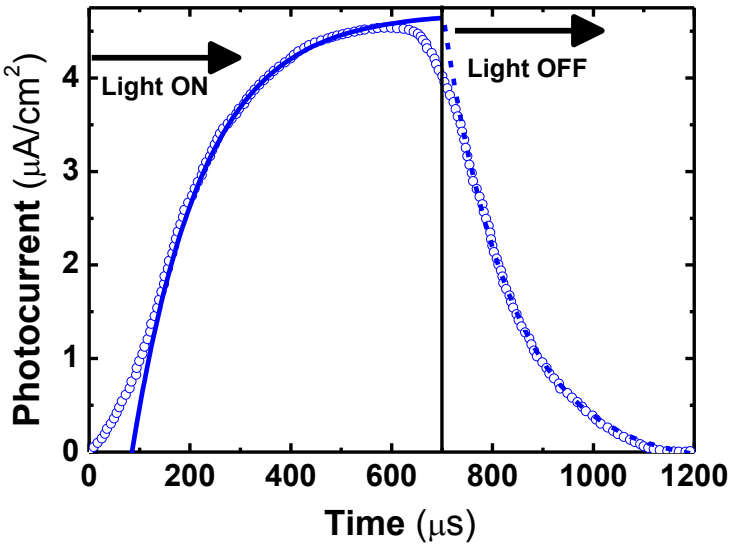

Figure 65: Photocurrent transient response measured at 0 V under an incident light at 1550 nm that is chopped at 800 Hz. Continuous and dotted lines stand for exponential grow/decay fit.

As follow a resume of the figures of merit registered for the PbS Schottky photodiode that we have obtained.

Table 5: A summary of the obtained PbS QD-solid-based Schottky photodiode figures of merit.

Active area (mm2)	**Spectral range** (nm)	**Responsivity** (A/W)	**EQE** (%)	**Detectivity** (Jones)	**NEP** (pW)	**Transient current constant** (μs)	**Air Stability** (days)
1	900- 1500	0.27	22	10^{11}	2	135	120

Conclusiones

Esta tesis se ha dedicado al desarrollo de fotodetectores relativamente estables en condiciones ambientales, altamente eficientes en la tercera ventana de telecomunicaciones ópticas, sobre la base de capas delgadas de QDs de PbS, los cuales se han procesado en disolución.

Para este propósito, primero hemos centrado nuestros estudios en la síntesis química de los QDs de PbS para conseguir nanocristales uniformes en morfología y tamaño para luego enfocarse en la optimización de la dispersión coloidal para la producción de películas delgadas bajo condiciones ambientales:

- Se ha desarrollado una ruta para producir, de manera reproducible, QDs de PbS protegidos con OAm altamente monodispersos de 6,7 ± 0,5 nm de diámetro. Este tamaño define una resonancia excitónica en la absorción a aproximadamente 1500 nm. Los análisis de XRD y GIXD evidencian la alta cristalinidad de los QDs de PbS sintetizados, cuya estructura cristalina es de tipo NaCl como el PbS masivo. Esto también es indicativo de la ausencia de productos sin reaccionar en la superficie de los QDs después de la síntesis. El análisis HRTEM también confirma la ausencia de defectos reticulares en el núcleo de los nanocristales.
- La disolución coloidal de QDs de PbS ha sido convertida en una nanotinta optimizada en sus propiedades reológicas para producir películas delgadas autoensambladas.
- Se demostró que la técnica de deposición por doctor blading permite la producción de películas de QDs de alta calidad con un espesor en el rango de 30 nm a 1 μm, aproximadamente. Este método de deposición se ha aplicado con éxito en áreas grandes (> 10 cm^2), pero también en superficies pequeñas (20 mm^2), con bajo consumo de material si se compara con el método de deposición más popular (recubrimiento por centrifugación).
- Se han producido sólidos de QDs de PbS libres de defectos estructurales, como agrietamiento o poros, con una superficie bastante lisa, como se desprende de su caracterización morfológicaº. Esto es de importancia clave para el desarrollo de dispositivos optoelectrónicos de alto rendimiento basados en QDs.

- Las moléculas originales de OAm presentes en la superficie de los QDs de PbS, junto con un proceso de secado lento de la nanotinta, han permitido que los nanocristales se autoensamblen en un supercrital de estructura cúbica centrada en el cuerpo una vez depositada en el sustrato, como se ha confirmado a través de los picos de difracción de rayos X a bajo ángulo.
- Los sólidos de QDs de PbS con ligandos de OAm tienen un comportamiento aislante. De esta manera, se ha investigado el efecto de alterar la química de la superficie de los QDs de PbS en los sólidos formados por éstos a través de un procedimiento de intercambio de ligando en estado sólido utilizando MPA y TBAI para mejorar la movilidad de los portadores. Ambos tratamientos con MPA y TBAI demostraron mejorar la conductividad de los sólidos de QDs. La resistividad disminuye de $\rho \approx 10^{10}$ Ωcm con OAm a $\rho \approx 10^{5}$ Ωcm con MPA y $\rho \approx 10^{4}$ Ωcm con TBAI, principalmente debido a un incremento notable de la concentración de portadores libres (huecos), si bien la movilidad se reduce sensiblemente en TBAI.
- Ambos tratamientos con MPA y TBAI dieron como resultado una fuerte disminución de la distancia entre partículas. Además, el MPA permite una eficiente pasivación de la superficie de los QDs evitando fenómenos de oxidación y preservando las propiedades de confinamiento cuántico de los nanocristales. Los QDs tratados con TBAI posiblemente tienden a formar aglomerados, causando un debilitamiento del confinamiento cuántico en los QDs, como se desprende de las imágenes TEM y de los espectros de absorción.
- Los efectos del intercambio de ligando en estado sólido de QDs de PbS también se han estudiado mediante XPS. Antes del intercambio de ligando, los sólidos de QDs pasivados con OAm mostraron la presencia de productos de oxidación tales como $PbSO_3$ en la superficie de los QDs. Después del intercambio de ligando no se observó oxidación, aunque sí se observaron nuevas especies, principalmente $Pb(OH)_2$ e IO_2 en las superficie de los QDs tratados con MPA y TBAI, respectivamente. Estas especies no afectan a la calidad estructural del núcleo de PbS y pasivan eficazmente la superficie de los QDs.

Finalmente, se ha estudiado a fondo la influencia de los tratamientos con MPA y TBAI (y las especies detectadas en superficie que se señalaron arriba) en las propiedades electro-ópticas de los sólidos de QDs medidas en dispositivos fotoconductores:

- La técnica de deposición doctor blading se aplicó con éxito para la fabricación de fotoconductores de alta calidad basados en solidos de QDs de PbS. Se ha estudiado y comparado el efecto del intercambio de ligandos en estado sólido posteriormente al procesamiento de TBAI y MPA sobre las propiedades optoelectrónicas de los fotoconductores fabricados. Logramos las mejores figuras de mérito globales utilizando MPA, principalmente debido a sus propiedades químicas, que permiten una mejor pasivación de los defectos superficiales en los nanocristales de PbS, en comparación con el TBAI. En el primer caso, el transporte de carga se debió principalmente a los portadores mayoritarios (huecos) a través de, presumiblemente, minibandas de huecos formadas en el sólido de QDs debido al acoplamiento electrónico tridimensional entre los QDs. La corta distancia entre partículas determinada por los ligandos de MPA condujo a movilidades de hasta 10^{-4} $cm^2 \cdot V^{-1}s^{-1}$. Además, la concentración de huecos/dopaje (~ 2×10^{15} cm^{-3}) es suficientemente baja y produce corrientes de oscuridad muy pequeñas, lo que es fundamental para obtener unos valores elevados de sensibilidad fotoconductiva y detectividadad. En el caso de TBAI, donde el nivel de dopaje era más alto (~ 2×10^{16} cm^{-3}) y la movilidad era menor que 2×10^{-5} $cm2 \cdot V^{-1}s^{-1}$, el transporte de carga parece estar influenciado por una banda adicional asociada a niveles de energía (trampas) relativamente profundos (el efecto de agregación de los QDs puede jugar un papel relevante en este mecanismo), lo que lleva a corrientes de oscuridad mucho más elevadas. El efecto resultante es una sensibilidad y una detectividad más pequeñas en los dispositivos tratados con TBAI.
- Desde el punto de vista de la cinética asociada con el exceso de portadores fotogenerados, los valores para los sólidos de QDs tratados con MPA y TBAI no fueron muy diferentes, como se deduce de su comportamiento bajo niveles relativamente altos de inyección de fotoportadores (10^{14}-10^{15} cm^{-3}). La principal diferencia en el transporte de portadores de carga mayoritarios bajo oscuridad limita la detección de señales de luz muy bajas, que está regulada por trampas relativamente poco profundas, situadas cerca de la banda de conducción del sólido de QDs. Hemos usado un modelo que incluye la presencia de tales "trampas seguras" para reproducir la evolución observada de la fotocorriente y la responsividad con la potencia de la luz incidente. Se alcanzaron valores elevados de responsividad, 15-70 A/W (para longitudes de canal de 20 y 5 μm,

respectivamente) a 1550 nm, en los dispositivos tratados con MPA, pero solo cuando la potencia de luz incidente es muy baja, con una contraparte negativa asociada a la lenta respuesta temporal del fotoconductor. El menor ruido en estos dispositivos tratados con MPA hace que la detectividad resulte ser mayor que 10^{11} (10^{12} si dominase el ruido de disparo, "shot noise") Jones.

Finalmente, hemos desarrollado fotodiodos Schottky basados en sólidos de QDs de PbS como fotodetectores en longitudes de onda de telecomunicaciones.

- Se fabricaron con éxito fotodiodos de unión Schottky sobre la base de sólidos de QDs de PbS tratados mediante intercambio de ligandos en estado sólido con MPA. Obtuvimos una responsividad R = 0.26 A W^{-1} a 1500 nm y una detectividad D * = 10^{11} Jones con una respuesta temporal de aproximadamente 135 µs. Estos resultados demuestran que los sólidos procesados a partir de nanotintas de QDs de PbS mediante la técnica doctor blading podrían allanar el camino hacia una tecnología rentable en continuo (roll-to-roll) compatible con el desarrollo de fotodetectores multiespectrales avanzados y células solares.

Conclusions

This thesis has been dedicated to the development of highly sensitive air-stable solution-processed photodetectors at the third optical telecom window, based on PbS QDs.

For this purpose, we have first focused our studies on the chemical synthesis of PbS QDs with high uniformity in size and shape and its optimization for the production of thin films under ambient conditions:

- It was developed a route to produce in a reproducible way highly monodispersed OAm-capped PbS QDs of 6.7±0.5 nm in diameter. This size is defining an exciton resonance in absorption at around 1500 nm. XRD and GIXD analysis evidence the high crystallinity of synthesized PbS QDs whose crystal structure corresponds to the rock salt crystal structure of PbS bulk. This is also indicative of the absence of unreacted products on the QD surface after the synthesis. HRTEM analysis also confirms the absence of lattice defects in the core of PbS QDs.
- The colloidal solution of PbS QDs has been converted into a nanoink optimized in its rheological properties to produce self-assembled thin films following a bottom-up approach.
- The doctor blading technique was proved to yield high quality QD-solids films of thickness ranging from 30 nm to 1 μm, approximately. This deposition method has been successfully applied over large areas (> 10 cm^2), but also over small ones (20 mm^2), with a very reduced material consumption if compared to the most popular spin coating deposition method.
- The as produced PbS QD-solids have been characterized in their morphology showing no sign of structural defect as cracking or pinholes and a smooth surface. This is of key importance for the development of high-performance QD-based optoelectronic devices.
- The original OAm molecules present on the surface of PbS QDs, together with a slow drying process of the nanoink, allows the QDs to self-assemble into a close-packed BCC 3D-superlattice once deposited on the substrate, as confirmed by low-angle XRD patterns.
- The OAm-capped PbS QD-solids demonstrate insulating behaviour. Thus, we investigated the effects of altering the surface chemistry of the PbS QDs in the QD-solids via solid-state ligand

exchange using MPA and TBAI to improve carrier mobility. Both treatments with MPA and TBAI demonstrated to improve the conductivity of the QD-solids. The resistivity decreases from $\rho \approx 10^{10}$ Ωcm with OAm to $\rho \approx 10^{5}$ Ωcm with MPA and $\rho \approx 10^{4}$ Ωcm with TBAI.

- Both treatments using MPA and TBAI resulted in a strong decrease of interparticle distance. Moreover, MPA efficiently passivate the QD surface avoiding oxidation, and preserves the QD quantum confinement properties. TBAI-treated QDs possibly tend to form agglomerates, causing a weakening of the QD quantum confinement, as evinced from TEM images and absorption spectra.
- The effects of ligand exchange on the PbS QD-solid was followed using XPS. Before ligand exchange, OAm QD-solids showed oxidation species such as $PbSO_3$ at the surface of PbS QDs. After ligand exchange, no oxidation was observed and new oxygen-containing species appear, manly $Pb(OH)_2$ and IO_2 in MPA and TBAI treated PbS QDs. These species do not affect the structural quality of the bulk-like PbS core and effectively passivate the QD surface.

The influence of these new species on the electro-optical properties of the QD-solids has been thoroughly studied in photoconductors devices:

- The doctor-blade deposition technique was successfully applied for the fabrication of high-quality PbS QD-solid-based photoconductors with different inter-electrode channel lengths. We studied and compared the effect of TBAI and MPA post-processing solid-state ligand exchange on the optoelectronic properties of PbS QD-solid-based photoconductors. We achieved the best overall photoconductive figures of merit using MPA, mainly attributed to the different chemical nature of passivation of the PbS QD surface defects, as compared to TBAI. In the first case, the charge transport was mainly due to majority carriers (holes) through the valence miniband formed in the QD-solid by the three-dimensional electronic coupling between QDs. The short inter-particle distance determined by the MPA ligands led to mobilities up to 10^{-4} $cm^2 \cdot V^{-1}s^{-1}$. Furthermore, the doping/hole concentration (~2×10^{15} cm^{-3}) was sufficiently low to yield very small dark currents, which is primordial for obtaining high photoconductive sensitivities and detectivities. In the case of TBAI, where the doping level was higher (~2×10^{16} cm^{-3}) and mobility smaller than 2×10^{-5} $cm^2 \cdot V^{-1}s^{-1}$, the charge transport seems to be influenced by an additional band associated with mid-

gap trap states (QD aggregation may play a role in this mechanism), leading to much higher dark currents. The resulting effect is the smaller sensitivity and detectivity deduced in TBAI-treated photodevices.

- From the point of view of the kinetics associated with the excess photogenerated carriers, values for both MPA- and TBAI-treated QD-solids were not too different, as revealed by their behaviour under relatively high photocarrier injection levels (10^{14}–10^{15} cm^{-3}). The major difference in the majority charge-carrier transport under dark conditions limits the detectivity for very low light signals, which is regulated by relatively shallow traps close to the conduction band of the QD-solid. A model including the presence of such "safe traps" reproduces the observed photocurrent and responsivity evolution with the incident light power. Values of responsivity as high as 15–70 A/W (for 20- and 5-µm channel lengths, respectively) at 1550 nm, were reached for MPA-treated photodevices, but only under very low incident powers, with a negative counterpart associated to the slow photo-response. The lower noise in these MPA-treated devices makes detectivity greater than 10^{11} (10^{12} if shot noise dominates) Jones.

We finally developed PbS QD-solid-based Schottky photodiodes for photodetector at telecom wavelengths.

- Schottky photodiodes were successfully fabricated on the basis of PbS QD-solids treated by MPA solid-state ligand exchange. We obtained a responsivity of R = 0.26 A W^{-1} at 1500 nm and a detectivity of D* = 10^{11} jones with a time response of about 135 µs. These results demonstrate that solids processed from PbS QD nanoinks by doctor blading might pave the way to a cost-effective roll-to-roll compatible technology for the development of advanced multispectral photodetectors and solar cells.

Outlooks

On the basis of our findings, we can identify two major routes for improving future photodevices based on QD-solids depending on the photocarrier injection level in photoconductors: (1) for the detection of very-low-light signals, the use of “safe traps” is positive in order to obtain very high photoconductive responsivity/gain, but it will be necessary to reduce the trap energy depth (i.e., create traps as shallow as possible) to reduce the response time; and (2) for detection of high-light signals, the only way of increasing the photoconductive gain is through an effective increase in carrier mobilities in the QD-solid.

The limited carrier mobility in QD-solids, due to the hopping nature of transport among nanocrystals appeared to be a major aspect to improve also in photodiodes. An interesting solution toward significant mobility increase can be achieved by the fabrication of multilayer structures with QDs and highly conductive two-dimensional materials (i.e. graphene). This concept is essentially based on the possibility to exploit the high absorption coefficient of PbS QDs and the high carrier mobilities of 2D materials. In this case the main issue to overcome would be the reduction of interfacial resistance between 2D materials and QDs for an efficient charge transport in such multi-layered structures.

Throughout this thesis work we have addressed PbS nanocrystals that contain lead. Due to the better overall performances enabled by colloidal nanocrystals many researches on optoelectronic devices, like those cited in this thesis, relay on heavy metals containing compounds as PbSe, PbTe, CdS, CdSe, etc. More research efforts on synthesis and material engineering that focus on environmentally friendly approaches are necessary. The production of high-performance semiconducting QDs based on “green” materials is crucial to boost large-scale quantum dot-based technology.

Bibliography

[1] G. H. BuAbbud, “High power fiber lasers and amplifiers for applications in telecommunications,” *Opt. Fiber Commun. (OFC), collocated Natl. Fiber Opt. Eng. Conf. 2010 Conf.*, p. 2010, 2010.

[2] R. Paschotta, *Encyclopedia of Laser Physics and Technology*, vol. 1. 2009.

[3] I. P. Kaminow, T. Li, and A. E. Willner, *Optical Fiber Telecommunications: Systems and Networks: Sixth Edition*. 2013.

[4] D. V. Talapin, J.-S. Lee, M. V. Kovalenko, and E. V. Shevchenko, “Prospects of Colloidal Nanocsrystals for Electronic and Optoelectronic Applications,” *Chem. Rev.*, vol. 110, pp. 389–458, 2010.

[5] C. Downs and T. E. Vandervelde, “Progress in infrared photodetectors since 2000,” *Sensors (Switzerland)*, 2013.

[6] G. Konstantatos and E. H. Sargent, “Solution-processed quantum dot photodetectors,” *Proc. IEEE*, vol. 97, no. 10, pp. 1666–1683, 2009.

[7] E. Heves and Y. Gurbuz, “Highly responsive, solution-based Al/PbS and Au-Ti/PbS schottky photodiodes for SWIR detection,” *IEEE Sens. J.*, vol. 14, no. 3, pp. 816–820, 2014.

[8] A. Guchhait, A. K. Rath, and A. J. Pal, “Near-IR activity of hybrid solar cells: Enhancement of efficiency by dissociating excitons generated in PbS nanoparticles,” *Appl. Phys. Lett.*, vol. 96, no. 7, 2010.

[9] K. Shen, S. Baig, G. Jiang, Y. hun Paik, S. J. Kim, and M. R. Wang, “Improved light emitting UV curable PbS quantum dots-polymer composite optical waveguides,” *Opt. Commun.*, vol. 402, pp. 606–611, 2017.

[10] G. Konstantatos, I. Howard, A. Fischer, S. Hoogland, J. Clifford, E. Klem, L. Levina, and E. H.

Sargent, “Ultrasensitive solution-cast quantum dot photodetectors.,” *Nature*, vol. 442, no. 7099, pp. 180–183, 2006.

[11] C. B. Murray, C. R. Kagan, and M. G. Bawendi, “Synthesis and Characterization of Monodisperse Nanocrystals and Close-Packed Nanocrystal Assemblies,” *Annu. Rev. Mater. Sci.*, vol. 30, no. 1, pp. 545–610, 2000.

[12] D. B. Mitzi, L. L. Kosbar, C. E. Murray, M. Copel, and A. Afzali, “High-mobility ultrathin semiconducting films prepared by spin coating.,” *Nature*, vol. 428, no. 6980, pp. 299–303, 2004.

[13] S. Maenosono, T. Okubo, and Y. Yamaguchi, “Overview of nanoparticle array formation by wet coating,” *Journal of Nanoparticle Research*, vol. 5, no. 1–2. pp. 5–15, 2003.

[14] H. Liu, M. Li, O. Voznyy, L. Hu, Q. Fu, D. Zhou, Z. Xia, E. H. Sargent, and J. Tang, “Physically flexible, rapid-response gas sensor based on colloidal quantum dot solids,” *Adv. Mater.*, vol. 26, no. 17, pp. 2718–2724, 2014.

[15] M. Scheele, W. Brutting, and F. Schreiber, “Coupled organic-inorganic nanostructures (COIN),” *Phys. Chem. Chem. Phys.*, vol. 17, no. 1, pp. 97–111, 2015.

[16] K. Whitham, J. Yang, B. H. Savitzky, L. F. Kourkoutis, F. Wise, and T. Hanrath, “Charge transport and localization in atomically coherent quantum dot solids,” *Nat. Mater.*, no. February, pp. 1–8, 2016.

[17] F. Xu, L. Gerlein, X. Ma, C. Haughn, M. Doty, and S. Cloutier, “Impact of Different Surface Ligands on the Optical Properties of PbS Quantum Dot Solids,” *Materials (Basel).*, vol. 8, no. 4, pp. 1858–1870, 2015.

[18] V. Bertasius, R. Mastria, A. Rizzo, G. Gigli, C. Giansante, and V. Gulbinas, “Charge Carrier Generation and Extraction in Hybrid Polymer/Quantum Dot Solar Cells,” *J. Phys. Chem. C*, vol. 120, no. 26, pp. 14356–14364, 2016.

[19] L. Hu, Z. Zhang, R. J. Patterson, Y. Hu, W. Chen, C. Chen, D. Li, C. Hu, C. Ge, Z. Chen, L. Yuan, C. Yan, N. Song, Z. L. Teh, G. J. Conibeer, J. Tang, and S. Huang, “Achieving high-performance

PbS quantum dot solar cells by improving hole extraction through Ag doping," *Nano Energy*, vol. 46, pp. 212–219, 2018.

[20] J. Kurpiers, D. M. Balazs, A. Paulke, S. Albrecht, I. Lange, L. Protesescu, M. V. Kovalenko, M. A. Loi, and D. Neher, "Free carrier generation and recombination in PbS quantum dot solar cells," *Appl. Phys. Lett.*, vol. 108, no. 10, 2016.

[21] R. K. Joshi and H. K. Sehgal, "Density of states near Fermi level in PbS nanoparticle films," *Phys. E-Low-Dimensional Syst. Nanostructures*, vol. 23, no. 1–2, pp. 168–170, 2004.

[22] J. M. Lee, B. H. Kwon, H. Il Park, H. Kim, M. G. Kim, J. S. Park, E. S. Kim, S. Yoo, D. Y. Jeon, and S. O. Kim, "Exciton dissociation and charge-transport enhancement in organic solar cells with quantum-dot/N-doped CNT hybrid nanomaterials," *Adv. Mater.*, vol. 25, no. 14, pp. 2011–2017, 2013.

[23] Y. Zhang, Q. Chen, A. P. Alivisatos, and M. Salmeron, "Dynamic Charge Carrier Trapping in Quantum Dot Field Effect Transistors," *Nano Lett.*, vol. 15, no. 7, pp. 4647–4663, 2015.

[24] Y. Diao, L. Shaw, and S. C. B. Mannsfeld, "Morphology control strategies for solution- processed organic semiconductor thin fi lms," *Energy Environ. Sci.*, vol. 7, pp. 2145–2159, 2014.

[25] J. Gao and J. C. Johnson, "Charge trapping in bright and dark states of coupled PbS quantum dot films," *ACS Nano*, vol. 6, no. 4, pp. 3292–3303, 2012.

[26] P. Nagpal and V. I. Klimov, "Role of mid-gap states in charge transport and photoconductivity in semiconductor nanocrystal films," *Nat. Commun.*, vol. 2, p. 486, 2011.

[27] Y. Yin and a P. Alivisatos, "Colloidal nanocrystal synthesis and the organic-inorganic interface.," *Nature*, vol. 437, no. 7059, pp. 664–670, 2005.

[28] R. L. Petritz, "Theory of photoconductivity in semiconductor films," *Phys. Rev.*, vol. 104, no. 6, pp. 1508–1516, 1956.

[29] J. Liu, "Photodetectors," in *Photonic Devices*, 2005, pp. 926–1017.

[30] R. Saran and R. J. Curry, “Lead sulphide nanocrystal photodetector technologies,” *Nat. Photonics*, vol. 10, no. 2, pp. 81–92, 2016.

[31] S. Espevik, “Mechanism of Photoconductivity in Chemically Deposited Lead Sulfide Layers,” *J. Appl. Phys.*, vol. 42, no. 9, p. 3513, 1971.

[32] A. Maulu, J. Navarro-Arenas, P. Rodríguez-Cantó, J. Sánchez-Royo, R. Abargues, I. Suárez, and J. Martínez-Pastor, “Charge Transport in Trap-Sensitized Infrared PbS Quantum-Dot-Based Photoconductors: Pros and Cons,” *Nanomaterials*, vol. 8, no. 9, 677, (18 pp.) 2018.

[33] P. Nagpal and V. I. Klimov, “Role of mid-gap states in charge transport and photoconductivity in semiconductor nanocrystal films,” *Nat. Commun.*, vol. 2, p. 486, 2011.

[34] R. Saran and R. J. Curry, “Lead sulphide nanocrystal photodetector technologies,” *Nat. Photonics*, vol. 10, no. 2, pp. 81–92, 2016.

[35] G. Konstantatos and E. H. Sargent, “PbS colloidal quantum dot photoconductive photodetectors: Transport, traps, and gain,” *Appl. Phys. Lett.*, vol. 91, no. 17, 2007.

[36] C. Quantum and D. Photovoltaic, “Charge Trapping Dynamics in PbS Devices,” no. 10, pp. 8771–8779, 2013.

[37] D. Bozyigit, S. Volk, O. Yarema, and V. Wood, “Supporting Information : Quantification of Deep Traps in Nanocrystal Solids , their Electronic Properties , and their Influence on Device Behavior,” pp. 1–12, 2013.

[38] P. R. Berger, “Metal-semiconductor-metal photodetectors,” *Proc. SPIE - Int. Soc. Opt. Eng.*, vol. 4285, no. 2001, pp. 198–207, 2001.

[39] P. C. Eng, S. Song, and B. Ping, “State-of-the-art photodetectors for optoelectronic integration at telecommunication wavelength,” *Nanophotonics*, vol. 4, no. 1, pp. 277–302, 2015.

[40] G. Konstantatos and E. H. Sargent, “Colloidal quantum dot photodetectors,” in *Infrared Physics and Technology*, 2011, vol. 54, no. 3, pp. 278–282.

[41] S. Nudelman, “The Detectivity of Infrared Photodetectors,” *Appl. Opt.*, vol. 1, no. 5, p. 627, 1962.

[42] T. H. E. B. Andwidth and O. T. Radeoff, “Detection Regimes and Figures of Merit,” *Quantum*, pp. 37–46.

[43] T. Emission, “Photodetectors,” *Kirk-Othmer Encycl. Chem. Technol.*, 2001.

[44] E. R. Chenette, “Noise in Semiconductor Devices,” *Adv. Electron. Electron Phys.*, vol. 23, no. C, pp. 303–346, 1967.

[45] A. De Iacovo, C. Venettacci, L. Colace, L. Scopa, S. Foglia, A. De Iacovo, C. Venettacci, L. Colace, L. Scopa, and S. Foglia, “Noise performance of PbS colloidal quantum dot photodetectors,” vol. 211104, 2017.

[46] H. Liu, E. Lhuillier, P. Guyot-sionnest, H. Liu, E. Lhuillier, and P. Guyot-sionnest, “1 / f noise in semiconductor and metal nanocrystal solids 1 / f noise in semiconductor and metal nanocrystal solids,” vol. 154309, pp. 0–7, 2014.

[47] I. Kang and F. W. Wise, “Electronic structure and optical properties of PbS and PbSe quantum dots,” *J. Opt. Soc. Am. B*, vol. 14, no. 7, p. 1632, 1997.

[48] L. Cademartiri and G. a Ozin, “Emerging strategies for the synthesis of highly monodisperse colloidal nanostructures.,” *Philos. Trans. A. Math. Phys. Eng. Sci.*, vol. 368, no. 1927, pp. 4229–48, 2010.

[49] I. Moreels, K. Lambert, D. De Muynck, F. Vanhaecke, D. Poelman, J. C. Martins, G. Allan, and Z. Hens, “Size-Dependent Optical Properties of Colloidal {PbS} Quantum Dots,” *ACS Nano*, vol. 3, no. 10, pp. 3023–3030, 2009.

[50] M. A. Hines and G. D. Scholes, “Colloidal PbS Nanocrystals with Size-Tunable Near-Infrared Emission: Observation of Post-Synthesis Self-Narrowing of the Particle Size Distribution,” *Adv. Mater.*, vol. 15, no. 21, pp. 1844–1849, 2003.

[51] J. H. Warner and H. Cao, “Shape control of PbS nanocrystals using multiple surfactants.,”

Nanotechnology, vol. 19, p. 305605, 2008.

[52] † Ludovico Cademartiri, ‡ Jacopo Bertolotti, ‡ Riccardo Sapienza, ‡ Diederik S. Wiersma, †,§ and Georg von Freymann, and † Geoffrey A. Ozin*, "Multigram Scale, Solventless, and Diffusion-Controlled Route to Highly Monodisperse PbS Nanocrystals," pp. 671–673, 2005.

[53] F. D. Martinez-Mancera and J. L. Hernandez-Lopez, "Physical characterization and photoluminescence properties of thioglycolic acid-stabilized lead sulfide nanocrystals," *Mater. Chem. Phys.*, vol. 148, no. 3, pp. 1045–1054, 2014.

[54] C. R. Bealing, W. J. Baumgardner, J. J. Choi, T. Hanrath, and R. G. Hennig, "Predicting nanocrystal shape through consideration of surface-ligand interactions," *ACS Nano*, vol. 6, no. 3, pp. 2118–2127, 2012.

[55] A. I. Ekimov and A. A. Onoshchenko, "Quantum size effect in three-dimensional microscopic semiconductor crystals," *Am. Inst. Phys.*, vol. 34, no. 6, p. 345, 1982.

[56] A. P. Alivisatos, "Perspectives on the physical chemistry of semiconductor nanocrystals," *Journal of Physical Chemistry*, vol. 100, no. 31. pp. 13226–13239, 1996.

[57] R. Rossetti and L. Brus, "Electron-hole recombination emission as a probe of surface chemistry in aqueous cadmium sulfide colloids," *J. Phys. Chem.*, vol. 86, no. 23, pp. 4470–4472, 1982.

[58] C. B. Murray, D. Norris, and M. G. Bawendi, "Synthesis and characterization of nearly monodisperse CdE (E= S, Se, Te) semiconductor nanocrystallites," *J. Am. Chem. Soc.*, vol. 115, no. 4, pp. 8706–8715, 1993.

[59] Y. Zhang, D. Zherebetskyy, N. D. Bronstein, S. Barja, L. Lichtenstein, D. Schuppisser, L. W. Wang, A. P. Alivisatos, and M. Salmeron, "Charge percolation pathways guided by defects in quantum dot solids," *Nano Lett.*, vol. 15, no. 5, pp. 3249–3253, 2015.

[60] C. R. Kagan and C. B. Murray, "Charge transport in strongly coupled quantum dot solids.," *Nat. Nanotechnol.*, vol. 10, no. 12, pp. 1013–1026, 2015.

[61] D. Kim, D. H. Kim, J. H. Lee, and J. C. Grossman, “Impact of stoichiometry on the electronic structure of PbS quantum dots,” *Phys. Rev. Lett.*, vol. 110, no. 19, pp. 1–5, 2013.

[62] D.-H. Chen and S.-H. Wu, “Synthesis of Nickel Nanoparticles in Water-in-Oil Microemulsions,” *Chem. Mater.*, vol. 12, no. 5, pp. 1354–1360, 2000.

[63] H. Y. Park, I. Ryu, J. Kim, S. Jeong, S. Yim, and S. Y. Jang, “PbS quantum dot solar cells integrated with sol-gel-derived ZnO as an n-type charge-selective layer,” *J. Phys. Chem. C*, vol. 118, no. 31, pp. 17374–17382, 2014.

[64] C. De Mello Donegá, P. Liljeroth, and D. Vanmaekelbergh, “Physicochemical evaluation of the hot-injection method, a synthesis route for monodisperse nanocrystals,” *Small*, vol. 1, no. 12, pp. 1152–1162, 2005.

[65] M. Z. Hu and T. Zhu, “Semiconductor Nanocrystal Quantum Dot Synthesis Approaches Towards Large-Scale Industrial Production for Energy Applications.,” *Nanoscale Res. Lett.*, vol. 10, no. 1, p. 469, 2015.

[66] X. Peng, L. Manna, W. Yang, J. Wickham, E. Scher, A. Kadavanich, and A. P. Alivisatos, “Shape control of {CdSe} nanocrystals,” *Nature*, vol. 404, no. 6773, pp. 59–61, 2000.

[67] H. Li, D. Chen, L. Li, F. Tang, L. Zhang, and J. Ren, “Size- and shape-controlled synthesis of PbSe and PbS nanocrystals via a facile method,” *CrystEngComm*, vol. 12, no. 4, p. 1127, 2010.

[68] B. N. Pal, I. Robel, A. Mohite, R. Laocharoensuk, D. J. Werder, and V. I. Klimov, “High-Sensitivity p-n junction photodiodes based on Pbs nanocrystal quantum dots,” *Adv. Funct. Mater.*, vol. 22, no. 8, pp. 1741–1748, 2012.

[69] L. C. Frenette and T. D. Krauss, “Uncovering active precursors in colloidal quantum dot synthesis,” *Nat. Commun.*, vol. 8, no. 1, 2017.

[70] M. Green, “The nature of quantum dot capping ligands,” *Journal of Materials Chemistry*, vol. 20, no. 28. pp. 5797–5809, 2010.

[71] R. Alam and M. M. Maye, “Asymmetric quantum dot growth via temperature cycling,” *Inorganica Chim. Acta*, vol. 380, no. 1, pp. 114–117, 2012.

[72] D. Zahn, “Thermodynamics and Kinetics of Prenucleation Clusters, Classical and Non-Classical Nucleation,” *ChemPhysChem*, vol. 16, no. 10, pp. 2069–2075, 2015.

[73] A. Volmer, M.; Weber, “Nucleus Formation in Supersaturated Systems,” *Z. Phys. Chem*, vol. 119, pp. 277–301, 1926.

[74] R. Becker, “Die Keimbildung bei der Ausscheidung in metallischen Mischkristallen,” *Ann. Phys.*, vol. 424, no. 1–2, pp. 128–140, 1938.

[75] V. LaMer and R. Dinegar, “Theory, production and mechanism of formation of monodispersed hydrosols,” *J. Am. Chem. …*, vol. 72, no. 8, pp. 4847–4854, 1950.

[76] P. W. Voorhees, “The theory of Ostwald ripening,” *J. Stat. Phys.*, vol. 38, no. 1–2, pp. 231–252, 1985.

[77] G. Madras and B. J. McCoy, “Distribution kinetics theory of Ostwald ripening,” *J. Chem. Phys.*, vol. 115, no. 14, pp. 6699–6706, 2001.

[78] R. Finsy, “On the critical radius in Ostwald ripening,” *Langmuir*, vol. 20, no. 7, pp. 2975–2976, 2004.

[79] P. Dagtepe and V. Chikan, “Quantized Ostwald ripening of colloidal nanoparticles,” *J. Phys. Chem. C*, vol. 114, no. 39, pp. 16263–16269, 2010.

[80] I. Moreels, Y. Justo, B. De Geyter, K. Haustraete, J. C. Martins, and Z. Hens, “Size-tunable, bright, and stable PbS quantum dots: A surface chemistry study,” *ACS Nano*, vol. 5, no. 3, pp. 2004–2012, 2011.

[81] C. Giansante, I. Infante, E. Fabiano, R. Grisorio, G. P. Suranna, and G. Gigli, “‘darker-than-black’ PbS quantum dots: Enhancing optical absorption of colloidal semiconductor nanocrystals via short conjugated ligands,” *J. Am. Chem. Soc.*, vol. 137, no. 5, pp. 1875–1886, 2015.

[82] I. Moreels, Y. Justo, B. De Geyter, K. Haustraete, J. C. Martins, and Z. Hens, “Quantum Dots: A Surface Chemistry Study,” *ACS Nano*, vol. 5, no. 3, pp. 2004–2012, 2012.

[83] V. Klimov, *Nanocrystal Quantum Dots*, vol. 40, no. 6. 2010.

[84] L. Cademartiri, E. Montanari, G. Calestani, A. Migliori, A. Guagliardi, and G. a Ozin, “Size-dependent extinction coefficients of PbS quantum dots,” *J. Am. Chem. Soc.*, vol. 128, pp. 10337–10346, 2006.

[85] D. Zhang, J. Song, J. Zhang, Y. Wang, S. Zhang, and X. Miao, “A facile and rapid synthesis of lead sulfide colloidal quantum dots using in situ generated H2S as the sulfur source,” *CrystEngComm*, vol. 15, no. 13, p. 2532, 2013.

[86] J. Tang, “Materials Engineering for Stable and Efficient PbS Colloidal Quantum Dot Photovoltaics Materials Engineering for Stable and Efficient PbS Colloidal Quantum Dot Photovoltaics,” 2010.

[87] J. P. Clifford, G. Konstantatos, K. W. Johnston, S. Hoogland, L. Levina, and E. H. Sargent, “Fast, sensitive and spectrally tuneable colloidal-quantum-dot photodetectors.,” *Nat. Nanotechnol.*, vol. 4, no. 1, pp. 40–44, 2009.

[88] E. H. Gong, Xiwen;Yang, Zhenyu; Walters, Grant; Comin, Riccardo; Ning, Zhijun; Beauregard, Eric; Adinolfi, Valerio; Voznyy, Oleksandr;Sargent, “Highly efficient quantum dot near-infrared light-emitting diodes,” *Nat. Nanotechnol.*, vol. xx, no. xx, p. x, 2016.

[89] Z. Yang, O. Voznyy, M. Liu, M. Yuan, A. H. Ip, O. S. Ahmed, L. Levina, S. Kinge, S. Hoogland, and E. H. Sargent, “All-Quantum-Dot Infrared Light-Emitting Diodes,” *ACS Nano*, vol. 9, no. 12, pp. 12327–12333, 2015.

[90] C. Dang, J. Lee, K. Roh, H. Kim, S. Ahn, H. Jeon, C. Breen, J. S. Steckel, S. Coe-Sullivan, and A. Nurmikko, “Highly efficient, spatially coherent distributed feedback lasers from dense colloidal quantum dot films,” *Appl. Phys. Lett.*, vol. 103, no. 17, 2013.

[91] D. Pacifici, H. J. Lezec, and H. A. Atwater, “All-optical modulation by plasmonic excitation of {CdSe} quantum dots,” *Nat Phot.*, vol. 1, no. 7, pp. 402–406, 2007.

[92] N. Zhao, T. P. Osedach, L.-Y. Chang, S. M. Geyer, D. Wanger, M. T. Binda, A. C. Arango, M. G. Bawendi, and V. Bulovic, "Colloidal PbS Quantum Dot Solar Cells with High Fill Factor," *ACS Nano*, vol. 4, no. 7, pp. 3743–3752, 2010.

[93] Z. Ning, H. Dong, Q. Zhang, O. Voznyy, and E. H. Sargent, "Solar cells based on inks of n-type colloidal quantum dots," *ACS Nano*, vol. 8, no. 10, pp. 10321–10327, 2014.

[94] A. De Iacovo, C. Venettacci, L. Colace, L. Scopa, and S. Foglia, "PbS Colloidal Quantum Dot Photodetectors operating in the near infrared," *Sci. Rep.*, 2016.

[95] S. A. McDonald, G. Konstantatos, S. Zhang, P. W. Cyr, E. J. D. Klem, L. Levina, and E. H. Sargent, "Solution-processed PbS quantum dot infrared photodetectors and photovoltaics," *Nat. Mater.*, vol. 4, no. 2, pp. 138–142, 2005.

[96] A. Adamson and A. Gast, "Physical Chemistry Of Surfaces (Adamson, Gast , 6Ed, Wiley, 1997).pdf." p. 190, 1997.

[97] B. Derby, "Inkjet Printing of Functional and Structural Materials: Fluid Property Requirements, Feature Stability, and Resolution," *Annu. Rev. Mater. Res.*, vol. 40, no. 1, pp. 395–414, 2010.

[98] A. Fischer, L. Rollny, J. Pan, G. H. Carey, S. M. Thon, S. Hoogland, O. Voznyy, D. Zhitomirsky, J. Y. Kim, O. M. Bakr, and E. H. Sargent, "Directly deposited quantum dot solids using a colloidally stable nanoparticle ink," *Adv. Mater.*, vol. 25, no. 40, pp. 5742–5749, 2013.

[99] S. Ahmadi, N. Asim, M. A. Alghoul, F. Y. Hammadi, K. Saeedfar, N. A. Ludin, S. H. Zaidi, and K. Sopian, "The role of physical techniques on the preparation of photoanodes for dye sensitized solar cells," *Int. J. Photoenergy*, vol. 2014, 2014.

[100] L. Chen and E. Bonaccurso, "Effects of surface wettability and liquid viscosity on the dynamic wetting of individual drops," *Phys. Rev. E - Stat. Nonlinear, Soft Matter Phys.*, vol. 90, no. 2, pp. 1–9, 2014.

[101] M. D. Tyona, "A theorical Study on spin coating technique," *Adv. Mater. Res.*, vol. 2, no. 4, pp. 195–208, 2013.

[102] R. R. Eley, “Applied Rheology in the Protective and Decorative Coatings Industry,” *Rheol. Rev.*, vol. 3, pp. 173–240, 2005.

[103] A. a. Tracton, *Coatings technology - Fundaentals, Testing, and processing techniques*. 2007.

[104] E. Hrehorova, A. Pekarovicova, and P. D. Fleming, “Gravure Printability of Conducting Polymer Inks,” *Final Progr. Proc.*, vol. 4, pp. 107–110, 2006.

[105] “Fabrication of Thin Ceramic S S for Capacitors *,” *Contract*, 1947.

[106] G. A. Howcz, “Patent 2, 582, 993,” 1952.

[107] A. Berni, M. Mennig, and H. Schmidt, “Doctor blade,” in *Sol-Gel Technologies for Glass Producers and Users*, 2004, pp. 89–92.

[108] A. Maulu, P. J. Rodríguez Cantó, J. Navarro Arenas, R. Abargues, J. F. Sanchez-Royo, R. García Calzada, and J. P. Martínez-Pastor, “Strongly-coupled PbS QD-solids by Doctor-Blading for IR Photodetection,” *RSC Adv.*, vol. 6, pp. 80201–80212, 2016.

[109] Sun, Murray, Weller, Folks, and Moser, “Monodisperse FePt nanoparticles and ferromagnetic FePt nanocrystal superlattices,” *Science (80-.).*, vol. 287, no. 5460, pp. 1989–92, 2000.

[110] C. Daniel and J. O. Besenhard, *Handbook of Battery Materials: Second Edition*. 2011.

[111] A. H. Ip, S. M. Thon, S. Hoogland, O. Voznyy, D. Zhitomirsky, R. Debnath, L. Levina, L. R. Rollny, G. H. Carey, A. Fischer, K. W. Kemp, I. J. Kramer, Z. Ning, A. J. Labelle, K. W. Chou, A. Amassian, and E. H. Sargent, “Hybrid passivated colloidal quantum dot solids,” *Nat. Nanotechnol.*, vol. 7, no. 9, pp. 577–582, 2012.

[112] A. Patel, J. D., Mighri, F., Ajji and S. Elkoun, “Room Temperature Synthesis of Aminocaproic Acid-Capped Lead Sulphide Nanoparticles,” *Sci. Res.*, vol. 3, no. February, pp. 125–130, 2012.

[113] R. W. Crisp, D. M. Kroupa, A. R. Marshall, E. M. Miller, J. Zhang, M. C. Beard, and J. M. Luther, “Metal halide solid-state surface treatment for high efficiency PbS and PbSe QD solar cells.,” *Sci. Rep.*, vol. 5, p. 9945, 2015.

[114] F. Xu, L. Gerlein, X. Ma, C. Haughn, M. Doty, and S. Cloutier, “Impact of Different Surface Ligands on the Optical Properties of PbS Quantum Dot Solids,” *Materials (Basel).*, vol. 8, no. 4, pp. 1858–1870, 2015.

[115] C. C. Reinhart and E. Johansson, “Colloidally Prepared 3-Mercaptopropionic Acid Capped Lead Sulfide Quantum Dots,” *Chem. Mater.*, vol. 27, no. 21, pp. 7313–7320, 2015.

[116] M. E. Peach and S. Patai, “The Chemistry of the Thiol Groups,” p. 721, 1979.

[117] Z. Ning, Y. Ren, S. Hoogland, O. Voznyy, L. Levina, P. Stadler, X. Lan, D. Zhitomirsky, and E. H. Sargent, “All-inorganic colloidal quantum dot photovoltaics employing solution-phase halide passivation,” *Adv. Mater.*, vol. 24, no. 47, pp. 6295–6299, 2012.

[118] G. Niu, L. Wang, R. Gao, B. Ma, H. Dong, and Y. Qiu, “Inorganic iodide ligands in ex situ PbS quantum dot sensitized solar cells with I−/I3− electrolytes,” *J. Mater. Chem.*, vol. 22, no. 33, p. 16914, 2012.

[119] V. Malgras, A. Nattestad, Y. Yamauchi, S. X. Dou, and J. H. Kim, “The effect of surface passivation on the structure of sulphur-rich PbS colloidal quantum dots for photovoltaic application.,” *Nanoscale*, vol. 7, no. 13, pp. 5706–11, 2015.

[120] A. Nag, M. V Kovalenko, J. Lee, W. Liu, B. Spokoyny, and D. V Talapin, “Metal-free Inorganic Ligands for Colloidal Nanocrystals: S 2– , HS – , Se 2– , HSe – , Te 2– , HTe – , TeS 3 2– , OH – , and NH 2 – as Surface Ligands,” *J. Am. Chem. Soc.*, vol. 133, no. 27, pp. 10612–10620, 2011.

[121] E. J. D. Klem, H. Shukla, S. Hinds, D. D. MacNeil, L. Levina, and E. H. Sargent, “Impact of dithiol treatment and air annealing on the conductivity, mobility, and hole density in PbS colloidal quantum dot solids,” *Appl. Phys. Lett.*, vol. 92, no. 21, pp. 100–102, 2008.

[122] D. N. Dirin, M. I. Bodnarchuk, G. Nedelcu, P. Papagiorgis, G. Itskos, and M. V Kovalenko, “Lead Halide Perovskites and Other Metal Halide Complexes As Inorganic Capping Ligands for Colloidal Nanocrystals,” pp. 0–3, 2014.

[123] D. Zherebetskyy, M. Scheele, Y. Zhang, N. Bronstein, C. Thompson, D. Britt, M. Salmeron, P.

Alivisatos, and L.-W. Wang, “Hydroxylation of the surface of PbS nanocrystals passivated with oleic acid. (Suppl Mat),” *Science*, vol. 344, no. 6190, pp. 1380–4, 2014.

[124] W. K. Bae, J. Joo, L. A. Padilha, J. Won, D. C. Lee, Q. Lin, W. K. Koh, H. Luo, V. I. Klimov, and J. M. Pietryga, “Highly effective surface passivation of pbse quantum dots through reaction with molecular chlorine,” *J. Am. Chem. Soc.*, vol. 134, no. 49, pp. 20160–20168, 2012.

[125] J. Zhang, J. Gao, C. P. Church, E. M. Miller, J. M. Luther, V. I. Klimov, and M. C. Beard, “PbSe quantum dot solar cells with more than 6% efficiency fabricated in ambient atmosphere,” *Nano Lett.*, vol. 14, no. 10, pp. 6010–6015, 2014.

[126] L. Yan, X. Shen, Y. Zhang, T. Zhang, X. Zhang, Y. Feng, J. Yin, J. Zhao, and W. W. Yu, “Near-infrared light emitting diodes using PbSe quantum dots,” *RSC Adv.*, vol. 5, no. 67, pp. 54109–54114, 2015.

[127] I. J. Kramer, G. Moreno-Bautista, J. C. Minor, D. Kopilovic, and E. H. Sargent, “Colloidal quantum dot solar cells on curved and flexible substrates,” *Appl. Phys. Lett.*, vol. 105, no. 16, 2014.

[128] J. M. Luther, M. Law, M. C. Beard, Q. Song, M. O. Reese, R. J. Ellingson, and A. J. Nozik, “Schottky solar cells based on colloidal nanocrystal films,” *Nano Lett.*, vol. 8, no. 10, pp. 3488–3492, 2008.

[129] N. B. Kotadiya, A. J. Kothari, D. Tiwari, and T. K. Chaudhuri, “Photoconducting nanocrystalline lead sulphide thin films obtained by chemical bath deposition,” *Appl. Phys. A Mater. Sci. Process.*, vol. 108, no. 4, pp. 819–824, 2012.

[130] S. V Kershaw, A. S. Susha, and A. L. Rogach, “Narrow bandgap colloidal metal chalcogenide quantum dots: synthetic methods, heterostructures, assemblies, electronic and infrared optical properties.,” *Chem. Soc. Rev.*, vol. 42, no. 7, pp. 3033–87, 2013.

[131] V. Malgras, A. Nattestad, Y. Yamauchi, S. X. Dou, and J. H. Kim, “The effect of surface passivation on the structure of sulphur-rich PbS colloidal quantum dots for photovoltaic application.,” *Nanoscale*, vol. 7, no. 13, pp. 5706–11, 2015.

[132] K. S. Jeong, J. Tang, H. Liu, J. Kim, A. W. Schaefer, K. Kemp, L. Levina, X. Wang, S. Hoogland, R. Debnath, L. Brzozowski, E. H. Sargent, and J. B. Asbury, "Enhanced mobility-lifetime products in PbS colloidal quantum dot photovoltaics," *ACS Nano*, vol. 6, no. 1, pp. 89–99, 2012.

[133] J. M. Zemke, T. E. Novet, and D. R. Tyler, "Investigation of ligand effects on exciton recombination in PbS nanoparticles," *Can. J. Chem.*, vol. 89, no. 3, pp. 339–346, 2011.

[134] A. E. Colbert, W. Wu, E. M. Janke, F. Ma, and D. S. Ginger, "Effects of Ligands on Charge Generation and Recombination in Hybrid Polymer/Quantum Dot Solar Cells," *J. Phys. Chem. C*, vol. 119, no. 44, pp. 24733–24739, 2015.

[135] Z. Jin, A. Wang, Q. Zhou, Y. Wang, and J. Wang, "Detecting trap states in planar PbS colloidal quantum dot solar cells," *Nat. Publ. Gr.*, no. November, pp. 1–8, 2016.

[136] M. Yuan, K. W. Kemp, S. M. Thon, J. Y. Kim, K. W. Chou, A. Amassian, and E. H. Sargent, "High-performance quantum-dot solids via elemental sulfur synthesis," *Adv. Mater.*, vol. 26, no. 21, pp. 3513–3519, 2014.

[137] Y. Yang, B. Zhao, Y. Gao, H. Liu, Y. Tian, D. Qin, H. Wu, W. Huang, and L. Hou, "Novel Hybrid Ligands for Passivating PbS Colloid Quantum Dots to Enhance the Performance of Solar Cells," *Nano-Micro Lett.*, vol. 7, no. ?, 2015.

[138] R. N. Pereira, S. Niesar, W. B. You, A. F. Da Cunha, N. Erhard, A. R. Stegner, H. Wiggers, M. G. Willinger, M. Stutzmann, and M. S. Brandt, "Solution-processed networks of silicon nanocrystals: The role of internanocrystal medium on semiconducting behavior," *J. Phys. Chem. C*, vol. 115, no. 41, pp. 20120–20127, 2011.

[139] J. P. Clifford, K. W. Johnston, L. Levina, and E. H. Sargent, "Schottky barriers to colloidal quantum dot films," *Appl. Phys. Lett.*, vol. 91, no. 25, pp. 5–7, 2007.

[140] L. Hu, A. Mandelis, A. Melnikov, X. Lan, S. Hoogland, and E. H. Sargent, "Study of Exciton Hopping Transport in PbS Colloidal Quantum Dot Thin Films Using Frequency- and Temperature-Scanned Photocarrier Radiometry," *Int. J. Thermophys.*, vol. 38, no. 1, pp. 1–9, 2017.

[141] G. Konstantatos, “Colloidal quantum dot photodetectors,” in *Colloidal Quantum Dot Optoelectronics and Photovoltaics*, 2010, pp. 173–198.

[142] C. Hu, A. Gassenq, Y. Justo, K. Devloo-Casier, H. Chen, C. Detavernier, Z. Hens, and G. Roelkens, “Air-stable short-wave infrared PbS colloidal quantum dot photoconductors passivated with Al2O3 atomic layer deposition,” *Appl. Phys. Lett.*, vol. 105, no. 17, pp. 3–7, 2014.

[143] A. De Iacovo, C. Venettacci, L. Colace, L. Scopa, and S. Foglia, “Noise performance of PbS colloidal quantum dot photodetectors,” *Appl. Phys. Lett.*, vol. 111, no. 21, 2017.

[144] Z. Ren, J. Sun, H. Li, P. Mao, Y. Wei, X. Zhong, J. Hu, S. Yang, and J. Wang, “Bilayer PbS Quantum Dots for High-Performance Photodetectors,” *Adv. Mater.*, vol. 29, no. 33, 2017.

[145] Y. Yu, Y. Zhang, X. Song, H. Zhang, M. Cao, Y. Che, H. Dai, J. Yang, H. Zhang, and J. Yao, “PbS-Decorated WS2 Phototransistors with Fast Response,” *ACS Photonics*, vol. 4, no. 4, pp. 950–956, 2017.

[146] Z. Zheng, L. Gan, J. B. Zhang, F. Zhuge, and T. Y. Zhai, “An enhanced UV-Vis-NIR an d flexible photodetector based on electrospun Zno nanowire array/PbS quantum dots film heterostructure,” *Adv. Sci.*, vol. 4, no. 3, pp. 1–8, 2017.

[147] Y. Che, Y. Zhang, X. Cao, X. Song, H. Zhang, M. Cao, H. Dai, J. Yang, G. Zhang, and J. Yao, “High-performance PbS quantum dot vertical field-effect phototransistor using graphene as a transparent electrode,” *Appl. Phys. Lett.*, vol. 109, no. 26, 2016.

[148] Y. Wei, Z. Ren, A. Zhang, P. Mao, H. Li, X. Zhong, W. Li, S. Yang, and J. Wang, “Hybrid Organic/PbS Quantum Dot Bilayer Photodetector with Low Dark Current and High Detectivity,” *Adv. Funct. Mater.*, vol. 28, no. 11, 2018.

[149] M. Sytnyk, S. Yakunin, W. Schöfberger, R. T. Lechner, M. Burian, L. Ludescher, N. A. Killilea, A. Yousefiamin, D. Kriegner, J. Stangl, H. Groiss, and W. Heiss, “Quasi-epitaxial Metal-Halide Perovskite Ligand Shells on PbS Nanocrystals,” *ACS Nano*, vol. 11, no. 2, pp. 1246–1256, 2017.

[150] J. R. Haynes and J. A. Hornbeck, “Trapping of minority carriers in silicon. II. n-type silicon,” *Phys.*

Rev., vol. 100, no. 2, pp. 606–615, 1955.

[151] D. M. Balazs, N. Rizkia, H. H. Fang, D. N. Dirin, J. Momand, B. J. Kooi, M. V. Kovalenko, and M. A. Loi, "Colloidal Quantum Dot Inks for Single-Step-Fabricated Field-Effect Transistors: The Importance of Postdeposition Ligand Removal," *ACS Appl. Mater. Interfaces*, vol. 10, no. 6, pp. 5626–5632, 2018.

[152] S. Kahmann, M. Sytnyk, N. Schrenker, G. J. Matt, E. Spiecker, W. Heiss, C. J. Brabec, and M. A. Loi, "Revealing Trap States in Lead Sulphide Colloidal Quantum Dots by Photoinduced Absorption Spectroscopy," *Adv. Electron. Mater.*, vol. 4, no. 1, 2018.

[153] A. A. Bakulin, S. Neutzner, H. J. Bakker, L. Ottaviani, D. Barakel, and Z. Chen, "Charge trapping dynamics in pbs colloidal quantum dot photovoltaic devices," *ACS Nano*, vol. 7, no. 10, pp. 8771–8779, 2013.

[154] G. Konstantatos and E. H. Sargent, "PbS colloidal quantum dot photoconductive photodetectors: Transport, traps, and gain," *Appl. Phys. Lett.*, vol. 91, no. 17, pp. 100–102, 2007.

[155] A. De Iacovo, C. Venettacci, L. Colace, L. Scopa, and S. Foglia, "PbS Colloidal Quantum Dot Photodetectors operating in the near infrared," *Sci. Rep.*, vol. 6, 2016.

[156] H. Schumacher, H. P. Leblanc, J. Soole, and R. Bhat, "An Investigation of the Optoelectronic Response of GaAs/InGaAs MSM Photodetectors," *IEEE Electron Device Lett.*, vol. 9, no. 11, pp. 607–609, 1988.

[157] N. Debbar, A. Flu, E. Polytechnic, and F. De Lausanne, "High-speed performance of OMCVD grown InAlAs/InGaAs MSM photodetectors at 1.5 μmand 1.3 μm wavelengths," vol. 65, no. May 2005, pp. 228–230, 1994.

[158] H. T. Griem, S. Ray, J. L. Freeman, and D. L. West, "Longwavelength (1.0–1.6 μm)In0.52Al0.48As/ In0.53(Ga x Al1−x)0.47As/In0.53Ga0.47As metal/semiconductor/metal photodetector," *Appl. Phys. Lett.*, vol. 56, no. 11, pp. 1067–1068, 1990.

[159] K. Ohira, K. Kobayashi, N. Iizuka, H. Yoshida, M. Ezaki, H. Uemura, A. Kojima, K. Nakamura, H.

Furuyama, and H. Shibata, “On-chip optical interconnection by using integrated III-V laser diode and photodetector with silicon waveguide,” *Opt. Express*, vol. 18, no. 15, p. 15440, 2010.

[160] G. Konstantatos and E. H. Sargent, “Nanostructured materials for photon detection,” *Nat. Nanotechnol.*, vol. 5, no. 6, pp. 391–400, 2010.

[161] F. Xia, H. Wang, D. Xiao, M. Dubey, and A. Ramasubramaniam, “Two-dimensional material nanophotonics,” *Nat. Photonics*, vol. 8, no. 12, pp. 899–907, 2014.

[162] P. J. Pauzauskie and P. Yang, “Nanowire photonics,” *Mater. Today*, vol. 9, no. 10, pp. 36–45, 2006.

[163] C. B. Murray, D. J. Noms, and M. G. Bawendi, “Synthesis and Characterization of Nearly Monodisperse CdE (E = S, Se, Te) Semiconductir Nanocrystallites,” *J. Am. Chem. Soc.*, vol. 115, no. 4, pp. 8706–8715, 1993.

[164] C. R. Kagan, E. Lifshitz, E. H. Sargent, and D. V. Talapin, “Building devices from colloidal quantum dots,” *Science (80-.).*, vol. 353, no. 6302, pp. aac5523-aac5523, 2016.

[165] W. Yoon, J. E. Boercker, M. P. Lumb, D. Placencia, E. E. Foos, and J. G. Tischler, “Enhanced open-circuit voltage of PbS nanocrystal quantum dot solar cells.,” *Sci. Rep.*, vol. 3, p. 2225, 2013.

[166] Y. Zhu, T. Song, F. Zhang, S. T. Lee, and B. Sun, “Efficient organic-inorganic hybrid Schottky solar cell: The role of built-in potential,” *Appl. Phys. Lett.*, vol. 102, no. 11, 2013.

[167] D. Photodetectors, “Solution-Processed Quantum,” vol. 97, no. 10, 2009.

[168] E. J. D. Klem, “Infrared sensitive solution-processed quantum dot photovoltaics in a nanoporous architecture,” *Comput. Eng.*, 2008.

[169] I. Moreels, D. Kruschke, P. Glas, and J. W. Tomm, “The dielectric function of PbS quantum dots in a glass matrix,” *Opt. Mater. Express*, vol. 2, no. Copyright (C) 2013 American Chemical Society (ACS). All Rights Reserved., pp. 496–500, 2012.

[170] Y. Cheng, M. D. C. Whitaker, R. Makkia, S. Cocklin, V. R. Whiteside, L. A. Bumm, E. Adcock-Smith, K. P. Roberts, P. Hari, and I. R. Sellers, “Role of Defects and Surface States in the Carrier

Transport and Nonlinearity of the Diode Characteristics in PbS/ZnO Quantum Dot Solar Cells," *ACS Appl. Mater. Interfaces*, vol. 9, no. 15, pp. 13269–13277, 2017.

[171] D. Bozyigit, S. Volk, O. Yarema, and V. Wood, "Quantification of deep traps in nanocrystal solids, their electronic properties, and their influence on device behavior," *Nano Lett.*, vol. 13, no. 11, pp. 5284–5288, 2013.